Scuola Normale Superiore
Classe di Scienze

Search of a graviscalar particle of the Randall-Sundrum model with the CMS experiment at LHC

Tesi di perfezionamento

CANDIDATO
Dr. Simone GENNAI

RELATORE
Chiar.mo Prof. Lorenzo FOÀ

a.a. 2003

Alla mia famiglia,
a mio nonno
e ad Erica.

Contents

Introduction

In the past ten years the four LEP experiments provided the best way to prove theoretical predictions in the framework of the Standard Model. All the collected data have been well described by theory and no room has been left for signal leading to new physics. However physicists never give up and they started to think about new models involving new concepts that can reproduce the experimental data and enlarge our understanding of the ultimate nature of fundamental interactions. Among these theoretical models, one of the most amazing new concept is, in my opinion, the introduction of extra spatial dimensions. These extra dimensions could explain some theoretical black points not yet fully understood, and provide a set of clear signatures that may be investigated at the greatest particle accelerator under construction: the Large Hadron Collider (LHC).

LHC will provide the best possibilities to study any kind of signals that may lead to the discovery of new physiscs. In this thesis the candidate considers one of the most interesting consequences of the extra dimensions models: the existence of a new scalar particle. This particle (ϕ) interacts with all the other Standard Model particles and can mix with the Higgs boson, making much more interesting the study of the Higgs sector at LHC.

In order to exploit in the best way the performance of the Large Hadron Collider, a detector, with extremely good reconstruction capabilities of the final states of hadron interactions, is needed. The Compact Muon Solenoid (CMS) has been designed for this purpose. The aim of this thesis is to understand if CMS will be sensitive to the decay of the new scalar particle into a pair of Higgs boson ($\phi \rightarrow$hh).

In the first chapter of this thesis the theoretical framework of the extra dimensions is presented. After a short review of the principal ideas of the various models, the Randall-Sundrum one is presented with more details. The search

for the new scalar particle has been studied, indeed, in this specific model.
In the second chapter a schematic view of the Large Hadron collider is presented, with the main CMS subdetector: the tracker, the calorimeters, the magnet and the muon chambers.
The use of the tracker to tag b and τ jets is very important for the analysis presented in this thesis. For this reason the subdetector is described in detail in the third chapter. At the end of the chapter a measurement of the dead time of the electronics of the tracker modules is presented. The candidate has performed this measurements at the CERN laboratories in collaboration with Jacopo Bernardini, Laurent Mirabito and Roger Grabit.
The fourth chapter describes the CMS trigger strategies. The candidate has developped and implemented the isolation algorithm for the hadronic decays of the τ lepton, used as a filter in the High Level Trigger chain. This selection is of great importance in the study of the Higgs sector in CMS.
In the last chapter the analysis of the process: $gg \rightarrow \phi \rightarrow hh$ is described with three different final states:

- $hh \rightarrow \tau\tau$ bb
- $hh \rightarrow \gamma\gamma$ bb
- $hh \rightarrow$ bb bb

The candidate has studied in detail the final state with two τ leptons. The effects of possible systematical uncertainties on the knowledge of the background rate has been properly considered.

Chapter 1

Theoretical introduction

In this chapter the main reasons for the dissatisfaction with our present understanding of the foundamental interactions are presented. The basic concepts of a new, foundamental theory involving the presence of *extra dimensions* are also explained. In the following the letter h will indicate the Higgs boson in the extra dimensions scenario, while the capital H will indicate the Standard Model Higgs boson.

1.1 Merits and Failures of the Standard Model

During past years the Standard Model [1, 2, 3] of strong and electroweak interactions has worked astonishingly well. The conceptual successes (the electro-weak unification, the prediction of neutral current interactions and of the properties of the weak bosons, the necessity of the charm quark...), are only a part of its merits, most of which come from the overall agreement beetwen the theory and the vast set of experimental data collected in electron-positron annihilations, hadronic collisions and neutrino interactions, often measured at an accuracy level better than one part per mille.
The present status of this good agreement is shown in Fig. 1.1. The most important message of these ElectroWeak Precision Tests (EWPT) concernes possible physics beyond the Standard Model (SM): only very delicate deviations from the SM predictions are allowed. This is a very strong constraint on theorist's immagination.
So, why do we speak about the failures of the theory? The answer is that some

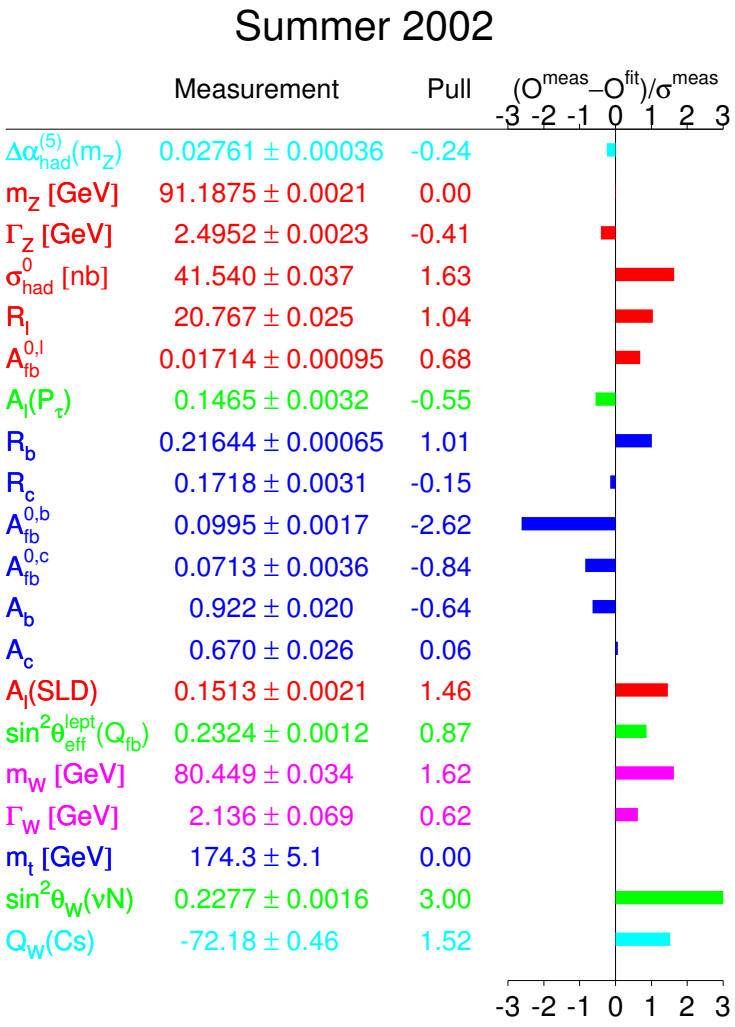

Figure 1.1: Precision Electroweak measurements and the pulls they exert on a global fit to the Standard Model.

foundamental things are not included yet in the model and even some aspects of the model itself are not well established.
A short list of the unsatisfactory features and drawbacks of the Standard Model should include at least the following:

1. too many arbitrary parameters,
2. no description for neutrino oscillations (at least if we don't want to include new energy scales related to neutrinos' masses),
3. unification of gravity to the electroweak and strong interactions,
4. finite values for the Higgs mass.

1. Even if one accepts the rather odd set of group representations and hypercharges, the Standard Model contains at least 18 free parameters (3 gauge couplings, 6 quark masses and 3 lepton masses, 4 Cabibbo-Kobayashi-Maskawa free matrix elements, 2 parameters to characterize the scalar sector of theory).[1] The common feeling of this fact is that a more fundamental theory should be invoked to naturally explain the pattern. Unification theories start from this point.
2. There is now compelling evidence that neutrinos have masses [4, 5] while in the minimal Standard Model, i.e. without including the right-handed neutrinos, these are vanishing at any order. All most popular extensions of the SM that can account for non zero neutrino masses call for a higher energy scale (should it be the mass scale suppressing higher dimensional operators that yield (Majorana) masses for left-handed neutrinos or the explicit mass for right-handed neutrino fields in the see-saw mechanism). This mass scale sits naturally close to the Unification scale and indeed small neutrino masses are addressed as the "third pillar of Unification" in [6].
3. The Standard Model is not the "Theory of Everything" since gravitational interaction is not included. The unification of gravity calls for a higher energy scale around 10^{19} GeV, at which gravitational interaction becomes comparable with gauge forces. This is called Planck mass (M_{Pl}). String theory is the only candidate to be the ultimate answer to this need.
4. The problem of the Higgs mass is very important and it is discussed in the following sections.

[1] The angle related to strong CP problem is an additional free parameter.

1.1.1 The Hierarchy Problem

From the schematic picture given above, it seems that it is all a matter of energy scales: first we meet the well known ElectroWeak Symmetry Breaking (EWSB) scale at $few \cdot 100$ GeV $\div 1$ TeV, then a large energy desert opens, up to the Unification scale and, above all, to the Planck scale. It seems that we are simply being informed that physics is not ended at the EWSB energy and we could go and look for some New Physics at those large scales. The problem is that we **must** look for New Physics at *low* energy (< 1 TeV) scales. The compelling argument to look for New Physics at low scales is known as **hierarchy problem**. It originates in the very existence of the scalar sector of the theory, coupled to the presence of higher energy scales. The standard argument goes as follows:

a. The scalar sector of the Standard Model leaves the Higgs mass as a free parameter. Such sector is the most hazardous in the theory: we postulate the existence of an elementary Higgs scalar that spontaneously realizes the EWSB since we assume a tree level potential which is characterized by the negative mass parameter μ^2 and the dimensionless quartic coupling λ. The measured value of the Fermi constant fixes a combination of these parameters (essentially μ^2/λ) but the squared mass of the physical Higgs boson, proportional to μ^2, is undetermined.

b. However, the Higgs boson has to be light. This comes from the requirement of self consistency of the model. This sets an overall upper bound on the Higgs mass of the order of 600 GeV/c^2 [7], as depicted in Fig. 1.2. More precisely, the limit depends on the high energy scale that one aims to reach: if New Physics shows up at a scale close to the Unification scale, the Higgs boson is confined to be roughly under 200 GeV/c^2. Stronger limits on the Higgs mass come from the electroweak fit to the LEP precision data [3].

c. The mass of the Higgs boson receives divergent contributions, quadratic in the cut-off Λ, already at one loop in perturbation theory, as we will check later. If the nearest available cut-off is at the Unification scale or even at the Planck scale, the quantum corrections to the Higgs mass lift the physical value by about 34 orders of magnitude (the Hierarchy). In other words, the tree level value has to be choosen with an accuracy of 10^{-34} compared to the Planck mass.

Possible solutions to the Hierarchy Problem are:

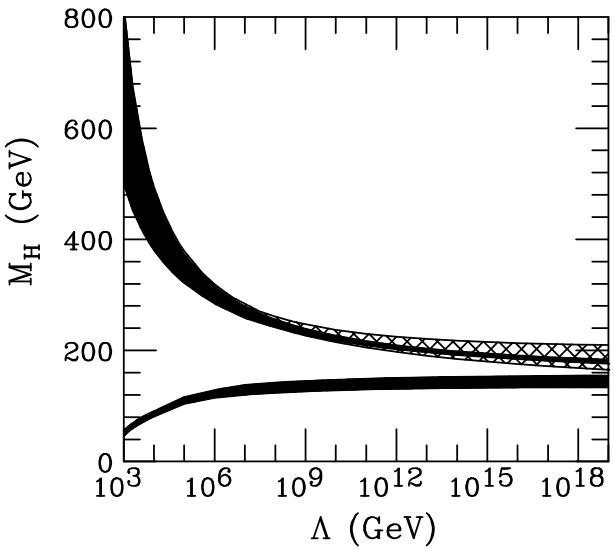

Figure 1.2: The upper (and lower) bound on Higgs mass as a function of the scale Λ at which the Standard Model ceases to be meaningful.

I. Technicolor models aim to eliminate the fundamental scalar field from the theory, replacing it with some fermion condensate: the energy scale of EWSB is then understood as the scale at which a new gauge force becomes strong. These models encounter several theoretical and phenomenological problems, I will not be interested in them here.

II. Low energy SuperSymmetry relies on the existence of an additional (although broken) symmetry that can motivate the smallness of Higgs mass. In other words, low energy SuperSymmetry aims to interpose a new energy scale low enough to limit the values of the scalar masses. This scale is related to the scale of SuSy breaking. SuperSymmetric models, and in particular the Minimal SuperSymmetric Standard Model (MSSM), feature a lot of new particles (the superpartners) that enter the model with a mass comparable to that scale. In the optics of the necessity of a light touch on EWPT, this approach is very successful since the superpartners contributions decouple very fast. Unfortunately, one should also mention that a lot more parameters are introduced: in the unconstrained MSSM, for instance, we end up with 105 new ones with respect to the SM which repropose the problem discussed in point 1 in section 1.1. Moreover (as explained in the next section) the contribution of these superpartner requires another fine tuning, this time to lift up the value of the Higgs mass.

Recently, a new idea has being considered:
III. The only fundamental scale in nature is assumed to be the ElectroWeak Breaking scale ($\sim$ 1 TeV); it also settles the scale of gravitational interactions, the enormity of the Planck scale being only a mirage produced by the presence of **large extra (space) dimensions** accessible to gravity. Due to the smallness of these extra dimensions, what we "see" is an effective gravitational coupling much smaller than the real one. The relation between these two couplings is similar to the one between G_F in the Fermi model of Weak Interaction and the "weak" coupling constant g in the Standard Model.
This theory has the advantage of having on the same energy scale all the foundamental forces, and this is a first step towards their unification. This new theory will be discussed with more details later in this chapter.

1.1.2 The LEP Paradox or Little Hierarchy Problem

The problem related to the Higgs mass is a cardinal point of any New Physics theories and it worths being discussed a little more, taking into account the consideration which can arise from the EWPT.
From EWPT it seems that the Higgs boson most probably exists and is light: this is intuitively inferred from Fig. 1.3 and Fig. 1.4, for instance. On the

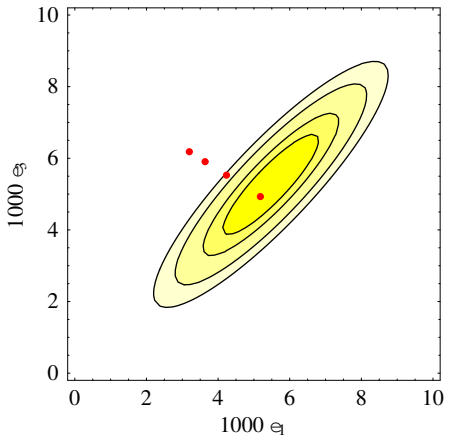

Figure 1.3: Level curves at 68, 90, 99, 99.9 per cent of confidence level of the ElectroWeak Parameters ϵ_1 and ϵ_3 compared with the SM prediction for Higgs mass equal to 100, 300, 600, 1000 GeV/c^2 (dots from right to left). The agreement is best for $m_H \simeq 100$ GeV/c^2.

other hand EWPT yield enough information to say that a characteristic scale

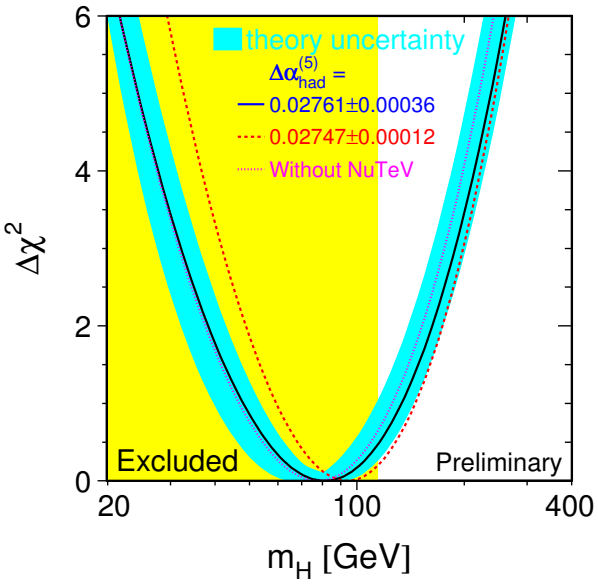

Figure 1.4: The $\Delta\chi^2$ curve derived from the Precision ElectroWeak measurements, performed at LEP and by SLD, CDF, D0, NuTeV and others, as a function of the Higgs boson mass. The preferred value, corresponding to the minimum of the curve, is around 81 GeV/c^2, with an experimental uncertainty of +52 and −33 GeV/c^2 (at 68% confidence level. The mass is lower than about 193 GeV/c^2 (one-sided 95% confidence level upper limit derived from $\Delta\chi^2 = 2.7$ for the blue band, thus including both the experimental and the theoretical uncertainty).

of any New Physics cannot be lower than about 5 TeV [8]. This limits comes mainly from the contributions of the New Physics operators to the corrections of the observables measured at LEP.

Let us now consider the most significant divergent contributions to the Higgs mass: they are the one-loop diagrams involving the top quark, the $SU(2)\times U(1)$ gauge bosons and the Higgs itself (see Fig. 1.5). The *top loop* is the most important and gives a correction:

$$\delta m_H^2(\text{top}) = -\frac{3}{\sqrt{2}\pi^2} G_F\, m_t^2\, \Lambda^2 = -\,(120\,\text{GeV})^2 \left(\frac{\Lambda}{400\,\text{GeV}}\right)^2 \qquad (1.1)$$

where G_F is the Fermi constant and m_t the top mass. Even when the New Physics scale Λ is at its lowest value, the correction is roughly 100 times larger than the most probable physical Higgs mass. To solve this problem we are

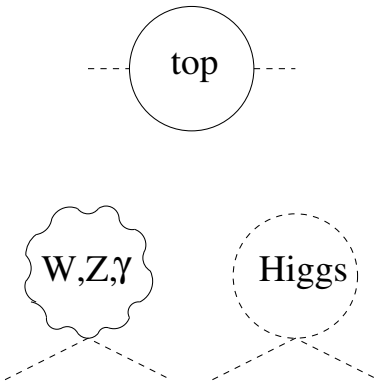

Figure 1.5: The most significant quadratically divergent contributions to the Higgs mass in the Standard Model.

obliged to assume the existence of other terms which cancel this divergency at the cost of a fine tuning of the model parameters ("**Little Hierarchy Problem**"). This can be called "**Lep Paradox**" [8], given the importance of LEP measurements to the constraints on Λ. Even invoking the traditional SuperSymmetry (i.e. in the standard 3+1 dimensions) the problem cannot be solved completely. As already mentioned in SuperSymmetric models every quadratic divergent loop diagram is accompanied by another with a superpartner running in the loop (Fig. 1.6). Let's then introduce the loops of the stop, whose

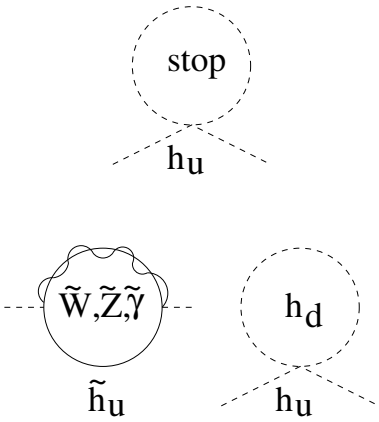

Figure 1.6: The superpartner diagrams of the loops in figure 1.5, cancelling the quadratic divergencies.

mass is $m_{\tilde{t}}$, and equation (1.1) becomes:

$$\delta m_H^2(\text{top}\,,\,\text{stop}) = -\frac{3}{\sqrt{2}\pi^2} G_F\, m_t^2\, m_{\tilde{t}}^2\, \log\frac{\Lambda^2}{m_{\tilde{t}}^2} = -0.1\, m_{\tilde{t}}^2\, \log\frac{\Lambda^2}{m_{\tilde{t}}^2} \qquad (1.2)$$

which is again divergent, although less severely.
So we can control divergences but there is again the need of a fine tuning, but this time in order to pump the Higgs mass to values greater than 115 GeV/c^2 which is the exclusion limits set by the LEP Collaborations.
Theorists are trying to join extradimensions and supersymmetric concepts in order to avoid these fine tunings and predict a range for the value of the Higgs mass.

1.2 Extra Dimensions

As already mentioned the assumption of the existence of extra dimensions can lead to the solution of the problems related to the Lep Paradox. Moreover early attempts to extend general relativity in order to unify gravity and electromagnetism within a common geometrical framework trace back to Gunnar Nordstr om (1914) [11], Theodor Kaluza (1921) and Oscar Klein (1926) [12]. They proposed that unifcation of the two forces occurred when spacetime was extended to a five dimensional manifold and imposed the condition that the fields should not depend on the extra dimension. A difficulty with the acceptance of these ideas at the time was a lack of both experimental implications and a quantum description of gravitational dynamics.
Today, one of the most striking requirements of modern string theory, which incorporates both gauge theories and gravitation, is that there must be six or seven extra spatial dimensions. Otherwise the theory is anomalous. Recently, concepts developed within string theory have led to new phenomenological ideas which relate the physics of extra dimensions to observables in a variety of physics experiments.
It is in this perspective that the idea of the existence of Extra space Dimensions is worth being pursued.
Motivated by the introduction above, we will assume that one or more extra space dimensions exist.[2] The additional space is usually named "bulk". In the bulk can be embedded a hyper-surface (often a (3+1)-dimensional space)

[2]For general reviews on Extra Dimensions see [13].

called "brane", on which some fields are possibly confined by some mechanism. The choice of which fields can access the bulk fixes also the type of problem the theory can solve. Usually a theory in which Gravity can access the bulk is used to solve the Hierarchy Problem, while a theory in which SM fields can access the bulk is addressed to the Little Hierarchy Problem.
Also the geometry of the bulk can differ from one model to another. We can group the theory in two main streams:

- **Flat Compactified Extra Dimensions**;
- **Warped Extra Dimensions**.

As mentioned above each stream can then be divided in:

- **Gravitational Extra Dimensions** (only the graviton in extra dimensions)
- **Universal Extra Dimensions** (also SM fields in extra dimensions)

Even if in some model the extra dimensions can be indeed infinite, we are interested in the compactified, i.e. made *finite*, extra dimensions. Each extra dimension is so assumed to have a finite radius R which is the crucial parameter. [3] If the size of the extra dimensions is enough microscopic, the space-time is effectively four dimensional at distances that largely exceed R. Equivalently: experiments probing energies much lower than the compactification scale $1/R$ will see no hint of their presence. In the following a brief description of these main streams is given, with more emphasis to the Warped Extra Dimensions with gravitons accessing the bulk. It is in this scenario that the presence of new scalar particles becomes of relevant interest.

1.2.1 Flat Compactified Extra Dimensions

In general, the physics of Extra Dimensions is effectively described from a 4-dimensional point of view in terms of Kaluza-Klein fields. What is explained in the following is valid also in the Warped extra dimensions, provided few changes are taken into account. As a reference, let us consider the case of one

[3] If more than one extra dimension are present the resulting compactification manifold is a torus that can also be beautifully endowed with a non trivial shape [14].

extra dimension y, so that the complete set of coordinates in (4+1)-dimensional space time is $x^M = (x^\mu, y)$, $M = (0,1,2,3,5)$, $\mu = (0,1,2,3)$. Every field allowed in the extra dimension is a function of all 5 coordinates: $\Phi(x^\mu, y)$. The compactification implies that the points $y = 0$ and $y = 2\pi R$, at fixed point x^μ, are the same, so that the wave function of the field is periodic and can be expanded in Fourier series:

$$\Phi(x^\mu, y) = \sum_{n\in\mathbb{Z}} e^{in\frac{y}{R}} \phi_n(x^\mu) \tag{1.3}$$

where $\Phi_n(x^\mu)$ are an infinite tower of 4-dimensional (Kaluza-Klein, KK) fields. The kinetic lagrangian term for a 5D massless scalar, for instance, is:

$$\int d^4x\, dy \left(\partial_M \Phi^*\, \partial^M \Phi\right) = \int d^4x\, dy \left(\partial_\mu \Phi^*\, \partial^\mu \Phi + \partial_5 \Phi^*\, \partial^5 \Phi\right) = \tag{1.4}$$

$$= \int d^4x \sum_{n\in\mathbb{Z}} \left(\partial_\mu \phi_n^*\, \partial^\mu \phi_n - \frac{n^2}{R^2} \phi_n^* \phi_n\right) \tag{1.5}$$

Each KK mode ϕ_n, therefore, can be interpreted as a separate particle with mass $m_n = |n|/R$. At low energies, only massless modes are relevant, while at energies $\sim 1/R$ heavy modes will be produced in collision and take part in physical processes.

Probably the most important criticism to the Compact Extra Dimensions picture is related to the determination and stabilization of the compactification radii. In a sense, one introduces a new unmotivated hierarchy between the fundamental scale $M_* \sim$ TeV and the compactification scale of the extra dimensions ($\sim 10^{-3}$ eV when $R \sim 100$ μm). Although the embedding in some string theory can support certain choices [31], the need for a more fundamental theory that can predict such structures is still alive.

Gravitational Extra Dimensions

This framework of Extra Dimensions (the first that was investigated [15]) blossomed from the simple observation that the behaviour of gravitational interaction is not known at distances in the sub-mm range [16]. This opens the possibility that the graviton can experience a certain number δ of extra space dimensions of size up to ~ 100 μm.

The general set-up is very simple: all Standard Model fields are (somehow) confined on a 4D brane while the graviton is free to propagate in all the $4 + \delta$

dimensions. The extra ones are compactified on circles of radii R_i. The Hierarchy Problem is solved thanks to the volume of the extra space: the only fundamental scale is $M_* \sim$ TeV while the hugeness of the Planck mass is produced by

$$M_{Pl}^2 = \prod_{i=1}^{\delta} (2\pi R_i M_*)\ M_*^2\,. \tag{1.6}$$

Let's explain the formula above in the simpler case in which all the extradimensions have the same size R. Using the consistency of the Gauss Law in $4+\delta$ dimension it is easy to demonstrate that the Newton potential at distances smaller than the compactification radius is modified and goes with r like $1/r^{1+\delta}$ instead of $1/r$:

$$U \sim G^* \frac{1}{r^{1+\delta}} \tag{1.7}$$

where G^* is different from the Gravitational costant G we are used to. Due to dimensional consideration we can write this G^* in terms of the foundamental Mass Scale M_*:

$$G^* \sim \frac{1}{M_*^{2+\delta}} \tag{1.8}$$

For distances $r >> R$ the potential is "saturated", for what regards the δ dimensions, so that we can write:

$$U \sim G^* \frac{1}{R^\delta r^1} \tag{1.9}$$

Now using the similitude with the formula for the Newtonian potential in 3 space dimensions we get:

$$G \sim G^* \frac{1}{R^\delta} \tag{1.10}$$

and using the relation $G \sim 1/M_{Pl}^2$ we get:

$$M_{Pl}^2 \sim M_*^2 (M_* R)^\delta \tag{1.11}$$

The generalization to the case of extra dimension with different radii, is now obvious.

A lot of different physical processes have to be considered in order to guarantee the experimental viability of such a scenario. Schematically, relevant constraints or confirmations can come from (besides of course the detection of a modification of Newton law at small distances):

- **collider physics** [17, 18, 19], via the phenomenon of graviton production and virtual exchange or even, since the gravity scale is lowered to TeV, black hole production;
- **astrophysics** [17, 20], since the cooling of Supernovae must not be unacceptably accelerated by KK graviton emissions; this turns out to be one of the most stringent constraints in the case that all extra dimensions have the same size (at least 3 extra dimensions are needed), but can be relaxed if the radii are allowed to be different;
- **cosmology** [17, 21], from the fact that relic KK gravitons must not be so numerous to over-close the universe and from the fact that KK gravitons can "come back" from the bulk and decay giving an unobserved distorsion of the photon spectrum; again these severe limits can be eased in models with enough extra dimensions or with a non degenerate structure of radii.

Moreover, one can investigate the modifications induced by KK gravitons in rare decays [17], ultra high energy cosmic ray physics [22], other astrophysical issues such as the additional heating of neutron stars [17], other cosmological points including Big Bang Nucleosynthesis [21] and so on.
In short, one can state that all phenomenological tests are passed, with the fundamental scale still fixed at $M_* \sim$ TeV (to solve the Hierarchy), at least paying the price of some uncomfortable flexibility in the constructions.

Universal Extra Dimensions

Another interesting realizations of theories with extra dimensions are the models in which also the fields of the Standard Model or MSSM propagate in the bulk [24, 25, 26, 27, 28].
Many possible variations on this theme have been implemented, particularly regarding the choice of the fields allowed in the bulk (all SM/MSSM fields, only gauge bosons with all or some matter fermions confined on a brane, only Higgs bosons...) some general aspects can be outlined:

- in this case the focus is not on the unification of EW and Gravitational forces, as in the previous model, infact Gravity is not considered at all. The interest in these models cames from the possibility to solve some

problems of the Standard Model or MSSM as for example the Lep Paradox, or the neutrino masses.

- the size of the extra dimensions have to be much smaller than the case where only gravity is higher dimensional, since of course ElectroWeak interactions are probed at much smaller distances; the typical compactification energy must indeed be larger than $\sim few \cdot 100$ GeV $\div 1$ TeV, corresponding to radii smaller than $\sim 10^{-17}$ cm; [4]

- the models usually need only one extra dimension, that is often compactified on a circle with at least one additional $\mathbb{Z}_2$ symmetry: $y \to -y$. Such a structure is called an *orbifold*.

- In the limit of "low energy" the reference model (SM, MSSM, etc.) is reproduced by the zero modes of the KK expansion.

Interesting works on the theory have been proposed by Barbieri, J. Hall and Nomura [30]. In this model Gravity is not taken into account, but SuperSymmetry is introduced both in the brane and in the bulk. In this way the entire KK towers will contribute to the Higgs mass corrections. The result is that the Higgs mass assumes a finite value, indipendent from the cutoff Λ. The presence of two $\mathbb{Z}_2$ symmetries limits the number of zero modes KK fields, removing zero modes superpartners fields so that only the SM zero modes are present.
The symmetries of the model put limits also in the Higgs potential terms, so that the model can predict a Higgs boson mass arount 127 GeV/c^2.

1.2.2 Warped Extra Dimensions

An alternative scenario [32, 33] that does not suffer of the residual hierarchy highlighted in section 1.2.1 can be built with at least one extra dimension accessible to gravity, provided that the metric of the space time distinguishes between the four traditional coordinates and the additional ones.
Let's discuss the simplest realization of this theory: only one extra dimension is present. Differently from the previous case the geometry of the 5^{th} dimension is the one of a space of constant negative curvature. The additional dimension

[4] Of course hybrid models are possible, where some large extra dimensions are accessible to gravity and some smaller ones to the SM fields [29].

is contained between two branes located at $y = 0$ and $y = \pi R_c$. Every slice of this dimension corrisponds to a 4-d Minkowski metric. The Standard Model fields are localized on one of the 3-brane. The metric in 5 dimensions is the one of a "flat" space with a "warp" factor, a rapidly changing (exponential) function of the extra coordinate, multiplying the 4-d Minkowski term:

$$ds^2 = e^{-2k|y|}\eta_{\mu\nu}dx^\mu dx^\nu - dy^2 \tag{1.12}$$

where $\eta_{\mu\nu}$ is the usual 4-d Minkowski metric, k is a parameter of the theory which is assumed to be of order of the Planck Scale. Consistency of the low-energy theory sets $k/\overline{M}_{Pl} < 0.1$, with $\overline{M}_{Pl} = M_{Pl}/\sqrt{8\pi} = 2.4 \times 10^{18}$ being the reduced 4-d Planck scale.
The Hierarchy problem is solved assuming that there exists only one Mass Scale which is of order of $\overline{M_{Pl}}$ and the scale of physical phenomena in our 4-d flat space is achieved by the exponential warp factor. The scale Λ of the EWSB is then:

$$\Lambda \equiv \overline{M}_{Pl}e^{-kR_c\pi} \tag{1.13}$$

where we can obtain $\Lambda \sim 1$ TeV with $kR_c \sim 11$ - 12. It has been demonstated [34] that this value of kR_c can be stabilized within this configuration without the fine tuning of the model parameters. The picture is perfectly consistent with $R_c \to \infty$ [35], therefore opening the way to infinite, non-compact extra dimensions.[5]

1.2.3 The scalar sector of Extra Dimensions

One particularly attractive warped extra dimensional model is the one proposed by Randall and Sundrum (RS) [32, 35, 36], in which there are two 3+1 dimensional branes separated in a 5th dimension. In the simplest version of the 5-dimensional RS model, all the SM particles and forces, with the exception of gravity, are confined to one of the 4-dimensional boundaries. Gravity lives on this visible brane, on the second hidden brane and in the 5-dimensional compactified bulk. The warp factor e^{-kR_c} is called Ω_0. As the metric is present in the Action of all the Standard Model particles, we can derive the interaction between gravitons and SM particles from the linear expansion of the metric itself in 5 dimensions:

$$G_{\alpha\beta} \equiv e^{-2k|y|}\left(\eta_{\alpha\beta} + 2/M_*^{3/2}h_{\alpha\beta}\right) \tag{1.14}$$

[5]Notice that in this case the focus is no more on the Hierarchy Problem.

Where α and β are the indexes of the 5-d space and can be: 0,1,2,3,5; while $h_{\alpha\beta}$ is the graviton field. After the compactification, i.e. after imposing the boundary condition for the graviton field, we can expand the graviton field in KK modes and we can decompose it in different four dimensional fields. For δ extra dimension, with $\delta > 2$ we have: 1 spin-two fields, (δ-1) spin-one fields and $\delta(\delta-1)/2$ spin-zero fields. The KK expansions of these fields are the following:

$$h_{\mu\nu}(x,y) = \sum_{n=0}^{\infty} h^n_{\mu\nu}(x) C^n(y) \;\; (spin-2) \tag{1.15}$$

$$A_{\mu i}(x,y) = \sum_{n=0}^{\infty} A^n_{\mu i}(x) C^n(y) \;\; (spin-1) \tag{1.16}$$

$$\phi_{ij}(x,y) = \sum_{n=0}^{\infty} \phi^n_{ij}(x) C^n(y) \;\; (spin-0) \tag{1.17}$$

Where x and y are respectively the 4-d and extra dimensional coordinates, μ, ν=0,1,2,3 and i, j=5,...,4+δ, $C^n(y)$ are the expansion coefficients. In a flat geometry space they would be equal to $exp(iny/R_c)$ but in this model, due to the strong curvature of the extra dimension and the warp factor, $C^n(y)$ are the Bessel functions. After integrating over the extra dimensions we can recognize, from the kinetic term of the Lagrangian, that the KK states acquire a mass $m_n = x_n k e^{-kR_c\pi}$, with x_n the zero points of the Bessel function $J_1(x)$.
The spin-1 particles don't couple to fermions and Gauge bosons.
For δ =1 there is only one scalar particle, called Radion. This particle represents the radial fluctuations of the 5^{th} dimensions. The problem of stabilizing this radius is related to give a mass to the zero mode of the Radion. Therefore the value of its mass depends on additional model-building assumptions [37], not just on the geometry.
In the RS model, a mixing between the radion field and the Higgs field comes naturally from the Action of Higgs field [38]. Let's now consider the kinetic term of the Higgs Lagrangian [39]), after the usual shift: $H_0 = \frac{1}{\sqrt{2}}(v + h_0)$ with v= 246 GeV:

$$\mathcal{L} = -\frac{1}{2}\left[1 + 6\gamma^2\xi\right]\phi_0 \Box \phi_0 - \frac{1}{2}\phi_0 m^2_{\phi_0}\phi_0 - \frac{1}{2}h_0\left(\Box + m^2_{h_0}\right)h_0 - 6\gamma\xi\phi_0\Box h_0, \tag{1.18}$$

where m_{h_0} ($\equiv 2\lambda v^2$) and m_{ϕ_0} are the Higgs and radion masses before mixing, $\gamma \equiv v/\Lambda$, and ξ is an adimensional mixing parameter, if $\xi = 0$ no mixing is present. Λ represent the EWSM energy scale $\sim \Omega_0 \overline{M}_{Pl}$ and it specifies the

strength of the radion interactions with matter. We can consider a range of values for Λ, from 1 to 10 TeV, without loosing any consistency for the solution of the Hierarchy Problem.
The states that diagonalize the kinetic energy and have canonical normalization are h and ϕ with:

$$h_0 = \left[\cos\theta - \frac{6\xi\gamma}{Z}\sin\theta\right] h + \left[\cos\theta + \frac{6\xi\gamma}{Z}\sin\theta\right] \phi \equiv dh + c\phi \quad (1.19)$$

$$\phi_0 = -\cos\theta\frac{\phi}{Z} + \sin\theta\frac{h}{Z} \equiv a\phi + bh. \quad (1.20)$$

Here, the mixing angle θ is given by

$$\tan 2\theta \equiv 12\gamma\xi Z \frac{m_{h_0}^2}{m_{\phi_0}^2 - m_{h_0}^2\,(Z^2 - 36\xi^2\gamma^2)}, \quad (1.21)$$

and

$$Z^2 = 1 + 6\xi\gamma^2\,(1 - 6\xi) \equiv \beta - 36\xi^2\gamma^2. \quad (1.22)$$

The corrisponding mass-squared eigenvalues are:

$$m_\pm^2 = \frac{Z^2}{2}\left[m_{h_0}^2 + m_{\phi_0}^2 \pm \left((m_{h_0}^2 + m_{\phi_0}^2)^2 - \frac{4\beta m_{h_0}^2 m_{\phi_0}^2}{Z^2}\right)^2\right]. \quad (1.23)$$

since m_+ will identify either m_h or m_ϕ, the physical states h and ϕ cannot be too close to being degenerate in mass, depending on the precise values of ξ and γ; extreme degeneracy is allowed only for small ξ and/or γ.
The couplings of the h and ϕ to ZZ, WW and ff are given relative to those of the SM Higgs boson, denoted by H, by:

$$\frac{g_h W^+W^-}{g_H W^+W^-} = \frac{g_h ZZ}{g_H ZZ} = \frac{g_h f\overline{f}}{g_H f\overline{f}} = d + \gamma b, \quad (1.24)$$

$$\frac{g_\phi W^+W^-}{g_H W^+W^-} = \frac{g_\phi ZZ}{g_H ZZ} = \frac{g_\phi f\overline{f}}{g_H f\overline{f}} = c + \gamma a. \quad (1.25)$$

Couplings of the h and ϕ to $\gamma\gamma$ and gg receive contributions not only from the usual loop diagrams but also from trace-anomaly couplings of the ϕ_0 to $\gamma\gamma$ and gg. Thus, these couplings are not simply directly proportional to those of the SM H. Of course, in the limit of $\xi = 0$, the h has the same properties as the SM Higgs boson.
In the end, when $\xi \neq 0$ the four primary independent parameters are: ξ, Λ and the mass eigenvalues m_h and m_ϕ. These completely determine a, b, c, d

and, hence, all the couplings of the h and ϕ to W^+W^- , ZZ and $f\overline{f}$.
Two further parameters are required to completely fix the h and ϕ decay phenomenology in the RS model: $\hat{\Lambda}_W$ (which determines KK-graviton couplings to the h and ϕ) and m_1, the mass of the first KK graviton excitation:

$$\hat{\Lambda}_W \sim \sqrt{2}M_{Pl}\Omega_0 \tag{1.26}$$

$$m_1 = x_1 k\Omega_0 = x_1 k\frac{\Lambda}{\overline{M}_{Pl}} \tag{1.27}$$

where x_1 is the first zero of the Bessel function J_1 ($x_1 \sim 3.8$).
Searches for the Radion have been made at both hadronic and leptonic colliders. Current bounds, derived from Tevatron Run I data and precision electroweak constraints have been examined in [40].
As the ϕZZ coupling remains small relative to the SM HZZ coupling for low radion masses [39], lower bounds on the radion mass, from Higgs searches at LEP, are weak.
Lower bounds for m_1 come from: KK excitation corrections to precision electroweak observables and RunI Tevatron searches for KK excitations; from these measurements the lower bound is set to 450 GeV. We can use this bound together with the requirment of low-energy consistency of the theory ($k/\overline{M}_{Pl} < 0.1$) to get the reference value for $\Lambda \sim 5.8$ TeV from equation 1.27.
At higher k/M_{Pl} , the naive RunI Tevatron restriction becomes much stronger than the precision electroweak constraint. Thus, for example, at $k/M_{Pl} \sim 0.1$ we employ the RunI Tevatron constraint of $m_1 > 600$ GeV/c^2 to obtain $\Lambda >$ 4 TeV.
Although large $\Lambda >$ 4-5 TeV is guaranteed to avoid conflict with all existing constraints from LEP/LEP2 and RunI Tevatron data, it is by no means certain that such a large value is required. For example, if $\Lambda = 1$ TeV, m_1 ranges from $\sim$ 75 GeV/c^2 to $\sim$ 1.55 TeV as k/M_{Pl} ranges from .05 to 1. For this case, if we take k/M_{Pl} to be of order 1, then $m_1 \sim 1.55$ TeV and there are no precision electroweak or RunI constraints.
In the following section a brief phenomenology of the scalar sector of the model and the exclusion regions of the parameter space are presented for $\Lambda = 5$ TeV.

1.2.4 Phenomenology for Λ= 5 TeV

In this section the restrictions on the h, ϕ sector imposed by LEP Higgs boson searches are discussed. This section is related to the work of Dominici *et al.*, for more details see [39].
LEP/LEP2 provides an upper limit to the coupling of a ZZ pair to a scalar (s) as a function of the scalar mass. Because the decays of the h and ϕ can be strongly influenced by the ξ mixing, it is necessary to consider limits that are obtained both with and without making use of b tagging. The most recent paper on the 'flavor-blind' limits obtained without b tagging is [41]. Next, there is a preliminary OPAL note [42] in which decay-mode-independent limits on the ZZs coupling are obtained that are considerably stronger than those of [41], but not as strong as those of [43]. For scalar masses above 60 GeV/c^2, the flavor-blind limits of the above references are superseded by the results shown on the LEPHIGGS working group homepage [44], which extend up to $m_s < 113$ GeV/c^2. Reference [41] is used for $m_s < 60$ GeV/c^2 and [44] for 60 GeV/c^2< $m_s < 113$ GeV/c^2. Including the stronger limits of [43] and/or [42] would have no impact on the plots presented. Limits on g^2_{ZZs} can be also set using b tagging and assuming that $BR(s \to \mathrm{b\overline{b}}) = \mathrm{BR}(\mathrm{h_{SM}} \to \mathrm{b\overline{b}})$. Excluded and allowed regions are plotted in Fig. 1.7 for Λ=5 TeV and m_h =120 GeV/c^2. For any given value of m_h and m_ϕ, the range of ξ is limited by:

1. the constraint of eq. 1.23 limiting ξ according to the degree of $m_h - m_\phi$ degeneracy;
2. the constraint that $Z^2 > 0$ in eq. 1.22;
3. the requirements that g^2_{ZZh} and $g^2_{ZZ\phi}$ both lie below any relevant LEP/LEP2 limit, (countur plots of the coupling g^2_{ZZh} are shown in Fig. 1.8 for m_h=120 GeV/c^2).

For the most part, it is the degeneracy constraint (1) that defines the shown theoretically acceptable regions. The regions within the theoretically acceptable regions that are excluded by the LEP/LEP2 limits are shown by the yellow shaded regions, while the allowed regions are in blue. The precise regions shown are somewhat sensitive to the Λ choice, but the overall picture is always similar to that presented here for $\Lambda = 5$ TeV.
In Fig. 1.9, the branching ratios for $h \to b\overline{b}$, gg, WW, ZZ and $\gamma\gamma$ are plotted

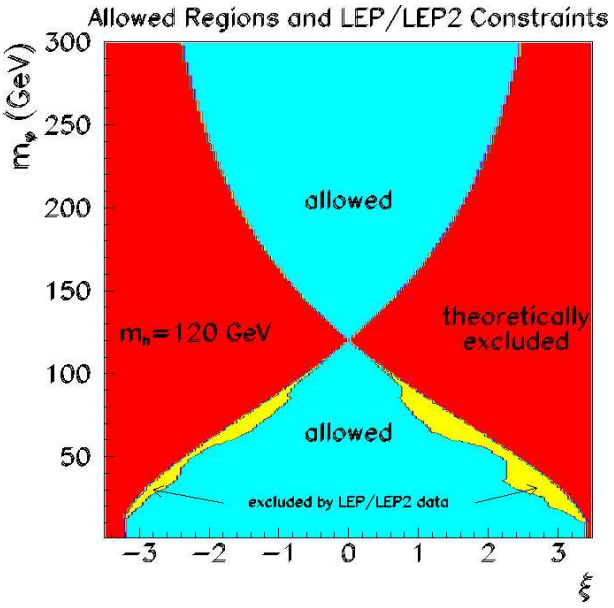

Figure 1.7: Allowed regions (see text) in (ξ, m_ϕ) parameter space for $\Lambda = 5$ TeV and for m_h=120 GeV/c^2 (lower). The dark red portion of parameter space is theoretically disallowed. The light yellow portion is eliminated by LEP/LEP2 constraints on the ZZs coupling-squared g^2_{ZZs} or on $BR(s \to b\bar{b})$, with $s = h$ or $s = \phi$.

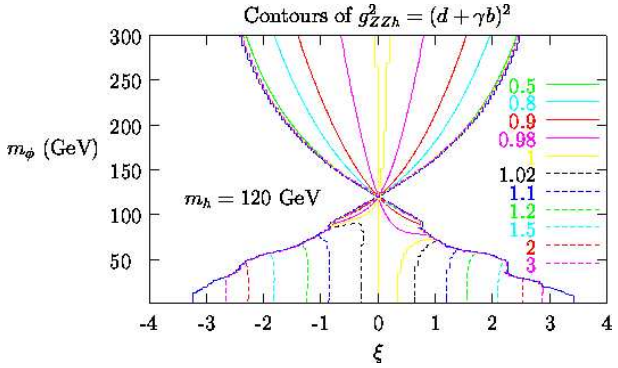

Figure 1.8: The quantity $g^2_{ZZh} = (d+\gamma b)^2$ which specifies the ratio of the h $f\overline{f}$ and VV couplings squared to the corresponding values for the SM Higgs boson, taking $m_{h_{SM}} = m_h$, for Λ=5 TeV and m_h=120 GeV/c^2. Line colors/textures drawn actually on the boundary should be ignored.

as a function of the mixing parameter ξ, taking $m_h = 120$ GeV/c^2 and $\Lambda = 5$ TeV. Results are shown for two different m_ϕ values: 55 and 200 GeV/c^2. (The case of $m_\phi = 55$ GeV/c^2 is one for which the BR(h$\to \phi\phi$) can be quite large when $m_h = 120$ GeV/c^2.) These plots are limited to ξ values allowed by the theoretical constraints discussed earlier. It is relevant to note that large

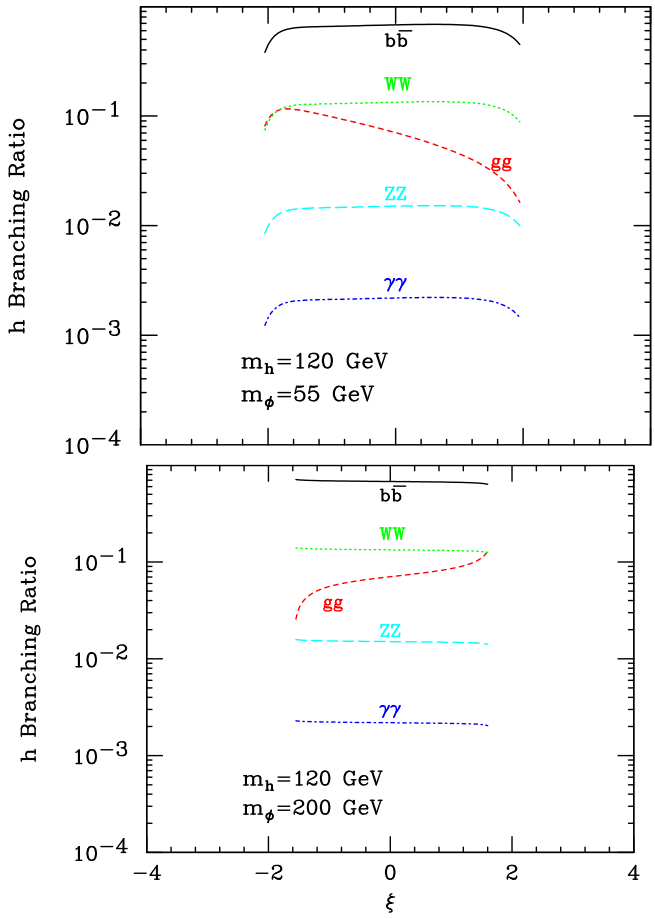

Figure 1.9: The branching ratios for h decays to $b\bar{b}$, gg, WW, ZZ and for $m_h = 120$ GeV/c^2 and $\Lambda = 5$ TeV as functions of ξ for $m_\phi = 55$ and 200 GeV/c^2.

values for the gg branching ratio (due to the anomalous contribution to the hgg coupling) are the norm. This suppresses the other branching ratios to some extent.

Results for the ϕ branching ratios are plotted in Fig. 1.10. The gg decay is generally dominant over the $b\bar{b}$ mode and it has the largest branching ratio until the WW*, ZZ* modes increase in importance at larger m_ϕ.

In the next section the radion production at the Large Hadron Collider (see next Chapter for more details) and its decay in a Higgs pair is described. This process has been studied in detail, by the candidate, in the fifth chapter. A Higgs mass value of 125 GeV/c^2 and a radion mass of 300 GeV/c^2 have been considered.

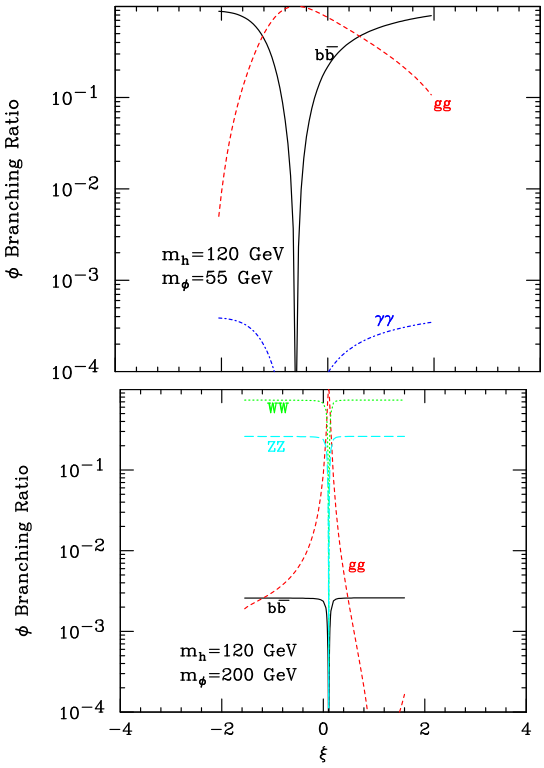

Figure 1.10: The branching ratios for ϕ decays to $b\bar{b}$, gg, WW, ZZ for m_h = 120 GeV/c^2 and Λ = 5 TeV as functions of ξ for m_ϕ = 55 and 200 GeV/c^2.

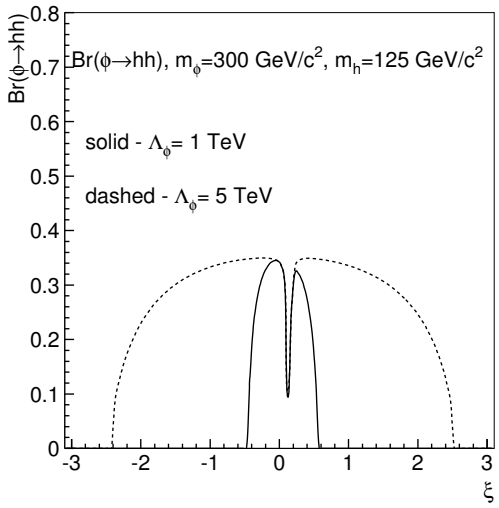

Figure 1.11: The $\phi \to hh$ branching ratio is plotted as a function of ξ for m_h = 125 GeV/c^2 and m_ϕ = 300 GeV/c^2, for Λ_ϕ = 1 and 5 TeV and assuming $m_1 > m_\phi$.

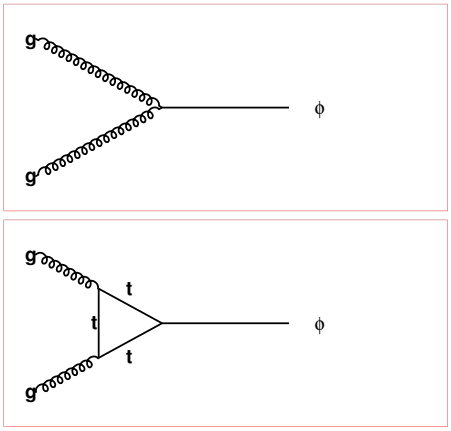

Figure 1.12: Feynman diagrams for the production process. The bottom plot exists only in the case of mixing with the Higgs boson.

The gg→ ϕ →hh process

Experimentally an interesting way to discover the radion is through its decay in a pair of Higgs bosons: $\phi \rightarrow$ hh. When allowed, these decays can offer a good opportunity to study both scalar particles at the same time. The branching ratios of the $\phi \rightarrow$ hh decays is illustrated for $m_h = 125$ GeV/c^2 and $m_\phi = 300$ GeV/c^2 in Fig. 1.11. Even though $m_\phi > 2m_W$, the BR($\phi \rightarrow$ hh) is still of order 0.3 for most of the allowed ξ range excluding the regionin which the ϕhh coupling vanishes near ξ=0.
Figure 1.12 shows the Feynman diagrams for the production process. The bottom plot exists only in the case of mixing with the Higgs boson. The cross section for the process gg→ ϕ can be calculated as:

$$\sigma(\mathrm{gg} \rightarrow \phi) = \sigma(\mathrm{gg} \rightarrow \mathrm{H_{SM}}) \cdot \frac{\Gamma(\phi)}{\Gamma(\mathrm{H_{SM}})} \cdot \frac{\mathrm{Br}(\phi \rightarrow \mathrm{gg})}{\mathrm{Br}(\mathrm{H_{SM}} \rightarrow \mathrm{gg})} \tag{1.28}$$

where Γ is the total width of the radion or Standard Model (SM) Higgs boson and Br is the branching ratio to a pair of gluons. The total width and branching ratio for a radion mass of 300 GeV/c^2 are shown in Fig. 1.13 as a function of the parameter ξ for two values of Λ_ϕ, 1 and 5 TeV. The values of $\sigma(\mathrm{gg} \rightarrow \mathrm{H_{SM}})$ (7.52 pb), $\Gamma(\mathrm{H_{SM}})$ (8.5 GeV/c) and $\mathrm{Br}(\mathrm{H_{SM}} \rightarrow \mathrm{gg})$ ($5.68{\cdot}10^{-3}$) were calculated at the next-to-leading order with HIGLU and HDECAY programs [46] for the center of mass energy of the Large Hadron Collider (14 TeV). Figure 1.14 shows the $\sigma(\mathrm{gg} \rightarrow \phi)$ as a function of the parameter ξ for two values of Λ_ϕ, 1

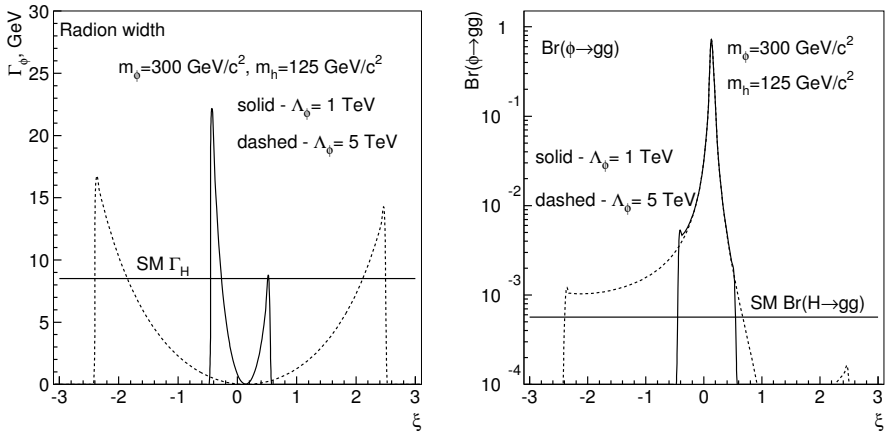

Figure 1.13: The total width(left plot) and branching ratio of radion to a pair of gluons (right plot) for the radion of the mass 300 GeV/c^2 as a function of the parameter ξ for two values of Λ_ϕ, 1 and 5 TeV. The values for a SM Higgs boson of 300 GeV/c^2 mass are also shown as the horizontal lines.

and 5 TeV. The maximal cross section is about 100 pb ($\Lambda_\phi = 1$ TeV).
In this thesis the following final states have been investigated:

- $\phi \rightarrow \mathrm{hh} \rightarrow \tau\tau\mathrm{b\overline{b}}$,
- $\phi \rightarrow \mathrm{hh} \rightarrow \gamma\gamma\mathrm{b\overline{b}}$,
- $\phi \rightarrow \mathrm{hh} \rightarrow \mathrm{b\overline{b}b\overline{b}}$.

Branching ratios of the Higgs boson in the Standard Model and in the Randall-Sundrum model are similar, as shown in Fig. 1.15, for m$_\mathrm{h}$ = 125 GeV/c^2. The BR(h→bb) is about 70%, the BR(h→ $\tau\tau$) is about 7% and BR(h→ $\gamma\gamma$) is 2×10^{-3}.

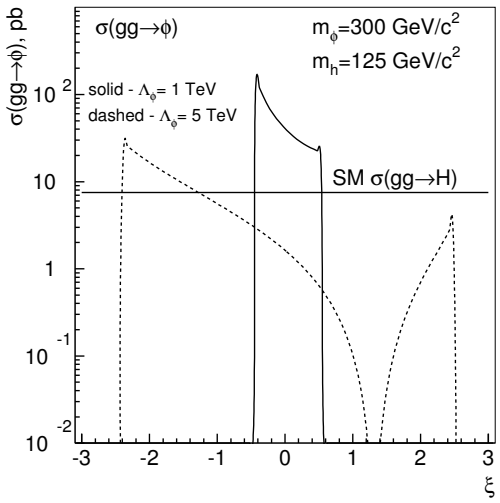

Figure 1.14: $\sigma(\mathrm{gg} \to \phi)$ as a function of the parameter ξ for two values of Λ_ϕ, 1 and 5 TeV. The cross section of $\mathrm{gg} \to \mathrm{H_{SM}}$ process for the SM Higgs boson of 300 GeV/c^2 mass is also shown as the horizontal line.

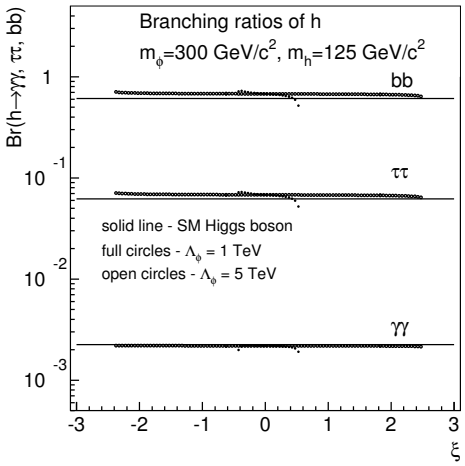

Figure 1.15: Branching ratios of the Higgs boson in the Standard Model and in the Randall-Sundrum model for $\mathrm{m_h} = 125$ GeV/c^2 as a function of the parameter ξ for two values of Λ_ϕ, 1 and 5 TeV.

da segneri

Chapter 2

The Large Hadron Collider and the CMS Experiment

This chapter provides an overview of the experimental facility. In the first part the basic features of the accelerator are described, with a special emphasis on the aspects related to physics. Then the CMS experiment, the main subdetectors and the trigger system are reviewed.

2.1 The Large Hadron Collider

The Large Hadron Collider (LHC) [47] will be the largest hadron collider in the world at its planned starting date in 2007. It will provide proton-proton collisions at a centre-of-mass energy $\sqrt{s} = 14$ TeV and it will be placed in the already existing LEP tunnel at CERN.
To supply the LHC with pre-accelerated protons, the existing CERN facilities have been upgraded. Protons will be accelerated through many steps by the already existing machines: a Linac will bring them up to 50 MeV, a Booster up to 1.4 GeV, the PS up to 25 GeV and the SPS up to 450 GeV. Finally, protons will be injected in the Large Hadron Collider where they will be accelerated up to 7 TeV. A scheme of the CERN acceleration complex is shown in Fig. 2.1.
Since collisions will occur between particles of the same type, two separate beam channels with opposite beam directions are required. The two channels, together with their superconducting dipole magnets will be inserted in a single cryostatic structure. Dipoles will operate at 1.9 K, where Helium becomes

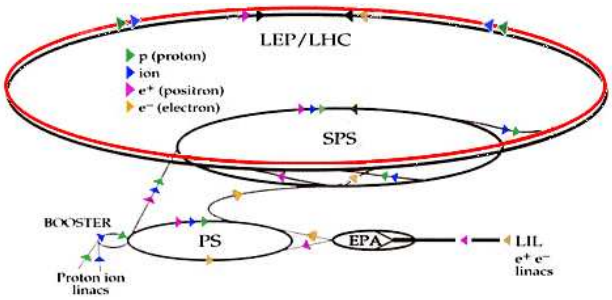

Figure 2.1: Overview of the accelerator complex at CERN. The sketch also shown the LEP electron and positrons trajectories as well as those of the LHC protons and heavy ions.

Parameter	Value
Circumference (km)	27
Number of magnet dipoles	1232
Dipolar magnetic field (Tesla)	8.386
Magnet Temperature (Kelvin)	1.9
Beam Energy (TeV)	7
Maximum Luminosity ($cm^{-2}s^{-1}$)	10^{34}
Protons per bunch	$1.05 \cdot 10^{11}$
Bunch spacing (ns)	24.95
R.M.S. bunch length	7.5 cm
Transverse beam size @ I.P.	16μm
Crossing angle	200μrad
Beam Lifetime	22 h
Luminosity Lifetime	10 h

Table 2.1: Main technical parameters of LHC.

superfluid, and will provide a $\sim$ 9 Tesla magnetic field. The boost will be provided by 400 MHz superconducting radiofrequency cavities with a voltage ranging from 8 to 16 MV/m. The nominal number of protons per bunch will be 10^{11}: bunches will have a very small transverse spread, $\sigma_x \sim \sigma_y \sim 15\mu$m, while they will be 7.5 cm long in the z direction at the collision points. The main features of the accelerator are summarized in Table 2.1. The accelerator parameter related to the rate of interactions is the *Luminosity* ($\mathcal{L}$): it depends on the number of protons per bunch (n_1 and n_2 for the two colliding beams respectively), the revolution frequency (f) and the widths which characterise the Gaussian transverse beam profiles in the horizontal (bending) and vertical

directions (σ_x and σ_y respectively) through the formula:

$$\mathcal{L} = f\frac{n_1 n_2}{4\pi\sigma_x\sigma_y}. \tag{2.1}$$

The number of interactions N_i, corresponding to the process i with a cross section σ_i, is related to $\mathcal{L}$ through the relationship

$$N_i = \sigma_i \int \mathcal{L}dt. \tag{2.2}$$

$\int \mathcal{L}dt$ is also called *Integrated Luminosity*. For the first few years the luminosity value will be $\mathcal{L} = 2 \times 10^{33} cm^{-2}s^{-1}$ (low luminosity run). An integrated luminosity of 20 fb^{-1} per year will be collected. After this period, which will be mainly dedicated to tune the detector performance to search for new particles and to study B physics, the luminosity will be increased to the design value $\mathcal{L} = 10^{34} cm^{-2}s^{-1}$. The second phase of data taking, the high luminosity period, will be dedicated to extend the searches. It will last 5 years and 100 fb^{-1} of integrated luminosity will be collected each year for a total of 500 fb^{-1}. Four detectors will be installed in the caverns around the collision points. Two of them will be multipurpose experiments: ATLAS[48] and CMS[49]. In the two remaining points, the ALICE[50] and LHCb[51] experiments will be dedicated respectively to heavy ions and $b-$physics.

2.1.1 Physics and Experimental Requirements

The main physics goal for the LHC experiments is the search for the Higgs boson. The new accelerator will allow the exploration of a mass range from $\sim$ 100 GeV, which is the current lower bound, up to $\sim$ 1 TeV. Searches for Supersymmetry signals or tests of alternative models are the second physics goal of LHC, while the very large statistics of events will make possible also precision measurements on electroweak, heavy flavours and QCD physics. To cope with this ambitious program, the LHC experiments were designed to be fully hermetic and to achieve optimal sensitivity in the harsh experimental environment of the new machine.
The first challenge for LHC experiments comes from the very high event rate. The cross-sections for different processes at LHC span several orders of magnitude (see Fig. 2.2). A very high luminosity is required to allow reasonable statistics for rare processes. On the other hand, the rate of events at LHC,

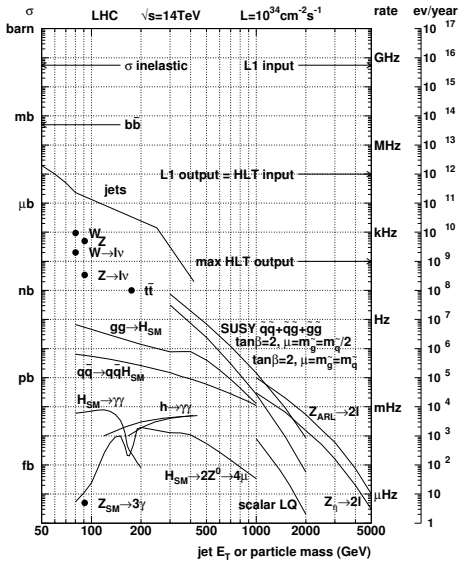

Figure 2.2: Inclusive proton cross section for basic physics processes. Interaction rates for the nominal luminosity are given on the right hand scale.

which is dominated by background events, is several order of magnitude larger than the maximum allowed for the data storage devices. The total inelastic pp cross-section is indeed estimated to be $\sigma_{inel} \sim 100$ mb, which corresponds to an average of 10^9 interactions per second in the LHC conditions. Therefore, a strong online selection is required to reduce by $\sim$7 orders of magnitude the interaction rate before the storage on disks. A very high time resolution is also needed to distinguish events belonging to different bunch crossings separated by only 25 ns.

The second challenge comes from the very dense particle environment. At high luminosity running, approximately 20 interactions are expected for each bunch crossing. A typical minimum bias collision at LHC will produce on average 5.5 charged particles with $\langle p_T \rangle \sim 0.5$ GeV and 8 primary (i.e. not emitted from particle interactions with matter, or from particle decays) photons per unit of pseudorapidity. The interesting signals, containing high p_T leptons, high E_T hadron jets, $b-$jets or large missing transverse momentum will always be superimposed on such a background. Therefore, detector units must be finely segmented to separate particles very close in space. Sophisticated algorithms are also required to reconstruct particles in such a high density environment. Lastly, several technological restrictions apply to detectors which are supposed to withstand the high radiation dose expected at LHC.

As said before most of the processes under investigation would provide final states with leptons, hadron jets from quark fragmentation and missing energy. Therefore, the basic detector requirements for ATLAS and CMS are:

- almost full hermeticity to allow missing transverse momentum reconstruction (and thus identify neutrinos and neutralinos);
- capability to reconstruct muons in a large range of p_T and rapidity (to reconstruct Z, W and tag b-jets);
- possibility to reconstruct electrons and photons (electrons from Z, W and photons mainly for $H \rightarrow \gamma\gamma$ search);
- possibility to reconstruct charged tracks with good p_T and impact parameter precision for Bs and τs reconstruction and tagging;
- possibility to reconstruct hadron jets from QCD processes and heavy particles decays (t, Z, W, H, SUSY particles).

Part of the reconstruction should be performed at the trigger level to reject the large background which is present in LHC events.

2.2 The CMS Experiment

The Compact Muon Solenoid (CMS) is designed to fulfill all requirements listed above. Its layout is sketched in Fig. 2.3. The apparatus has a cylindrical symmetry around the beam direction. It is made out of several layers of detectors around the beam in the central region (*barrel*) and several disks (*end-caps*) in the forward regions to allow a nearly hermetic coverage. The inner part of the apparatus is contained in a superconducting solenoid (7 m diameter, 12 m long) which provides a uniform 4 Tesla magnetic field for charged particles bending. The Tracking system and most of the Calorimetry are fully contained inside the magnet. Two very forward calorimeters extend the coverage up to $|\eta| < 5$. A complex system for muon detection is placed inside the return yoke of the magnet. Indeed the iron slabs used to filter the muons and to house the muon detectors act as a return yoke for the CMS magnetic field.

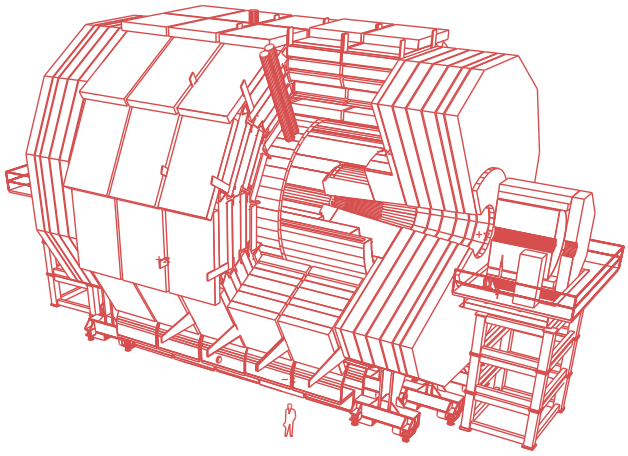

Figure 2.3: Overview of the CMS detector

2.2.1 The Magnet

The goal of the CMS magnet[52] is to provide a 4 Tesla magnetic field to bend charged particles and thus provide the transverse momentum measurement. To achieve this goal a superconducting magnet has almost been completed. The Magnet system includes a cryogenic system, power supply, quench protection, vacuum pumping and control system. The coil is inserted inside the cryostat and consists of the windings with its structural support, the thermal radiation shield and vacuum tank. The conductor consists of three concentric parts: the central flat superconducting cable, with high purity aluminium stabiliser, and two external aluminium-alloy reinforcing slabs. The superconducting cable is of Rutherford type and contains 40 NiTb strands.

2.2.2 The Tracker

The Tracker [53][54] is the subdetector system which is closest to the interaction point. Its goal is the reconstruction of charged tracks and vertices. The main physics goal of the Tracker are the reconstruction of the primary vertex, the matching of charged tracks with Calorimetry and Muon system for lepton identification and secondary vertices reconstruction for B and τ decays detection. It is thus a key device for searches for new particles (e.g. $H \rightarrow b\bar{b}$, $H \rightarrow ZZ \rightarrow 4l$, SUSY searches, primary vertex reconstruction for $H \rightarrow \gamma\gamma$) and Standard Model physics (e.g. study of the properties of the top quark and

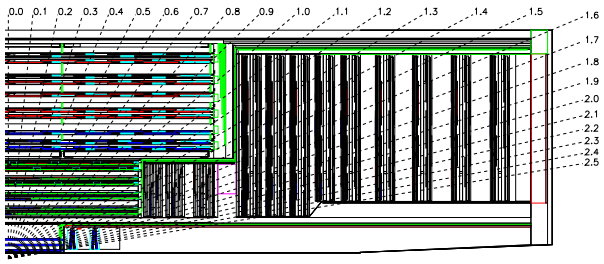

Figure 2.4: Layout of the Tracker.

of CP violation in B decays). A Tracker completely based on semiconductor detectors was designed for these purposes and its layout is shown in Fig. 2.4. The innermost part of the Tracker is made of silicon pixel detectors to provide a good precision in the extrapolation to the primary vertex. According to the base design, the barrel part is made of three layers of pixel detectors while the end-caps are made of two pixel disks. The pseudorapidity range covered by the pixel detector is $|\eta| < 2.4$.

The intermediate and outer parts of the Tracker are made of Silicon microstrip detectors of different design and thickness. The total numbers of barrel layers and forward disks are 4 and 3 in the intermediate Tracker and 6 and 9 in the outer Tracker. These parts of the Tracker allow an efficient pattern recognition, a precise measurement of the particle momentum and a good matching with the outer detectors.

The general tracking performance is the following:

1) P_T resolution in the $|\eta| < 0.7$ region is better than $\delta p_T / p_T \sim (15\, p_T \oplus 0.5\,)\%$ with p_T measured in TeV. The p_T resolution is slightly worse in the forward region.

2) Efficiency for reconstructing single muons is greater than 98% all over the η coverage, while for electrons with $p_T > 10$ GeV/c is around 80%.

3) Efficiency for reconstructing hadrons inside jets is around 80% for $p_T > 1$ GeV/c and around 95% for $p_T > 10$ GeV/c.

4) Resolution in transverse impact parameter for reconstructed tracks is about 20 μm for 10 GeV particles.

5) This high tracking efficiency makes the detector suitable for b and τ identification. The possibility to read a single region of the apparatus permits to lower the time needed for reconstruction and allows the use of the tracker in a very early stage of the trigger system.

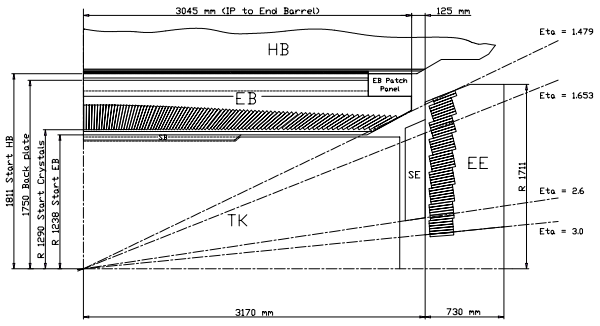

Figure 2.5: Layout of the Electromagnetic Calorimeter

2.2.3 The Electromagnetic Calorimeter

A complex Electromagnetic Calorimeter (ECAL) [55] is used for electron and photon reconstruction. The main goal of ECAL is to reconstruct the process $H \to \gamma\gamma$. The subsystem was designed in order to achieve the best sensitivity for this process.

ECAL is made out of several arrays of $PbWO_4$ crystals. This material is suitable to work in the LHC conditions since it is radiation resistant and chemically inhert. Moreover, it has a very short decay time ($\sim$ 10 ns) for scintillation radiation emission and allows 85% light collection in 25 ns. The layout of ECAL is shown in Fig. 2.5. A cylindrical barrel covers the region defined by $|\eta| < 1.48$, while two end-caps cover the forward region up to $|\eta| < 3$. The crystals have a very short radiation length of 0.89 cm which allows a very compact crystal. Barrel crystals are 23 cm long: this length corresponds to 26 radiation lengths and allows an almost complete shower containment. The cross section of the crystals is 22×22 mm^2, at the front face, throughout all calorimeter. In the barrel region this corresponds to a granularity $\Delta\eta \times \Delta\phi \sim 0.0175 \times 0.0175$ which is high enough to separate photons from π^0 decay up to π^0's energy of 20 GeV. The granularity decreases with η and reaches a maximum of $\Delta\eta \times \Delta\phi \sim 0.05 \times 0.05$ in the very forward crystals. To increase the π^0 rejection power in the forward regions, a silicon detector preshower will be placed in front of the end-caps. Since the preshower will be 3 radiation lengths deep, the end-cap crystals length will be reduced to 22 cm. The cross section of these crystals is 24.7×24.7 mm^2.

The light from the barrel crystals is collected by avalanche photodiodes (APD).

These devices are able to work in the presence of a high transverse magnetic field. In the end-cap regions the radiation dose will be much higher, hence vacuum phototriodes (VPT) were chosen to read out the signals.
The energy resolution that can be achieved by ECAL can be parametrised according to the formula, with Energy measured in GeV:

$$\frac{\sigma_E}{E} = \frac{a}{\sqrt{E}} \oplus b \oplus \frac{\sigma_N}{E}, \tag{2.3}$$

where the first term is the contribution due to the statistical fluctuations of the shower, the second one is due to calibration and the third one to electronics and pile-up. The design parameters are: $a = 2.7\%$, $b = 0.55\%$ and $\sigma_N = 155$ MeV for the barrel crystals while $a = 5.7\%$, $b = 0.55\%$ and $\sigma_N = 770$ MeV for the end-cap crystals [55].
It was recently envisaged the possibility of a staged ECAL scenario at the beginning of data taking due to a longer time scale required for the construction of the crystals. In the backup ECAL detector layout one or both end-cap calorimeters are staged by some months keeping only the preshower in the forward regions. The impact on dijet mass resolution and E_T is negligible[56].

2.2.4 The Hadron Calorimeter

The purpose of the Hadron Calorimeter (HCAL) [57] is to achieve a good jet energy resolution, a precise measurement of the jet direction and missing transverse momentum. Therefore, the detector must be thick enough to fully contain the hadronic shower, have a good transverse granularity and be completely hermetic.
The CMS Hadron Calorimeter is a sampling calorimeter with active layers alternated with absorbers. Active layers are made out of plastic scintillators, while absorbers are made out of Brass. The overall thickness varies from 8.9 interaction lengths in the barrel region up to 10 in the end-caps.
A scheme of HCAL is shown in Fig. 2.6. A *tail catcher* is placed outside the magnet to improve the shower containment at $\eta = 0$. Scintillators are arranged in projective towers with a granularity $\Delta\phi \times \Delta\eta = 0.087 \times 0.087$ to guarantee an efficient two-jet separation. The coverage extends up to $|\eta| < 1.4$ for the barrel and $1.4 < |\eta| < 3$ for the end-cap.
According to test-beam data [59], the expected energy resolution for pions

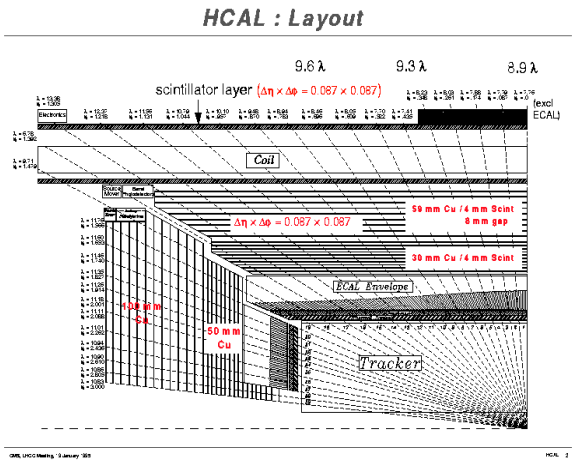

Figure 2.6: Layout of the Hadron Calorimeter

interacting in HCAL is:

$$\frac{\sigma_E}{E} = \frac{94\%}{\sqrt{E}} \oplus 4.5\%, \tag{2.4}$$

and for pions interactin in ECAL and HCAL is:

$$\frac{\sigma_E}{E} = \frac{83\%}{\sqrt{E}} \oplus 4.5\%. \tag{2.5}$$

where Energy is measured in GeV. A degradation of the response is expected at $|\eta| \sim 1.4$: in this region, the amount of inactive material is higher due to the presence of services and cables.

A very forward calorimeter (VFCAL) is placed outside the magnet to extend the hermetic coverage to the region between $3 < |\eta| < 5$. It is also a modular sampling calorimeter made of quartz crystals alternated with Brass. The granularity of VFCAL is $\Delta\eta \times \Delta\phi = 0.17 \times 0.17$. The forward calorimetry is expected to provide an energy resolution of

$$\frac{\sigma_{E_{had}}}{E_{had}} = \frac{172\%}{\sqrt{E_{had}}} \oplus 9\%, \qquad \frac{\sigma_{E_{em}}}{E_{em}} = \frac{100\%}{\sqrt{E_{em}}} \oplus 5\% \tag{2.6}$$

for hadrons and electrons respectively (Energy is measured in GeV) [57]. The energy resolution for jets can be parametrized with the following formula, after the energy calibration:

$$\sigma_{E_T}/E_T = 1.18/\sqrt{E_T} + 0.07$$

at low luminosity and

$$\sigma_{E_T}/E_T = 1.56/\sqrt{E_T} + 0.05$$

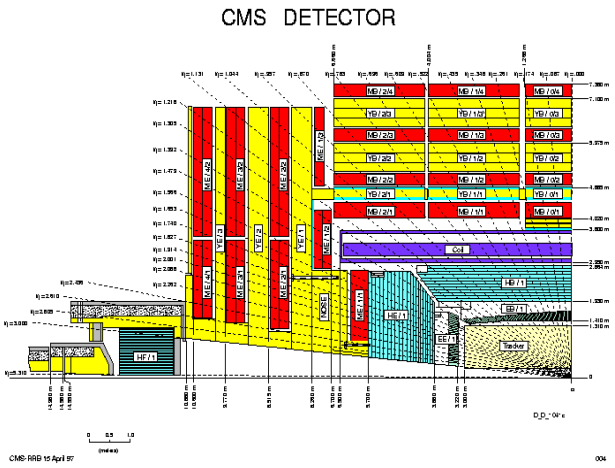

Figure 2.7: Layout of the muon detection system

at high luminosity, where E_T is the transverse energy of the jet measured in GeV.
The difference in the reconstructed jet direction with respect to the generated jet direction is less than 0.04 radiant for jets with transverse energy greater the 50 GeV [58].

2.2.5 The Muon System

A huge muon detection system [60] is placed outside the magnet coil. Its purpose is multiple: it allows muon identification and measurement of their momentum, it provides the trigger signal for events with muons as well as a precise time measurement of the bunch crossings. The layout of the muon detection system is sketched in Fig. 2.7. The muon detectors are integrated in the iron return yoke of the magnet. Both barrel and end-caps are made out of four active layers and three planes of absorber.
The barrel region extends up to $|\eta| < 1.3$. It is divided longitudinally in five segments. Each detection unit houses 12 layers of Drift Tube (DT) with approximately 400 ns drift time and a time resolution of 5 ns.
Tubes are arranged in 3 modules of four layers each. The first and third modules provide a ϕ measurement while the central one provides the z measurement. Layers of the same module are staggered by half cell to compute the coordinate and the angle of the crossing tracks. A certain redundancy

guarantees full coverage even in the presence of dead regions. The DT spatial resolution is 250 μm per tube and an overall resolution of 100 μm in $R-\phi$ and 150 μm in z is expected. The system is fast enough to allow the measurement of muon position and to compute its direction in the Level-1 Trigger.
End-caps extend the coverage up to $|\eta| < 2.4$. The active layers are equipped with trapezoidal shaped Cathode Strip Chamber (CSC) detectors. With the exception of the first layer, which has three detector rings, the other layers are made out of an inner disk of 18 detectors covering 20^0 in ϕ and an outer disk of 36 detectors covering 10^0 in ϕ. The last detector layer is followed by an iron layer, 1 cm thick, to protect detectors from radiation coming from the accelerator.
Each chamber is made of 6 sandwiches of cathode strips and wires which provide three-dimensional reconstruction. CSC are designed to operate in non uniform magnetic field ranging from 1 to 3 Tesla. The spatial resolution varies from 75 μm, for the first two inner layers, to 150 μm for the outer ones. CSC informations is available at Level-1 Trigger. The time resolution of CSC is 6 ns. Bunch crossing identification is also provided by CSC.
An additional muon Trigger is provided by the Resistive Plate Chambers (RPC). RPC detectors have excellent time resolution ($\sigma \sim 1-2$ ns). There is a plane of RPC detectors for each layer of CSC detectors in the end-caps and for the first, second and fourth layers of DT detectors in the barrel.
Each RPC chamber in the barrel is made of two phenolic resin planes separated by a gap of a few mm filled with gas. Planes are coated by a conductive graphite paint in the shape of electrodes. Signals are induced on plastic insulated aluminum strips outside the resin plates. These devices operate in avalanche mode to cope with the LHC high rate, but have worse spatial resolution than the CSC and the DT.
The spatial resolution of the overall muon system is of the order of few mm, while the intrinsic p_t resolution is $\Delta p_T/p_T = 8-15\%$ for $p_T = 10$ GeV/c muons and $\Delta p_T/p_T = 20-40\%$ for p_T up to 1 TeV/c. The matching with track segments in the Tracker allows to improve the resolution to less than 1% for 10 GeV muons.

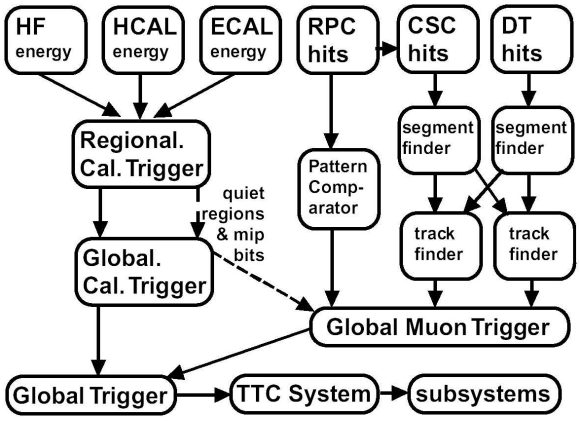

Figure 2.8: Overview of the Level-1 trigger flow.

2.2.6 The Trigger

A very complex Trigger System is being designed to reduce the 40 MHz event rate down to a value around 100 Hz which is considered the maximum that could be archived by a computer farm. This system is the start of the physics analysis selection. Due to the 7 orders of magnitude which separate the LHC collision rate from the acquisition rate, the Trigger System has a very complicated structure. It must be very performant in terms of signal efficiency and background rejection and very fast. It operates in several steps applied in cascade. A very coarse and fast decision is taken at low level to remove the bulk of the background, while more precise reconstruction is performed at higher levels.

The lowest level Trigger, called *Level-1* Trigger, is entirely based on hardware. It allows to reduce the event rate from 40 MHz to 100 kHz.

It is based exclusively on Calorimetry and Muon System informations. It has first a *regional* phase, where Calorimeter and Muon data are analysed locally to achieve a coarse reconstruction of jets and leptons, then the informations are combined together to extract the missing transverse momentum. An overview of the process is displayed in Fig. 2.8. The Calorimeter Level-1 Trigger works as follows: individual ECAL, HCAL and HF Trigger Primitive Generator (TPG) circuits provide coarse calorimetric towers and send them to the Regional Calorimeter Trigger (RCT) which reconstructs jets, leptons and photons to be sent to the Global Trigger (GT). It also provides the map of inactive calorimetry regions to improve the muon isolation.

In the meantime, the muon tracks are reconstructed independently by the RPCs and the Drift Tubes or the CSCs. Informations are then combined together by the Global Muon Trigger (GMT) to resolve ambiguities and to remove fakes. GMT and GCT are again combined to calculate the missing transverse momentum and they determine the regions where High Level Triggers should focus on.
The Level 1 accepted signal is distributed to the subsystems: front-end electronics was designed to store data in 3.2 μs pipelines (corresponding to 128 bunch crossings) which is the Level-1 decision time and send them to the PC farms only in case of Level-1 accepted signals.
High Level Triggers (HLT) are being designed to reduce the Trigger rate from 100 kHz to 100 Hz. This reduction is entirely accomplished via software through some dedicated PC-farms in many steps, for example *Level-2* and *Level-3* Trigger refine lepton and jet reconstruction [62]. Tracker hits are already available at Level-2: primary vertex from pixel hits [63] and track reconstruction are used to clean the Level-1 sample, increasing the purity of events with τ lepton and b quark final states. Tracking is also used in dedicated triggers for selected exclusive channels improving the statistics for rare processes.
Chapter 4 describes the use of tracking and calorimetry for a dedicated τ trigger chain, essential to increase the discovery potential of CMS.

Chapter 3

The CMS Tracker

For the study of physical channels as the one presented in this thesis, the tracker has a fundamental role in the reconstruction analysis. The calorimeters are needed to reconstruct the jets and the electrons, but they would be of little use without tools that can identify the b-flavoured jets or the hadronic decays of τ leptons. The only subdetector which can ensure good tagging efficiency and a high background rejection factor is the tracker system.
In this chapter the instrumental aspects of the problem and the track reconstruction are explained; the application to the radion signal are described in the following chapters.
An introductory part is provided to further motivate the necessity of this system. The main technical details are then discussed focussing on the most innovative ones.
The last section reports the study of the silicon electronic chip behaviour under laser induced Highly Ionizing Particles, to which the candidate gave an essential contribution.

3.1 Physics and Experimental Requirements

A robust tracking system has played a crucial role in all accelator experiments in the last decade and still will be a key element at LHC.
A measurement of track parameters is required by many physics studies. In particular, a precise measurement of the transverse momentum allows to reconstruct resonances and to measure invariant masses. In addition, the ex-

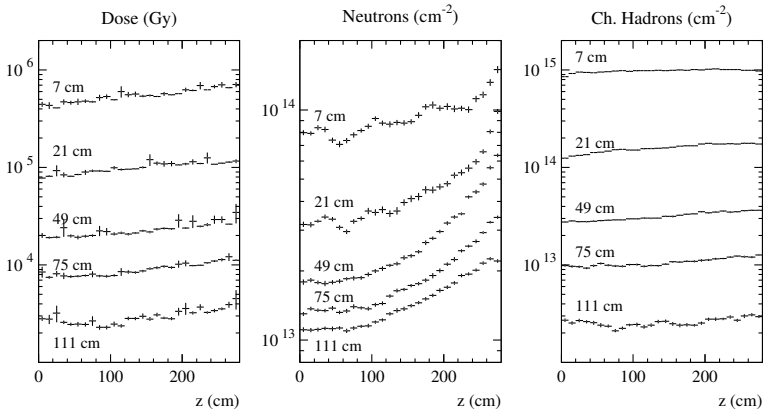

Figure 3.1: Radiation levels at selected radii in the CMS Tracker region. All values correspond to an integrated luminosity of 500 fb^{-1}.

trapolation of the track parameters to the calorimeters and the muon system helps in electron, hadron and muon identification. The precise extrapolation towards the interaction point is crucial for primary vertex reconstruction and for the identification of the hadronic decays of the τ lepton. Tracks with a large impact parameter with respect to the primary vertex will also be used to reconstruct secondary vertices and to tag jets from b quarks.

The complexity of the final states at LHC and the harsh conditions where the CMS detector will operate translate in very challenging requirements for the tracking system.

First of all, the very high particle density of the events requires highly segmented detectors. Particles in jets can produce hits very close in space and the pattern recognition algorithms can fail in associating them to the corresponding tracks. A sizeable effect on the measurement of track parameters would be thus expected. Since the particle density is higher in the innermost detector layers, the granularity must increase when decreasing the radius. Since many hits per track are needed to achieve a good pattern recognition and transverse momentum resolution, a very large number of readout channels is required. On the other hand, the amount of material crossed by particles (*material budget*) should be kept as low as possible to keep secondary interactions and conversions at an acceptable level in order not to spoil the tracking performance. A compromise between a large number of hits and a reasonable material budget is then required.

As a consequence of the large total cross section and high luminosity, the

radiation levels foreseen for the tracking system will also be higher than in previous experiments. Fig. 3.1 shows radiation dose and fluence of neutrons and charged hadrons foreseen for a 500 fb^{-1} integrated luminosity in different radial and longitudinal regions of the Tracker. For example, a layer of Silicon-strip detectors, placed at 22 cm from the interaction point, will experience a fluence of 1.6×10^{14} 1 - MeV - equivalent neutrons per cm^{-2}. To survive in this environment, both the sensitive and the readout electronics should be radiation resistant.
Finally, the tracker detectors must have a time resolution good enough to distinguish events belonging to different bunch crossings.

3.2 The Tracker Layout

In order to fulfill the above requirements, the CMS Tracker is completely based on silicon detectors [53, 54]. Silicon detectors are very compact devices that provide an excellent position resolution ($\sim 10\mu m$) with a reasonably good time resolution ($\sim 10ns$). For these reasons they have been succesfully used so far as microvertex detectors. In CMS, for the first time in high energy physics, they will be used to instrument a complete Tracker. The extensive R&D work performed by the CMS Collaboration has made it realistic. Low cost and simpler production processes have been developed to produce a very large number of detectors ($>$ 25,000) in a reasonably short timescale (2.5 years) [64, 65, 66, 67, 68]. A careful tuning of the detector design has been performed to optimize the performance in different regions of the system.
A detailed description of the principles of operation of silicon detector and their behaviour under heavy irradiation is not in the scope of this work. A comprehensive review can be found in [69].
Silicon detectors are large area planar diodes based on a n-type substrate with p^+ implants on the surface. The entire thickness of the sensors can be fully depleted by operating the diodes in reverse bias.
A particle interacting with the silicon bulk creates electron-hole pairs. Due to the electric field perpendicular to the surface, electrons and holes drift towards the electrodes and produce signals that can be amplified. For a minimum ionising particle crossing a 300 μm thick device, $\sim$ 24,000 electron-hole pairs are generated. According to the shape of the electrodes, different information

about the particle impact point position can be extracted.
In the CMS experiment two different silicon devices are foreseen: pixel and microstrip detectors. In pixel detectors the electrodes are shaped as small rectangles and provide a three dimensional reconstruction of the track impact point: two informations are provided by the fired cell and the third one comes from the radial position of the sensor itself.
In microstrip detectors the implant are shaped as arrays of strip. A coordinate is provided by the fired strip and the second one comes again from the position of the sensor. The three dimensional information can be recovered by placing two detectors back-to-back with tilted strip directions. This stereo coordinates provide a worse resolution compared to that provided by the pixel detector but the number of readout channels is much smaller. As the other subsystems of CMS, the Tracker has a cylindrical symmetry around the beam line. The tracking volume is a cylinder of 1.1 m radius and 5.6 m in length. Detector units are arranged in cylindrical layers around the beam line and disks in the end-cap regions. The granularity of the detectors depends on the distance from the primary interaction: in the innermost layers, the hit density is very high and a finer granularity is needed to improve the two track resolution and to allow the extrapolation to the interaction point. In the outer layers, the hit density becomes lower, while the sensitive surface increases. A lower granularity is therefore sufficient to provide the expected performance and it is indeed compulsory to limit the number of readout channels. The microstrip detectors, in the central region (the barrel) are rectangular with the strips parallel to the beam direction, while end-caps detectors are trapezoidal with radial strips. So barrel detectors provide the ϕ and r coordinates of the impact point while the end-cap detectors provide the information on ϕ and z.
In the low luminosity run, three cylindrical pixel layers will be placed at 4, 7 and 11 cm from the beam line and two disks in each end-cap region. The pixel layers will be moved to 7, 11 and 13 cm in the high luminosity run to cope with the higher radiation dose. The pixel rapidity coverage in this configuration extends up to $|\eta| < 2.4$. A sketch of the pixel detector is shown in Fig. 3.2. The Silicon-strip Tracker is divided in two parts: an inner and outer part with different types of microstrip sensors. The inner Tracker is made of 4 layers and 3 disks for each end-cap region. The outer Tracker has 6 layers in the barrel region and 9 disks in each end-cap. The first 2 layers and the first 2 rings in both inner and outer Trackers are double sided to allow a three

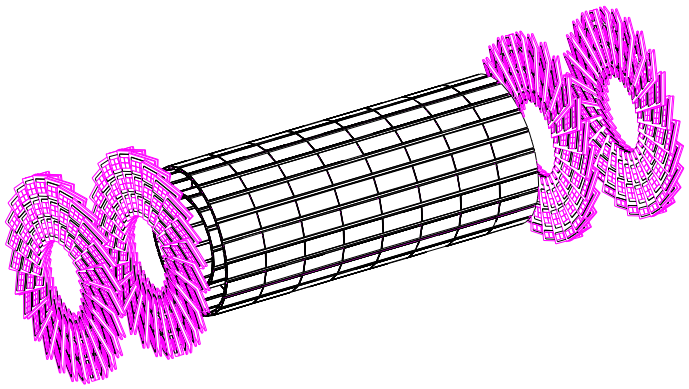

Figure 3.2: Scheme of the Pixel Detector

dimensional reconstruction. A sketch of the Silicon-strip Tracker is shown in Fig. 3.3. The first two layers of the inner and outer tracker are equipped with double sided stereo detectors. Figure. 3.4 shows a cross sectional view of the Tracker comprehensive of the supporting structures and services.
In comparison with other conventional tracking systems, the CMS Tracker provides a lower number of hits per track with a better position resolution. Sophisticated track reconstruction algorithms are being developed to perform the pattern recognition with a low number of precise hits in a very dense particles environment.
Another peculiarity of such complex devices comes from the large amount of material needed to readout and service a high granulairity detector. The material budget is calculated through a very detailed simulation, based on the GEANT package [70], which includes all known elements. The distribution of material expressed in radiation and nuclear interaction lenghts is shown in Fig. 3.5 as a function of η for the main Tracker components (left side) and the different functions of the material (right side). The distribution of the material in units of interaction lengths as a function of η is shown in Fig. 3.6 for the pixel detector (left) and the entire tracker (right). The material budget is higher in the transition region between barrel and end-caps ($\eta \sim 1$) due to cables and services which connect the Tracker modules to the outside systems.

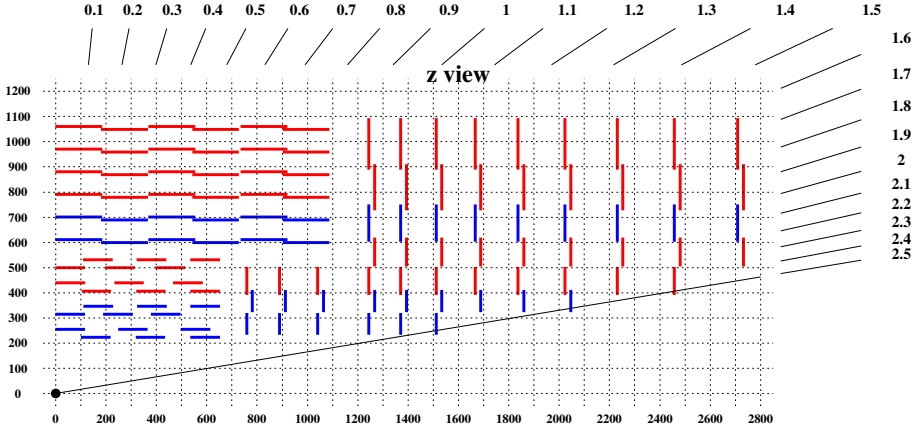

Figure 3.3: Layout of the Silicon-strip Tracker in the $r - z$ view. The first two layers of the inner and outer tracker are equipped with double sided stereo detectors.

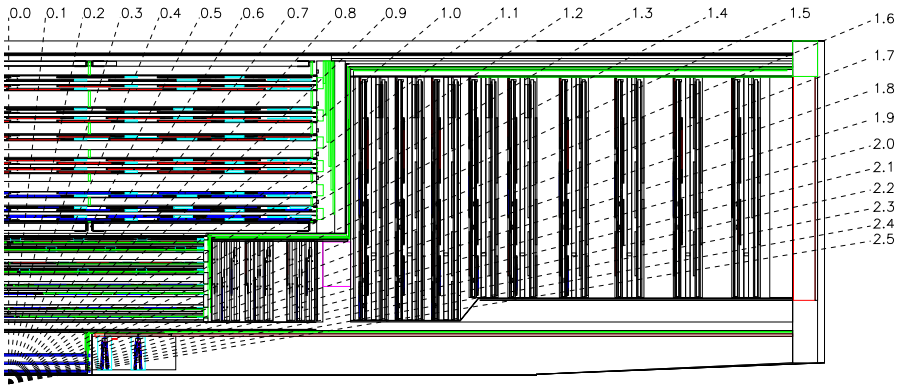

Figure 3.4: Schematic view of the Silicon-strip Tracker comprehensive of the supporting structures, cables and services.

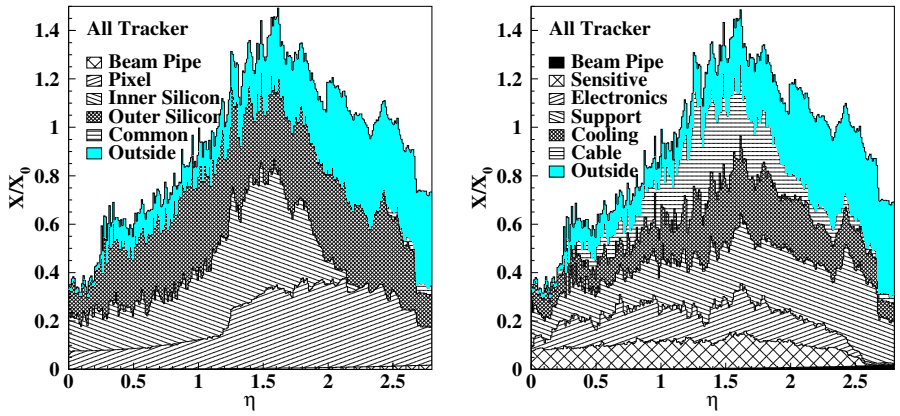

Figure 3.5: Tracker material budget in units of radiation length for the different components (left) and for the different functions of the Tracker (right).

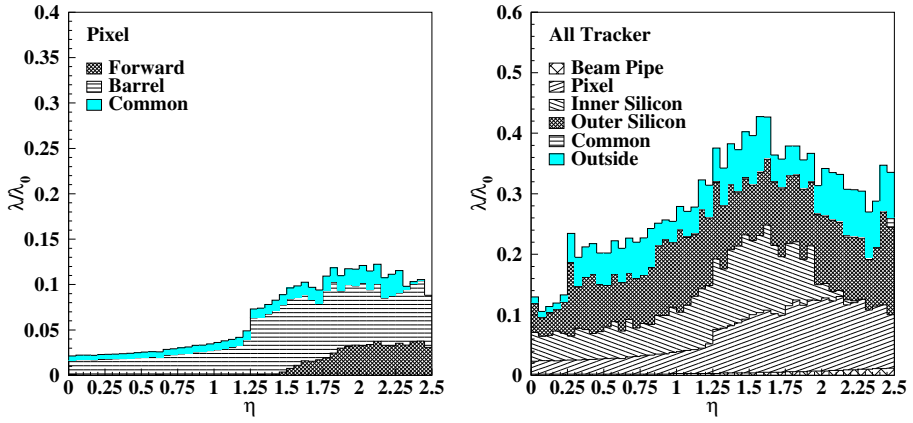

Figure 3.6: Tracker material budget in units of nuclear interaction length for the pixel sensor (left) and for the overall tracker (right).

3.2.1 Radiation Damage

A comprehensive review of radiation effects in semiconducting devices is outside of the scope of this work. A complete review can be found in [71]. Only the main parameters which affect the detector performance and play an important role in the definition of the layout and of the detector detailes of the silicon Tracker are discussed here.
The radiation damage effects can be divided in two main contributions: bulk and surface damage. The bulk damage is due to defects introduced in the crystal structure: as a consequence of knock-on collisions, atoms can be displaced from their original position in the lattice. A displaced atom can move to an interstitial position and create a vacancy. If the collision is hard enough, a nuclear reaction can occur and nuclear fragments can move in the lattice and start further displacements. Defects can combine and generate very complex structures.
The experimental results show that defects act as generation centers. One of the consequences of the bulk radiation damage is an increase of current through the junction (dark current). The increase in dark current density ΔI_v $(A \cdot cm^{-3})$ depends on the radiation fluence Φ according to the relationship:

$$\Delta I_v \quad = \quad \alpha\Phi, \tag{3.1}$$

α being a constant. After annealing effects (see below for more details), the value of α at 21^oC was estimated to be $\sim (2.9 \pm 0.2) \times 10^{-17} A cm^{-1}$ [72]. The main effect of an increase in dark current is a higher sensor noise. This effect can be reduced exploiting the strong dependence of α in temperature. For this reason the whole Tracker will be kept at a temperature of -10^oC during operation.
The presence of defects also degrades the Charge Collection Efficiency since they can trap the charge released by the interaction and thus reduce the charge collected by the electrodes. Since defects can act as acceptor centers, they also modify the effective dopant concentration N_{eff} linearly with the fluence. In particular when the fluence reaches the value:

$$\Phi_{inv} \sim (1.86 \pm 0.6) N^0_{eff}, \tag{3.2}$$

where N^0_{eff} is the effective dopant concentration before irradiation; an inversion of the material type from n to p type occurs [73].

A variation in the effective dopant concentration also requires a change of the operating voltage during the different periods of data taking. In the period after irradiation, the annealing behaviour of N_{eff} displays two distinct phases [74, 75]: an initial reduction in negative space charge (beneficial annealing), which is later dominated by a slower, but much larger, increase in acceptor concentration (reverse annealing). The rate of increase of reverse annealing has a strong dependence on temperatures and imposes strict limits on the operation temperature and the warm up maintenance periods.
Stable defects are also responsible for the so called surface damage: charges are trapped in the junction between the Si-SiO_2 layers. The trapped charge modifies the electric field and introduce new levels in the forbidden energy band. Charges released in the interaction are shared among several strips, spoiling the signal reconstruction. Moreover an increase of the interstrip capacitance enhances the overall electronic noise.

3.2.2 The Pixel Vertex Detector

For the first time in hadron collider experiments, CMS (and ATLAS) will use a microvertex system based on pixel detectors.
The scheme of a pixel detector is shown in Fig. 3.7. A pixel detector is made of a sensitive layer and a readout chip (ROC). The sensitive layer is a n-type Silicon crystal 285 μm thick with a continuous p^+ implant on the back and rectangular shaped ($100 \times 150 \mu m^2$) n^+ implant (pixel) in the front surface. Each pixel is covered by a special metalisation followed by a passivation layer with a bump pad window of $\sim 13 \mu m$ in diameter. Two p-implants with small opening at the opposite side sorround each pixel in order to reduce the nearest-neighbour capacitance. In the barrel region the magnetic field is perpendicular to the electric field, so the electrons produced in the silicon by crossing particles drift with a Lorentz angle of $\sim 32^o$ and the charge is collected by more than one pixel. In this way the charge sharing among different pixels can be exploited to improve the position resolution. In the end-caps, the electric field is parallel to the magnetic field. To mimic the effect of a Lorentz angle, the detector surface is tilted by 20^o around the radial direction to distribute the charge over several pixel units.
Each pixel is connected, through bump-bonding, to the Pixel Unit Cell (PUC) in the readout chip. Only one design of the readout chip is foreseen for all

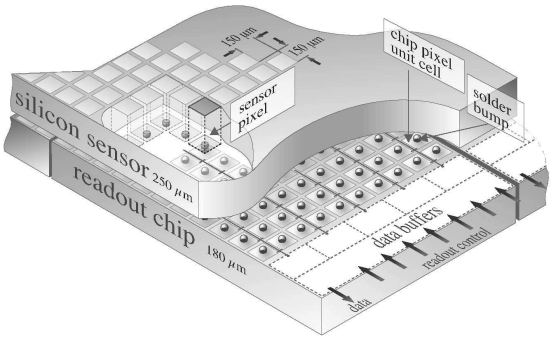

Figure 3.7: Schematic view of a pixel sensor.

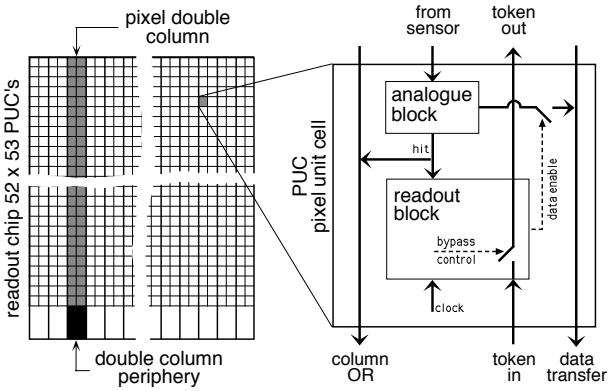

Figure 3.8: Schematic view of a pixel readout system.

geometries of the pixel modules: each chip has 52 columns and 80 rows of PUC and can read 4160 pixels.

The readout system [77] is sketched in Fig. 3.8. The main difficulty of the pixel readout system is to cope with a very large number of channels ($\sim 7.5 \times 10^7$); zero suppression is therefore required to reduce the huge data volume to a reasonable size. To this purpose, two nearby Pixel Unit Cell columns are read by one circuit placed in the pheriphery. The readout mechanim needs more than 25 ns to react and introduces a dead time of two clocks. The total inefficiency due to the overall readout system is 3.6% and 0.59% for layers at 4 and 7 cm respectively at low luminosity and Level-1 trigger rate of 100 MHz. These inefficiencies increase up to 12% and 3.6% at high luminosity at the same trigger rate while they go to 9% and 2.7% at a trigge rate of 30 MHz [76].

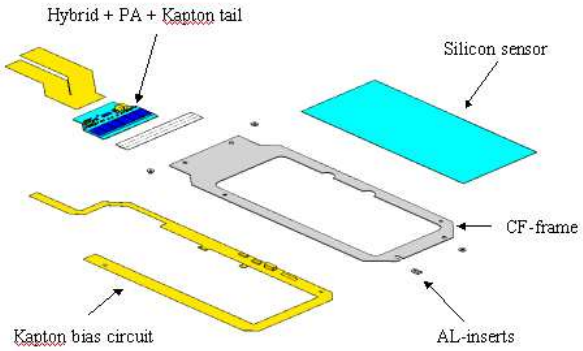

Figure 3.9: Layout of an inner barrel module.

The expected resolution of pixel sensors are 15 μm in both coordinates.
An R&D activity has been performed to design pixel detector components capable of operating in high radiation environment. Most of the solutions are common with the microstrip detectors so the discussion is reported in the next subsection.

3.2.3 The Silicon-strip Tracker

Silicon-strip Modules and Sensor Layout

The strip sensors are organised in detector units called modules. A Silicon-strip module is made of one or two sensors glued on a carbon fiber mechanical support with the strips micro-bonded to an array of readout chips (APV25 [78]) housed on a thin hybrid circuit. In the outer tracker modules two sensors are glued together and daisy chained while only one sensor is used in the inner tracker modules. Typical dimensions of the outer barrel modules are 96 $\times$ 190 mm^2, while smaller size modules (64 $\times$ 120 mm^2) are used in the inner part of the detector. A sketch of the assembly of an inner barrel module is shown in Fig. 3.9. The inner barrel sensors (also called thin sensors) are 320$\pm$20 μm thick while outer barrel sensor (thick sensors) are 500$\pm$20 μm. The larger thickness in the latter case allows to collect a larger signal which compensates the higher noise due to the larger capacitance introduced by the longer strips. In addition, the 500 μm thick sensors are produced by the industries in the 6$''$ commercial production lines with lower costs and shorter processing time.

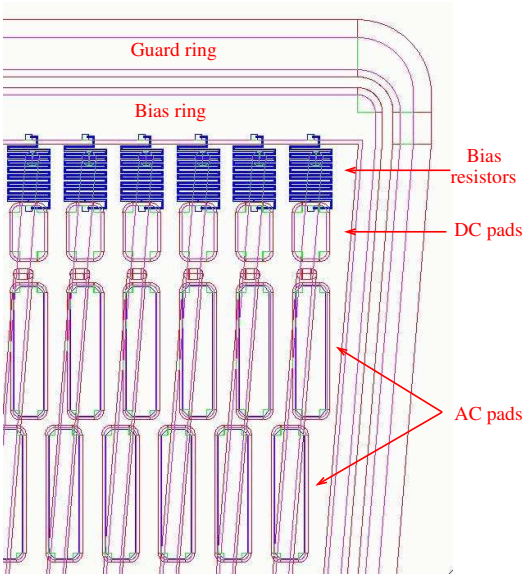

Figure 3.10: Corner of a microstrip detector sensor.

A corner of a Silicon-strip end-cap sensor is sketched in Fig. 3.10. The active area is surrounded by two p^+ implants, an inner one, the bias ring and an outer one, the guard ring. The inner ring is introduced to bias uniformly all strips through 1.5 MΩ polysilicon resistors. The outer one is introduced to limit the dark current from the sensor edges and thus improve the breakdown performance. A n^+ implant is also placed near the edge to limit the charge injection from the region damaged by the cut. On the side opposite to the strip, a n^+ implant connected to a thin aluminum layer covers the surface. A uniform deplation of the sensor is achieved by an inverse polarisation applied to the back plane while the junction side is connected to ground.
The strip signals are decoupled from the leackage current through capacitors integrated in the substrate (see Fig. 3.11). Capacitors are made by growing thin insulating dielectric layers between the p^+ implants and the aluminum electrodes. In all sensors the aluminum strips are larger than the p^+ implants in order to improve the breakdown performance [66, 67, 68]. The total number of microstrip modules is 15,232 (6,136 thin and 9,096 thick). The total number of electronic channels is 9,648,128 corresponding to 75,376 APV chips. The surface covered by the sensors is 206 m^2.

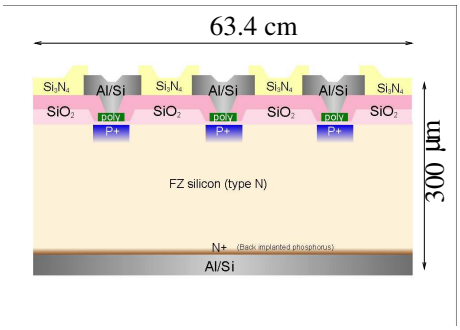

Figure 3.11: Cross section of a microstrip sensor (TIB).

Readout System

A scheme of the readout electronics [79] is shown in Fig. 3.12. The capacitor pads, which collect the strip signals, are connected to the 128 input channels of the APV circuit placed in the frontend hybrid. To adapt the different pitches of the sensors to the fixed pitch of the readout chip, a small circuit, the pitch adapter, is used. Each strip is read by a charge sensitive amplifier with a time constant of 50 ns, whose output voltage is sampled at the beam crossing rate of 40 MHz. Analog data are then buffered in 3.2 μs deep pipelines. If the bunch crossing event passes the Level-1 trigger selection, the pulse height signals are processed by analogue circuit, the APSP filter. If chips are operated in *peak* mode, the output is determined by the peak amplitude of the shaper output signal corrisponding to the trigger. If chips are operated in *deconvolution* mode the output signal is determined by the peak amplitude of the data as reshaped by the APSP. In deconvolution mode it is possible to recover the information of the bunch crossing which passed the Level-1 Trigger selection, minimizing the contamination from the other bunch crossings still present in the pipeline, but at the expense of an increased noise [80]. Figure 3.13 shows the average amplifier pulse shape for a range of (externally added) capacitance values in peak and deconvolution mode. The peak mode pulse shape shows a good approximation to ideal 50 ns CR-RC pulse shaping while the deconvolution mode illustrates the effectiveness of this techinque in achieving a pulse short enough to allow single bunch crossing resolution. Amplifiers, shapers, pipelines and APSP circuits are all integrated in the APV chip. Pulse height data are multiplexed from pairs of APV circuits onto a differential line over a short distance to laser driver transmitting at a wavelenght of 1,300 nm. Light signals are

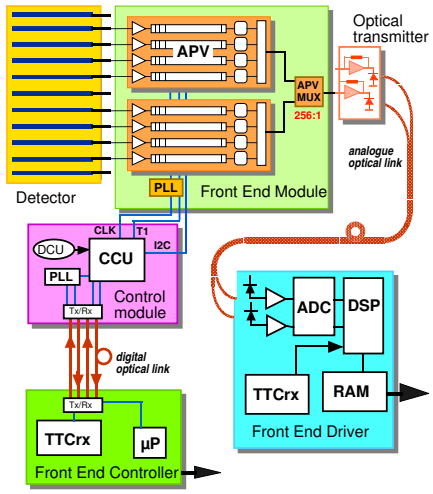

Figure 3.12: Scheme of a readout system for the Silicon-strip Tracker.

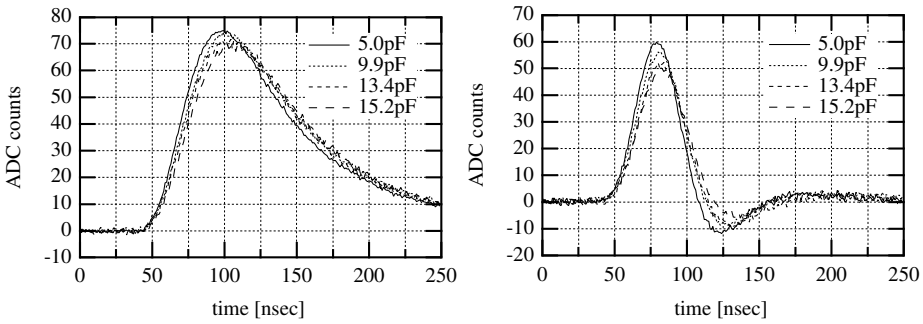

Figure 3.13: Analog pulse shape in peak (left) and deconvolution (right) mode.

then transmitted through a 100 m single mode optical fiber to the counting room adjacent to the cavern. The Tracker DAQ is based on a VME bus system. Pulse height data from the frontend chips, with no zero suppression, are converted back to electrical levels matching the range of a 10 bit ADC, which allows an adequate resolution over the expected signal range. The Front End Driver (FED) digitises the data, performs the signal processing that includes reordering and pedestal subtraction and stores data in a local memory until required by higher level data acquisition. In high luminosity conditions and maximum trigger rate an algorithm of cluster finding reduces the data volume to be transmitted.

The system is monitored by a VME bus module, the Front End Controller (FEC). The FEC acts also as an interface with the global Timing Trigger and

Command, which distributes the LHC machine master clock and the trigger signal. The clocks and triggers are transmitted from the FEC to the frontend hybrids through optical cables and distributed to a series of detector modules by Communication and Control Unit. The clock signals are locally recovered by Phase Locked Loop chips on each module to ensure high reliability and minimum phase jitter.
In the design of the CMS readout system, data are kept analog as long as possible to reduce the complexity of the frontend chip to reduce the power dissipation within the Tracker volume and to achieve a better position resolution through charge sharing between detector strips. The processing algorithms can be easily and inexpensively modified through programmable circuits in the FED.

Expected Performance

The performance of frontend electronics coupled to silicon detectors is related to the characteristic impedences of the sensors and the main geometrical parameters.
The channel noise is one of the main performance parameters. The main sources of noise are the thermal noise due to strip and metal resistance (R_s), the amplifier noise, the shot noise due to the reverse bias current (I_b) and the thermal noise of the bias resistance (R_p). The noise sources are indipendent and therefore the total noise is obtained by summing all contributions in quadrature. Table 3.1 shows the analytical formulas for the main noise contributions, in Equivalent Noise Charge (ENC) for an operating temperature of -10^{o}C, and the multiplicative factors needed to account for the deconvolution process. The noise due to front end electronics, which is added in series and is independent of the temperature, is shown in Tab. 3.2 for different types of chips used in these studies. The total noise is dominated by the frontend electronics contribution which is proportional to the total capacitance seen by the amplifier. The total capacitance depends on the sensor geometry. Several studies were performed to optimise the sensor geometry in order to keep the total capacitance as low as possible [54, 67, 68]. The total strip capacitance, C_{tot}, is about 1 pF/cm. The spatial resolution depends on the electrical and geometrical parameters. The expected resolution is around 20 μm for the inner detectors and 40 μm for the outer ones [81].

Noise Source	type	ENC (e^-)	ENC (e^-) @$T = -10^0 C$	deconvolution
Reverse bias current (I_b)	parallel	$\frac{e}{q_e}\sqrt{\frac{q_e \tau I_b}{4}}$	$\approx 108\sqrt{I_b(\mu A)\tau(ns)}$	$\times 0.45$
Polarisation Resistor (R_p)	parallel	$\frac{e}{q_e}\sqrt{\frac{kT\tau}{2R_p}}$	$\approx 22.5\sqrt{\frac{\tau(ns)}{R_p(M\Omega)}}$	$\times 0.45$
Metal Strip Resistance (R_s)	series	$\frac{e}{q_e}C_{tot}\sqrt{\frac{kTR_s}{6\tau}}$	$\approx 13 C_{tot}(pF)\cdot \sqrt{\frac{R_s(\Omega)}{\tau(ns)}}$	$\times 1.45$

Table 3.1: Noise sources, types and Equivalent Noise Charge (ENC) evaluation formulas. e is the Neper constant, q_e the electron charge, τ the shaping time and C_{tot} the total capacitive load.

Chip	ENC (e^-) in peak	ENC (e^-) in dec.
PREMUX-128	$558 + 41.5 C_{tot}$	-
APV6	$510 + 36 C_{tot}$	$10^3 + 46 C_{tot}$
APV25	$250 + 36 C_{tot}$	$400 + 60 C_{tot}$

Table 3.2: Equivalent Noise Charge (ENC) evaluation formulas for electronic noise in different chips in peak and deconvolution mode.

Radiation Hardening

Several strategies have been adopted to define a detector design and a processing technology which would allow good performance after 500 fb^{-1} integrated luminosity. The increase in dark current can be controlled by lowering the operating temperature during data taking. Moreover making the Tracker operate at low temperature, -10^o, all mechanisms of reverse annealing in damages silicon are freezed. The α value (i.e. the proportional constant between the radion flux and the dark current intensity) at -10^o is $\sim (1.4 \pm 0.2)\times 10^{-18}$ Acm^{-1}.

The variation in the effective dopant concentration is compensated by a change of the operating voltage during different periods of data taking which will be made possible by the use of high breakdown voltage devices ($V_{bd} > 500V$). Additional safety margins can be achieved with the choice of a lower bulk resistivity. The expected temporal evolution of the depletion voltage is shown in Fig. 3.14 for detectors with a standard resistivity (4kΩcm) and low resistivity

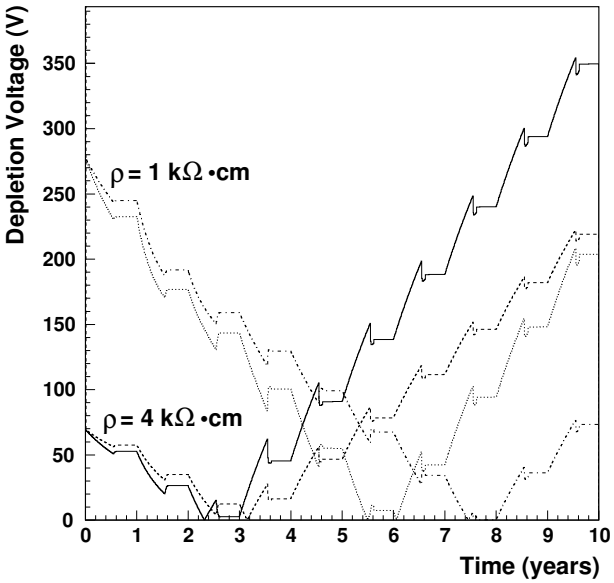

Figure 3.14: Predicted evolution of the depletion voltage with time for barrel layer 1 and two different initial resistivities. The pessimistic scenario is also shown for each initial bulk resistivity.

(1kΩcm). For each resistivity, the lower curves correspond to the expected fluence while the upper ones to a more pessimistic scenario with $\Phi = 2.4 \times 10^{14}$ 1-MeV-equivalent neutrons/cm^2 (1.5 safety factor). A low resistivity implies an higher bias voltage at the beginning of operation (V $\sim$ 300 V). On the other hand the substrate inversion would occur later and the required operating voltage after 10 years of running would be lower.
The surface effects are reduced by the choice of $< 100 >$ crystal lattice orientation, instead of the commonly used $< 111 >$, and by overdepleting the junction during operation. Finally, by operating the sensors at a very high bias voltage some increase in charge collection efficiency is also achievable [82].

3.3 Silicon-Strip Tracker Performance

An extended R&D activity has been performed by the CMS Collaboration to investigate the performance of the detectors designed for the Tracker and to study the impact of design modifications on the overall performance.
The performance has been studied with laboratory measurements and tests

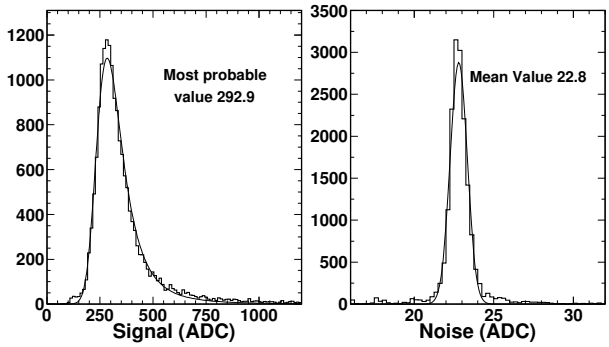

Figure 3.15: Signal and Noise distribution in ADC units at bias voltage 450 V for an irradiated module ($\Phi = 3.2 \times 10^{14} p/cm^2$).

under minimum-ionising particles beams.

3.3.1 Performance of Inner Barrel Detectors

The performance of the irradiated inner barrel detector has been evaluated with particles beams at CERN (X5 and T9 test beam facilities) in June 1999 with 120 GeV/c muons and 8 GeV/c pions [83]. Detectors were produced by CSEM (Neuchatel, Switzerland) with $< 111 >$ lattice orientation and 4-10 kΩcm bulk resistivity.
32 sensors were uniformly irradiated at CERN with 24 GeV/c protons to a fluence of 3.2 $\times 10^{14} p/cm^2$, which is equivalent to 10 years of LHC running. They were biased at 150 V during irradiation and kept at a temperature of -10^oC. No annealing was performed and sensors were kept at -25^oC after irradiation.
16 modules were assembled with these sensors and read with an ancestor of the APV chip (PREMUX [84] with a shaping time of 45 ns). A module was prepared with non irradiated sensors for comparison. Modules were placed in a climatic chamber able to accomodate up to 6 detectors; the temperature during data taking ranged from 0^oC to -40^oC. The chamber was placed in the middle of a telescope system made of standard silicon detectors for tracking purpose and two fast scintillators for triggering in coincidence.
The signal and noise distribution are shown in Fig. 3.15 for an irradiated module at 450 V bias voltage. The average noise as well as the signal to noise ratio are shown in Fig. 3.16 as a function of $V_{bias}/V_{deplation}$ for irradiated and non

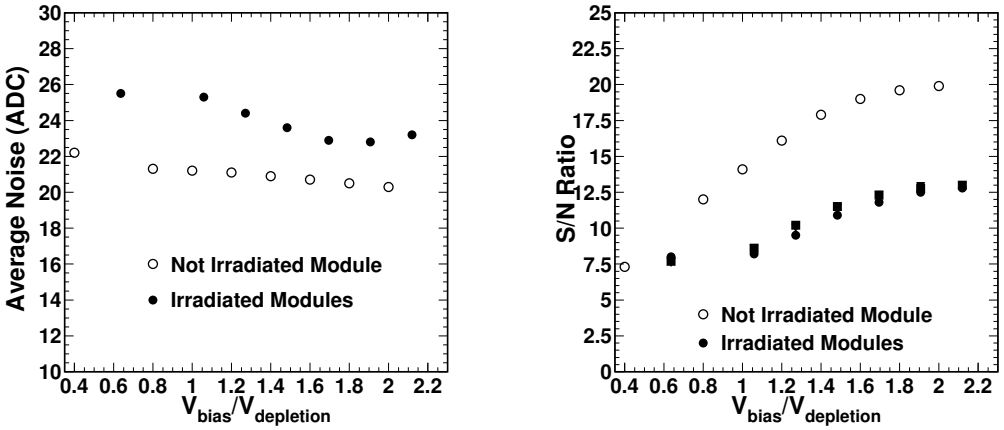

Figure 3.16: Noise (left side) and Signal to Noise ratio (right side) for an irradiated and a not irradiated module for different bias voltage.

irradiated detectors.

For the non irradiated module, the noise is approximately constant. In the irradiated one the noise is 10% higher due to the radiation damage: the noise decreases with $V_{bias}/V_{depletion}$ down to a minimum corresponding to a bias voltage 1.6 times higher than the depletion voltage. After this minimum the noise increases due to dark current. The signal to noise ratio tends to an asymptotic value of 20 for the non irradiated module and 12.5 for the irradiated one. The plateau is reached when the junction is already overdepleted.

The tracking performance was obtained through the telescope using the Newton algorithm [85]. Track segments were interpolated to the detector layers and the residual distributions were fitted with a gaussian function to extract the resolution. For the non irradiated and irradiated modules the measured resolution was 13.6 μm and 16.8μm respectively. Therefore, the spatial resolution is not dramatically spoiled by radiation damage.

Hit finding efficiency is shown in Fig. 3.17 as a function of $V_{bias}/V_{depletion}$: it is 99% for the reference module while it is 80% at $V_{bias} = V_{depletion}$ and increases up to 95% for $V_{bias} > 1.5V_{depletion}$, which is considered the standard operating condition in the experiment, for irradiated modules.

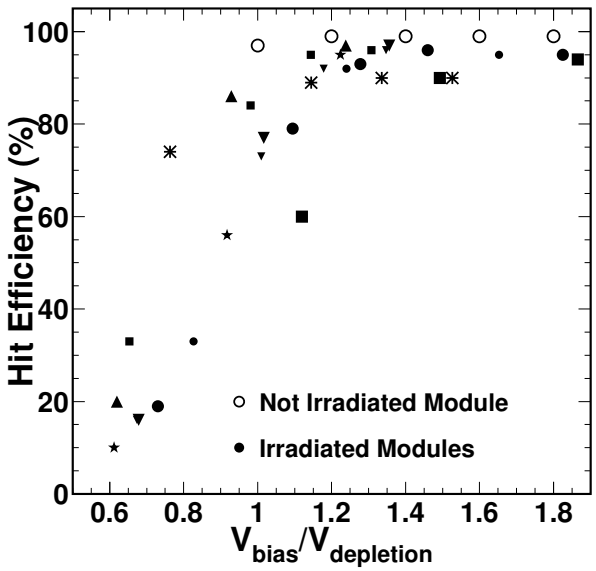

Figure 3.17: Hit finding efficiency for the not irradiated module and the irradiated ones for different bias voltage.

3.3.2 Performance of Outer Barrel Detectors

Detectors with thick sensors were tested for the first time in June 2000 at the CERN X5 beam facility [86, 87]. Sensors with 122 μm pitch were used for this test.

Irradiation was performed also with a neutron beam of 20 MeV at Louvain-la-Neuve (Belgium). The received dose corrisponds to $\sim 1.6 \times 10^{13}$ 1 MeV equivalent neutrons. The sensors were biased at 150 V and kept at -10^oC during irradiation and at -25^oC after irradiation to prevent annealing effects. Depletion voltage after irradiation is lower than 50 V.

Two modules with thick sensors were constructed: one with non-irradiated and one with irradiated sensor. APV6 chips (a previous approach to the final APV25) were used for readout in peak as well as in deconvolution modes. A 120 GeV/c pion beam with a bunch spacing of 25 ns (LHC like environment) was used for the test with a DAQ system very close to the final one.

Asymptotic values of signal and S/N are reported in Tab. 3.3 (for short strip detectors). The scaling of S/N with thickness, at fixed strip lenght, was confirmed for the first time in this test:

$$\frac{(S/N)_{thick}}{(S/N)_{thin}} \sim \frac{500\mu m}{300\mu m} \sim 1.6 \tag{3.3}$$

Module	Peak Mode		Deconvolution	
	Signal (ADC)	S/N	Signal (ADC)	S/N
300 μm	36	20	29	11
500 μm	58	45	49	23

Table 3.3: Measured values of signal and S/N ratio in peak and deconvolution mode for $300\mu m$ reference, 500 μm non irradiated and irradiated modules.

This relationship holds even after irradiation.

3.3.3 Performance on Tracks Reconstruction

Tracks reconstruction will be a very challenging issue in CMS because of the large number of particles per event. So it is very important to have a robust reconstruction algorithm with good efficiency and low fake rate in order to use the reconstructed tracks also in High Level Trigger algorithms as b and τ tagging.
Track reconstruction starts from the reconstructed hits in a portion of the Tracker. A *pattern recognition* or *seed generation* is the first step to find out groups of hits that can be associated to tracks. A fitting procedure is then applied to the track candidates to extract the values of the associated parameters. The parameters computed in this way are not necessarily the optimal ones: the inclusion of a wrong hit may spoil the fit and provide bad parameters. A *smoothing* phase is therefore invoked to adjust the values of the parameters: hits can be removed from the track candidate to improve the fit.
The main difficulty comes from the large number of hits per event ($\sim$ 4,000 at high luminosity and a factor 25 times lower at low luminosity). Special efforts are needed to limit the combinatorics as for example the implementation of a regional reconstruction which permits to consider only a geometrical region of the Tracker instead of the whole volume. The design of the algorithms depend on many aspects of the detector: shape of particles trajectories in magnetic field, type of hit information, geometry and performance of the detector. The algorithms must be flexible in order to be used both in the off line and in the High Level Trigger selections where the time which can be spent is much lower. This point will be better clarified in the next chapter.

Different track finders are foreseen for different types of particles: muons, electrons or tracks inside jets have different characteristics and need optimised algortithms to get the best reconstruction performance.
An object oriented framework called ORCA [88] was introduced to cope with this huge range of needs: object oriented software allows modularity in the architecture and the use of the same components and interfaces in different environments.

Detector Simulation

Events generated with pythia are passed to the CMSIM program to perform the detector simulation. CMSIM is a Fortran package based on the general purpose detector simulation GEANT3. A detailed model of the CMS detector is included in the simulation: the sensitive regions as well as the passive regions (electronics, mechanical supports, cables, cooling and alignment system) are reproduced with the correct material properties. The energies deposited in the sensitive regions are simulated according to the model of interaction of particles with matter. The electronics noise is then taken into account, inducing fluctuations on the value of the released energy and a detector output is returned in a raw data format. The parameters of the simulation are tuned in order to reproduce the test beam data.
In the tracker case, the signal-to-noise is set according to the parametrization made as a function of width over pitch of the detectors and dead strips are present at the level of 1%. The reconstructed cluster and hit positions are then passed to the reconstruction program to perform the track finding.

Track Reconstruction

Several track reconstruction algorithms are being developed by the CMS Collaboration. In particular, a modular track finder [89], based on a *Kalman Filter* [90, 91] has been proven to be optimal for track reconstruction in jets.
The reconstruction consists on four steps: *Trajectory seeding, Trajectory Building, Trajectory Cleaning* and *Trajectory Smoothing*. The trajectory seeds are raw trajectories whose parameters are estimated from a limited set of informations. They can be either internal or external to the Tracker. External

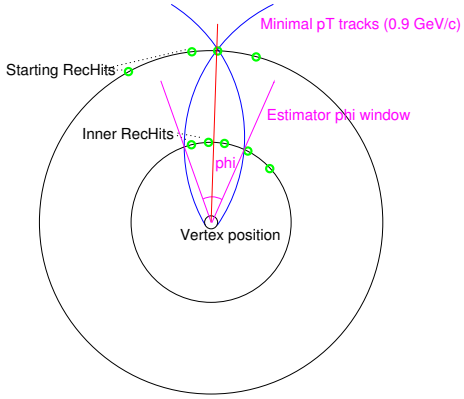

Figure 3.18: Definition of trajectory seeds in the track seeding phase.

seeds can be track segments measured with the muon system or seeds coming from the calorimeters, while internal seeds are produced by the Tracker alone. In this case the seeding starts from the hits in two innermost pixel layers: each pair of hits on the two layers are selected if they are compatible with the hypothesis of being generated by a track from the beam spot and with a minimum p_T, as sketched in Fig. 3.18. In this case the trajectory parameters are estimated and the track parameters and the associated hits constitute a *trajectory seed*. Presently only the pixel layers of the strip silicon tracker are used for internal seeding, but other algorithms that consider the two outmost layers are being studied. The next step is the *Trajectory Building*. This step is an iterative procedure: at the beginning of each step a trajectory is made from a number of associated hits (two if it starts from a trajectory seed) and with an estimate of the track parameters. The parameters are then etrapolated to a layer not yet included. If a reconstructed hit, compatible with the trajectory, is found in the layer, it is added to the trajectory itself and track parameters are updated. Trajectories which have at least two consecutive layers with no compatible hits are discarded. Iterations stop as soon as all layers are included. This procedure is known as Kalman Filtering. It does not involve iterative minimizations, as othe methods based on least squares fitting and allows to incorporate multiple scattering and energy loss in the propagation.
The *Trajectory Cleaning* is performed after each step of Trajectory Building to reduce the combinatorial background: if two trajectories share at least half of the associated hits, only the best one in terms of $\chi^2/n.d.f.$ is retained. This step allows to save CPU time and memory space.

After each step of Trajectory Building and Cleaning the track parameter precision increases. To obtain the best track parameters at the origin, the so called *Smoothing* phase is invoked: in this phase the tracks are fitted backwards and their parameters are recomputed at each previous point along the trajectory. The track reconstruction can be stopped at any moment either if the number of considered layers reaches a preselected value or if the track parameters reach the desired precision. In this way it is possible to save time and makes it possible to have track reconstruction available even in the High Level Trigger selection.

Primary Vertex Reconstruction

At low luminosity, about three secondary interactions are superimposed on average to the primary one, the so called pile-up events. These secondary interactions are usually minimum bias events and do not generate high p_T tracks. They can however degrade the tagging and isolation performance. It is therefore important to remove tracks coming from these interaction in order to consider only the tracks associated to the primary event. To do so, it is fundamental to reconstruct the vertices and to select the one associated to the primary interaction. Primary vertices are placed along the beamline: since the proton bunches have a spread $\sigma_x \sim \sigma_y \sim 15\mu m$, their position in the transverse plane is approximately $0\pm15\mu m$ in both coordinates while in the beam direction the spread is larger ($\sigma_z \sim 5$ cm). The primary vertices can be identified with good precision in multi-jet events because of the large number of charged tracks associated with them. There are several algorithms to reconstruct primary vertices but the fastest one uses tracks reconstructed with only the three pixel layers. This algorithm is 100% efficient at low luminosity and is essential for the b and τ tagging algorithms. Indeed, combining the possibility to limit the reconstruction region to a region of interest with the compatibility of seeds with the primary vertex is the fastest way, implemented at the moment, to reconstruct tracks in both low and high luminosity scenarios.

Track Finding Performance

Several samples of events have been produced to perform track finding performance studies. The samples are divided in single track events and di-jet

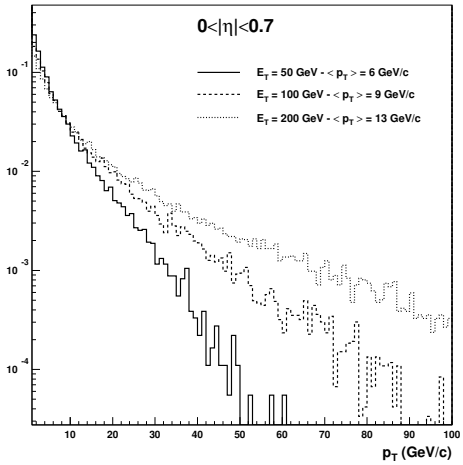

Figure 3.19: p_T spectrum for tracks in u-jets in the barrel region with E_T=50, 100 and 200 GeV.

samples. In all samples the primary interaction is generated with PYTHIA 6.152 [92]. The pile-up events were not considered in these studies.

- Single Tracks: single muon and pion tracks have been generated for many η bins and three p_T values (1, 10 and 100 GeV/c) to study the track finding efficiency and the accuracy on the track parameters. The very clean environment of these events have allowed to optimize the algorithms and to improve the detector design.

- Di-jet events: they have been generated in order to study the tracking performance in a dense environment. Jets have been produced in three different η bins, $|\eta|$ <0.7, 1.2 < $|\eta|$ <1.6 and 2.0 < $|\eta|$ <2.4 corrisponding to the barrel region, the overlap between barrel and end-caps and the very forward region. Different jet E_T bins, corrisponding to E_T=50, 100 and 200 GeV, have been taken into account: in the E_T=50 GeV the track p_T spectrum is softer, so the performance is limited by multiple scattering, while in E_T = 200 GeV jets the performance is affected by the very high particle density. The p_T spectrum for reconstructed tracks within a cone of ΔR <0.4 from these jets is shown in Fig. 3.19 and the mean p_T values are also reported.
  Jet momenta are provided by the PYTHIA's PYCELL routine. This routine performs a coarse simulation of the calorimeter response starting from the stable particle energy and momentum. The resolution and design of the CMS calorimeter are used.

The track reconstruction performance are evaluated in terms of reconstruction efficiency, fake rate and resolution on track parameters.
Two different definition of efficiency were introduced to decoupled the effect of the algorithms from the one of the overall tracking system: the *algorithmic efficiency* and the *global efficiency*. Both efficiency are defined as:

$$\epsilon = \frac{N(associated\ reconstructed\ tracks)}{N(simulated\ tracks)} \tag{3.4}$$

the denominator being the number of tracks which were simulated and the numerator the number of reconstructed tracks associated to the simulated ones. Reconstructed and simulated tracks are associated if they share at least 50% of the hits.
The algorithm can reconstruct with reasonable quality tracks which have at least 5 reconstructed hits, p_T >0.7 GeV/c and $|\eta|$ <2.5.
The requirements on simulated tracks depend on the type of efficiency under study. For what concerns algorithmic efficiency, the considered simulated tracks have at least 5 simulated hits, p_T >0.7 GeV/c, $|\eta|$ <2.4, while reconstructed tracks must have p_T >0.9 GeV/c, $|\eta|$ <2.4 and being associated to a simulated track. As the hit reconstruction efficiency is almost 100% any inefficiency would be due exclusively to the track reconstruction algorithms.
Looser cuts on simulated tracks (p_T >0.7 GeV/c and $|\eta|$ <2.4 without the requirement on the number of simulated hits) are used to compute the global efficiency which includes effects not depending only on the track finding algorithm (hit inefficiency or dead regions).
Algorithmic and global efficiencies are shown in Fig. 3.20 for muons and pions tracks with p_T=1, 10 and 100 GeV/c in the entire η range. The algorithmic efficiency for muons is always above 98%. The global one has a drop at very high η values because of the lower number of detector layers close to the edge of the Tracker. For pions of 1 GeV/c a drop in efficiency is observed around $|\eta|$ ∼1 because of the nuclear interactions induced by the higher amount of material.
Tracking performance is particularly important for hadronic jets since it can be spoiled by the very dense environment. The efficiency for tracks reconstructed inside jets even if slightly worse than the one for single particles, are always over 80%, reaching 90% in the barrel region.
The fake rate is defined by:

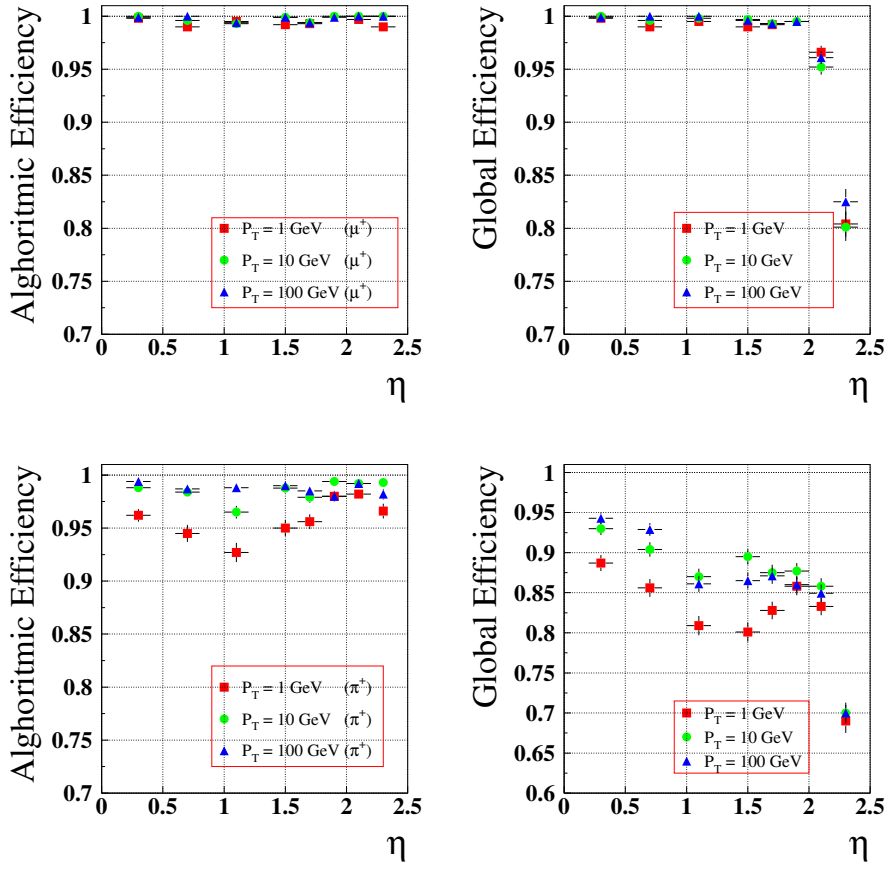

Figure 3.20: Algorithmic (left) and global (right) efficiencies for muon (up) and pion tracks (down).

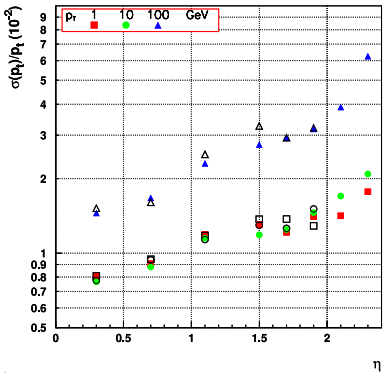

Figure 3.21: Transverse momentum resolution for single muon tracks for several p_T and η values.

$$\epsilon_{fake} = \frac{N(not\ associated\ reconstructed\ tracks)}{N(reconstructed\ tracks)} \tag{3.5}$$

where the denominator is the overall number of reconstructed tracks and the numerator is the number of reconstructed tracks which are not associated to any simulated one. The fake rate is required to be as low as possible in environments with a high track density where the pattern recognition would be less efficient. From Monte Carlo simulations it was observed that it is lower than 10^{-4} for E_T= 50 GeV and lower than 8×10^{-3} for E_T= 200 GeV.
Other important variables for the evaluation of the tracking performance are the resolution in the track parameters. For the i^{th} track parameter ξ_i, the difference between the reconstructed and simulated value is defined as the residual R_i:

$$R_i = \xi_i^{rec} - \xi_i^{sim}. \tag{3.6}$$

The resolution on the ξ_i parameter ($\sigma(\xi_i)$) is the width of a Gaussian fit to the residual distribution. The resolution in p_T is shown in Fig. 3.21: it is around 1-2% in the barrel and has a small dependence on η due to the lower lever arm at high η.
The resolution in the transverse impact parameter (the minimum distance of the track from the (0,0) position in the plane orthogonal to the beam line), which is crucial for b-tagging, is shown in Fig. 3.22. It is dominated by the accuracy of the innermost pixel hit. It also depends on η as the extrapolation to the primary vertex depends on the track momenta which is less precisely measured at high η. The last crucial track parameter is the longitudinal impact parameter (z_{imp}) that is the minimum distance of the track from the

primary vertex in a plane containing the beam line. The resolution on z_{imp}, shown in Fig. 3.22, depends mainly on the innermost pixel hits. However, the dependence on η is more remarkable since it is related to the cluster size on z according to the relationship:

$$\sigma(z_{imp}) \sim \frac{\sqrt{r_1^2 + r_2^2}}{|r_2 - r_1|}\sigma_z \tag{3.7}$$

being r_1 and r_2 the radii of the innermost pixel layers and σ_z the pixel hit resolution in z.

Resolution in the azimutal angle (ϕ) and $\cot\theta$, being θ the polar angle, are shown in the same figure. The former is almost independent on η while the latter degrades significantly in the forward/backward region.

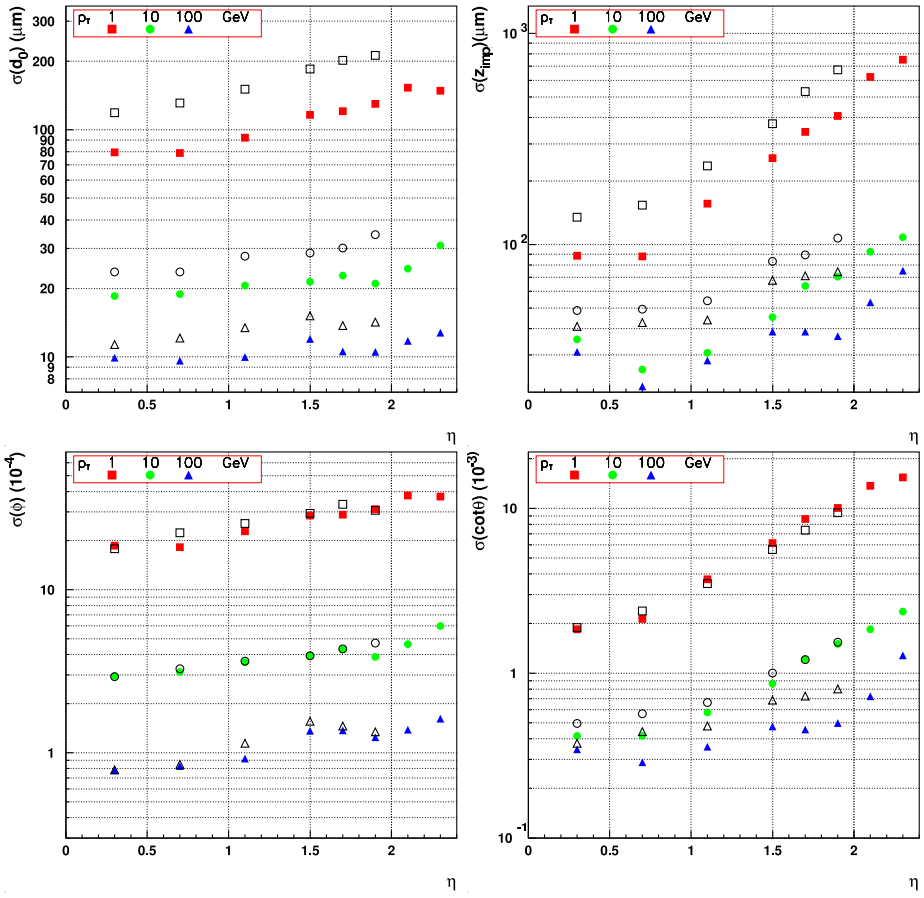

Figure 3.22: Resolutions in transverse impact parameter d_0 (upper left), longitudinal impact parameter z_{imp} (upper left), azimutal angle ϕ (lower left) and $\cot\theta$ (lower right) for muon tracks with p_t ranging between 1 and 100 GeV and $|\eta| < 2.5$. The empty symbols refers to the staged pixel scenario (two layers and 1 disk).

3.4 Measurement of the APV dead time caused by a Highly Ionizing Particle

After the beam test performed in October 2001 at the CERN X5 beam line [93], where six modules of silicon detector prototypes for the CMS tracker were exposed to 120 GeV pions, a few anomalous events were observed, where, following a high energy release inside a silicon sensor, the readout front-end electronics saturates. Typically, strips collecting the energy release give a high, positive, signal, whereas all other channels connected to the same readout chip, the APV[94], are brought well below the pedestal values, outside the dynamic

range. The effect has been explained as due to interaction of a Highly Ionizing Particle (HIP) within the silicon bulk of the CMS Tracker sensors.
Simulation studies [95] have shown that essentially all inelastic nuclear interactions between hadrons and silicon generate highly ionising events (HIP events) and they can result in energy depositions of up to a few hundreds of MeV in 500 μm of silicon (equivalent to $\sim$ 1000 minimum ionising particles). Inelastic

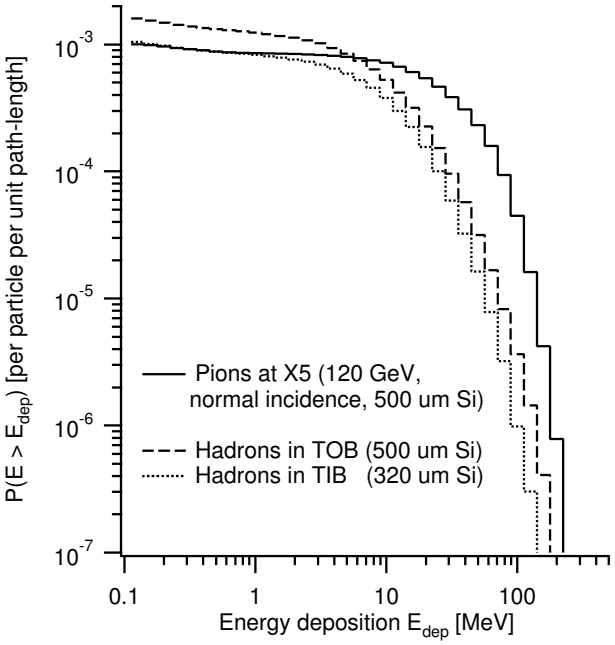

Figure 3.23: Cumulative energy deposition probability spectra, providing the probability of a hadronic interaction in silicon resulting in an energy deposition greater than E_{dep} [MeV] per unit path-lenght in silicon for: 120 GeV pions at normal incidence in 500 μm silicon; hadrons in the CMS Inner Barrel region with their predicted energy spectra and an isotropic angular distribution, per 320 μm path-length in silicon and hadrons in the CMS Outer Barrel region with their predicted energy spectra and an isotropic angular distribution, per 500 μm path-length in silicon.

hadronic collisions in silicon typically produce a short-range nuclear recoil ($<$ 100 μm), resulting in a highly localised energy deposition up to a few tens of MeV, and light fragments, which can travel up to a few mm in silicon and may also be highly ionising. Events with the highest energy depositions always involve several particles. Figure 3.23 shows the probability of a hadronic interaction resulting in an energy deposition greater than E_{dep}, for various sensor thickness and hadronic energy spectra as simulated in an as hoc Monte Carlo program. For more details see Ref. [95, 96].

The simulation has also shown that the magnitude of such energy deposit is often sufficient to saturate the APV chip. The saturation persists in time for few hundred nanoseconds, during which all the 128 channels of the APV are inefficient. The origin of this behaviour was identified in the feedback effect on the branch feeding the APV inverter stage, to which all APV channels are connected. This feed back effect ensures, during normal operation of the APV, the minimisation of any common mode noise. The saturation was reproduced in laboratory tests [96], and its temporal structure has been studied. In particular, it was noticed that, in the time recovery curve, the raise of the APV baseline can bring to an overshoot lasting several hundreds of nanoseconds.
To study the effect of these Highly Ionizing events a dedicated test [97] was performed in April 2002 at the Paul Scherrer Institute (PSI) with 300 MeV/c momentum pion beam. The main goal of this test was to measure the rate of HIP events in a "CMS-like" environment, and this low energy pion beam reproduces the mean interaction rate that the tracker will have to suffer during LHC operation. Final analysis showed an HIP rate per particle in 500 μm in silicon of about 4 $\times 10^{-4}$ [97, 96, 103] for 120 GeV pions which is in good agreement with the plots in Fig. 3.23. In order to further investigate this effect, measurements of the chip recovery time with different APV settings were performed with a dedicated laser setup. High ionisation energy is released in the silicon by the mean of a calibrated laser pulse. With a proper delay, a second laser induces a signal equivalent ot a Minimum Ionising Particle (MIP). The APV response is monitored as a function of the delay time. The induced inefficiency is studied as a function of the deposited energy and of the resistor on the branch feeding the inverter stage. These measurements are complementary to the results obtained on beam tests and in the laboratory in order to assess the effect of HIP events on the CMS Silicon Strip Tracker. The candidate has actively partecipated to this laser studies on the dead time of the chip.
The following sections describe the laboratory test setup and the measurement of the recovery time of the APV after a HIP signal has been induced.

3.4.1 Modules readout

Measurements are made with one of the Tracker Outer Barrel (TOB) modules which had been previously positioned in the pion beam at PSI. It has an APV chip bonded on it, initially equipped with an inverter resistor of 100 Ω. This

resistor was later changed to 50 Ω since it was shown in previous laboratory tests that this change could improve the baseline recovery. The module was equipped with the same read-out electronic used in the previous X5 and PSI beam tests [97]. A detailed explanation of the electronic components of the front-end readout can be found in [98]. A Trigger Sequencer Card [99] was used as external trigger in time with the pulser triggering the MIP laser.
Acquisition and control were performed through the *standalone* [100] acquisition program. This program is able to run the different calibration tasks needed for Silicon detector commissionning, i.e. pedestal, timing alignment, pulse shape on calibration pulse or signal. It has also been used to perform a full cluster analysis on data with the same algorythms that were used for the PSI beam test.

3.4.2 Laser setup and HIP calibration

The setup consists of two 1060 nm semi conductor lasers triggered by a narrow pulse (<3ns) in order to get a light pulse well calibrated in time, during the laser relaxation. The TOB module, composed by two Si wafers bonded together, was positionned over a second silicon wafer with part of the strips connected to the same APV chip. With the help of a spheric lense at the end of the fiber, the light was focused on one strip only for both lasers, outside the strip metallization. The intensity of one laser was then increased in order to generate a energy deposit comparable with a HIP signal. The second laser was still shooting a MIP equivalent pulse and the data acquisition was aligned in time with this later trigger in order to collect the maximum of the charge of the MIP pulse. This pulse was finally delayed with respect to the HIP one and the MIP signal was studied versus the delay time. The HIP pulse intensity is controlled by two parameters: the laser bias voltage and the time width of the light pulse. We fixed the time width and made a scan in voltage bias. The linear dependence of the HIP intensity from the voltage is shown in Fig. 3.24. Netherltheless, during the calibration of the laser it was discovered that the module was not perfectly shielded from light, which implied a systematic uncertainty of about 10% in the evaluation of the HIP intensity.
The energy deposited by a HIP pulse was evaluated using the bias current of the TOB module. The bias current, also known as the dark current, is indeed increased by the charge injected by the HIP. If the pulse rate, that

generates the HIP, is high enough it is possible to measure the increase of the bias current. To measure this current at different HIP pulse rates we used a nano-amperemeter [102]. We measured the difference in current with and without the HIP (ΔI) at different injection rates. At a fixed rate, assuming that the mean charge released by a MIP is known ($\sim$ 42,000 electrons for the 500 μm silicon devices), the number of MIPs injected is directly deduced from the current value

$$N_{MIP} = \frac{\Delta I}{rate \times MIP_{charge}}.$$

The stability of the charge collection and thus the quality of the measurement is verified along a large range of rate as shown in Fig. 3.24. To convert the number of MIP into a value of released energy (in MeV) the estraction energy of the silicon has been used. To create one electron-hole pair an energy release of about 3.6 eV is needed, so one MIP corrisponds to about 140 KeV.

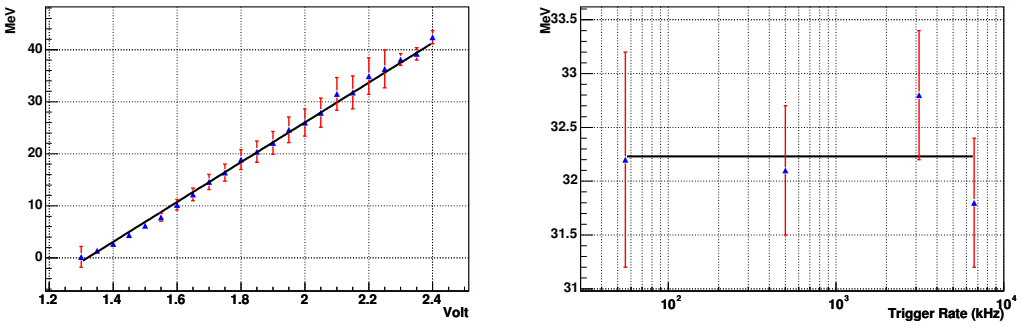

Figure 3.24: Laser bias voltage calibration curve for an integration time of 5.5 ns (left) and Measured HIP intensity versus the pulse rate (right).

3.4.3 APV recovery measurement

The recovery of the APV performances after a HIP event is studied in this section in terms of baseline and signal recovery, while the following section presents the improvement of the recovery when the inverter resistor is set to 50 Ω, as suggested by previous laboratory measurements [96]. All the following plots and data are referred to the APV chip operating in deconvolution mode, that will be the default mode during the CMS data taking.

Baseline and signal recovery

The baseline shift is evaluated on an event-by-event basis with the common mode noise calculation. In the present case, the calculation of the common mode is slightly different with respect to the one usually adopted. The calculation is restricted to blocks of 32 strips in order to obtain a signal as clean as possible without fake clusters created by baseline distortion due to the HIP. In the following plots the common mode noise shown is estimated from a block of 32 strips that do not contain the pulse of the HIP and of the MIP fired strips. Plots in Fig. 3.25 (black dots) show the evolution of the mean common mode noise of the APV as a function of the time after a HIP shot, using the data collected in deconvolution mode, for a TOB module equipped with an inverter resistor of 100 Ω. For low energy HIPs, the baseline starts to recover almost immediatly. For higher energy deposits ($>$ 21 MeV), the chip remains saturated for more than 200 ns. From the above results one may expect to recover full efficiency as soon as the baseline is brought back in the APV dynamic range, but this is not the case. To study the signal recovery without the cut on the cluster reconstruction, we took advantage of the fixed position of the laser pulse and we followed the time evolution of the signal (raw - pedestal - common mode noise) of the central strip in the cluster induced by the laser pulse. We normalized the signal over noise ratio of the strip to a reference value measured with strips not hit by the laser. Figure 3.25 (red triangles) shows the signal recovery in strips fired by the MIP. It is clear that for energy deposit below 20 MeV the signal recovery is nearly immedaite, as soon as the baseline enters again the dynamic range. For bigger energy deposit the signal recovery is delayed with respect to the baseline recovery.
To better quantify the effect of the HIP the *dead time* of the chip has been measured. We can define dead time as the time interval, after the HIP injection, during which no signal is detected. However, to have a recontructed cluster the signal must be at least 3 times bigger than the noise, so the inefficiency time may be longer than the dead time itself. Considering an average signal over noise of 12 for TOB irradiated modules, we can say that the chip is again fully efficient as soon as the signal over noise, in Fig. 3.25, reaches the value of 0.25. The maximum dead time, measured in deconvolution mode for an inverter resistor of 100 Ω, has been of 700 ns, reaching full efficiency after 800 ns, for an energy deposit of about 60 MeV. In Tab. 3.4 dead time and full

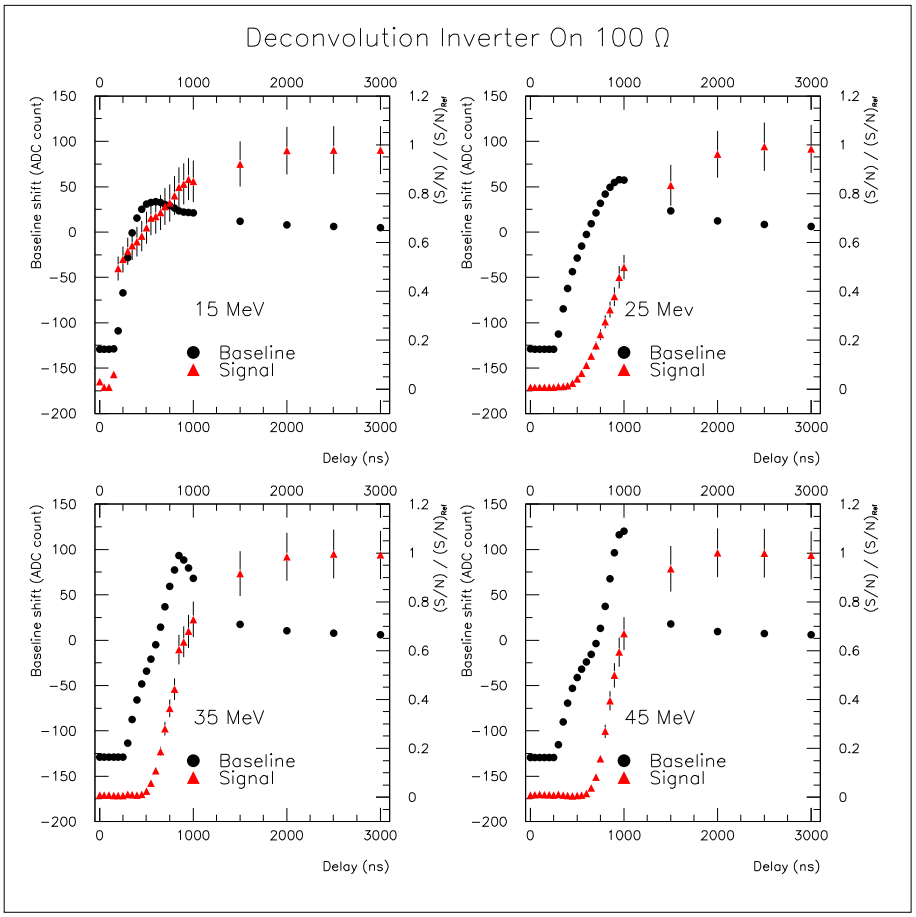

Figure 3.25: Time evolution of the baseline (black dots) and signal over noise (red triangles) recovery, expressed in terms of ADC counts, of APV's operating in deconvolution mode for a TOB module equipped with R inv=100 Ω. Different hip magnitudes are considered.

efficiency recovery time are shown for different energy deposit.

3.4.4 Comparison between 50 Ω and 100 Ω inverter resistor

In this section the behaviour of an APV with inverter resistor of 50 Ω is presented.

As shown in previous measurements [96], the dead time due to HIP events would be reduced with a smaller inverter resistor. We repeated the measurements on the same APV chip but equipped with an inverter resistors of 50 Ω instead of 100 Ω. Results are shown in Fig. 3.26 where the time evolution of the baseline (black dots) and signal over noise recovery (red triangles) are

HIP energy (Mev)	Dead time (ns)	Full Efficiency (ns)
20	100	200
34	500	800
48	600	700
62	700	800

Table 3.4: Dead time and full efficiency recovery time, as explained in the text for different HIP magnitudes. The measurements have been performed on an APV operating in deconvolution mode with inverter resistor of 100 Ω.

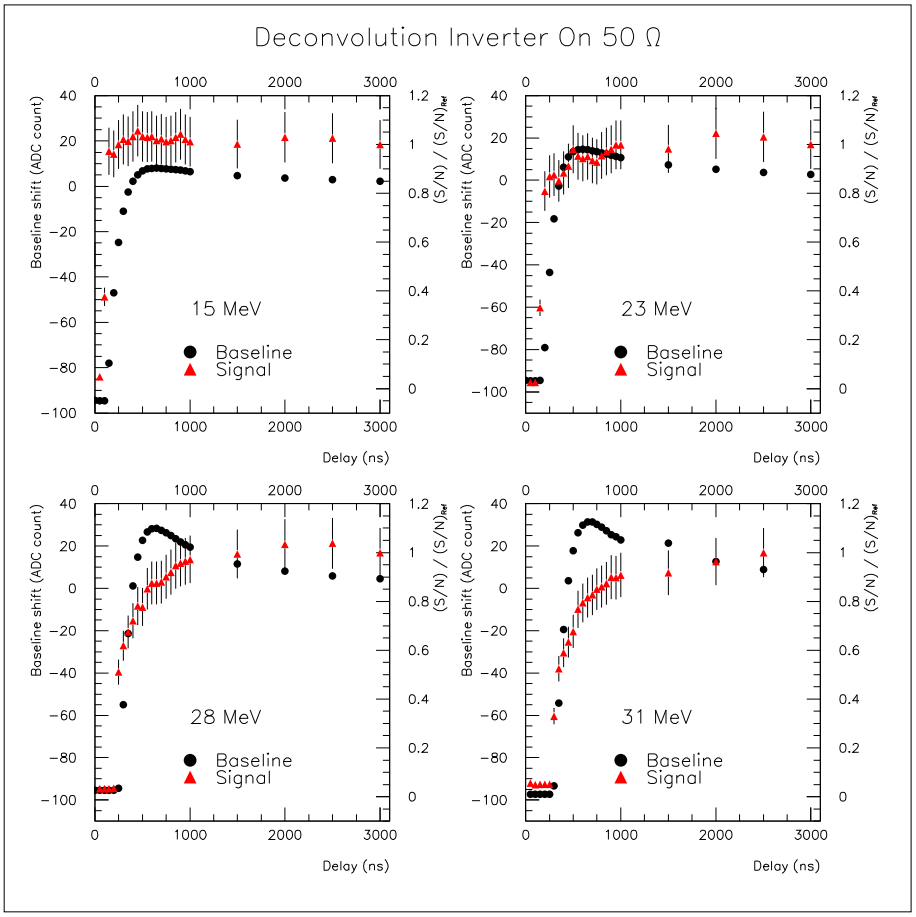

Figure 3.26: Time evolution of the baseline (black dots) and signal over noise (red triangles) recovery, expressed in terms of ADC counts, of APV's operating in deconvolution mode for a TOB module equipped with R inv=50 Ω. Different hip magnitudes are considered.

shown for different HIP magnitudes. The dead time is reduced by about a factor two with respect to the 100 Ω case, and the signal recovery is following

HIP energy (Mev)	Dead time (ns)	Full Efficiency (ns)
20	100	100
32	150	150
39	250	250
44	300	300

Table 3.5: Dead time and full efficiency recovery time, as explained in the text for different HIP magnitudes. The measurement have been performed on an APV operating in deconvolution mode with inverter resistor of 50 Ω.

the baseline recovery so that the total inefficiency time is reduced. Table 3.5 shows final results on dead time and full efficiency recovery. With 50 Ω inverter resistor the total dead time is about 300 ns for an energy deposit of 44 GeV.

3.4.5 Effect of dead time on the track reconstruction

The effect of the dead time of the APV chip, due to the HIP interaction, on the track reconstruction and b-tagging performance of the CMS tracker has been studied in detail in [104]. A reasonable dead time of 150 ns and a really pessimistic one of 750 ns have been simulated in the CMS reconstruction software. A dead time of 150 ns is expected for an energy deposit greater than 10 MeV. The probability that a hadronic collision in a TOB module results in an energy deposition greater than 10 MeV is about 5×10^{-4}.
The total effect on the single muon track reconstruction is an efficiency loss of about 2% with a dead time of 750 ns, and no effect at all for a dead time of 150 nsec. For what concerns b-tagging efficiency this numbers changes a little due to the high track multiplicity in the jet cone. For a dead time of 150 ns the b-tagging efficiency decreases by about 1% while in the worst case (750 ns) the efficiency loss is about 8%. This results are shown in Tab. 3.6 as a function of the dead time for two jet energies: 100 GeV and 200 GeV. Only a huge energy deposit would lead to a dead time of 750 ns, and it would really be a problem only if the present knowledge of hadronic interaction in the silicon modules are underestimated by a factor 3 or 4.
To cope even with this really unlike situation, the reconstruction software and the front-end electronics software are being modified. Within few months it will be possible, in the track reconstruction, to skip a silicon layer if a dead chip is found [105]. This procedure will guarantee the full recovery of the

HIP dead time (ns)	b-tagging eff. (100 GeV)	b-tagging eff. (200 GeV)
0 (no HIP)	0.81	0.79
150	0.80	0.78
750	0.78	0.72

Table 3.6: Effect of the dead time for b-tagging efficiency for jets with energies of 100 GeV and 200 GeV.

reconstruction and b-tagging efficiency.

Chapter 4

Trigger

The CMS experiment will operate with a bunch-crossing frequency of 40 MHz and with a luminosity which will range from about $10^{33} cm^{-2} s^{-1}$ to the design luminosity of $10^{34} cm^{-2} s^{-1}$, at which we expect about 20 inelastic interactions per bunch crossing. The CMS trigger system has the formidable task of reducing this input data rate to $\mathcal{O}(10^2)$ Hz which will be written to permanent storage.
The CMS data acquisition system (DAQ) is designed to accept an input rate of 100 kHz events having a size of 1 MB. The trigger system uses a custom Level-1 processor to select these kHz events from the input 40 MHz bunch-crossing rate. During the $3\mu s$ latency of the Level-1 trigger the event data are stored in front-end pipelines. The remaining selection process is made in a farm of standard commercial processors.
In this chapter the trigger is presented with particular emphasis on the τ trigger at which development the candidate has actively partecipated.

4.1 The Level-1 trigger

The Level-1 trigger System [106] is organized into three major subsystems: the Level-1 calorimeter trigger, the Level-1 muon trigger, and the Level-1 global trigger.
The muon trigger is further organized into subsystems representing the 3 different muon detector systems, the Drift Tube (DT) trigger in the barrel, the Cathode Strip Chamber (CSC) trigger in the endcap and the Resistive Plate

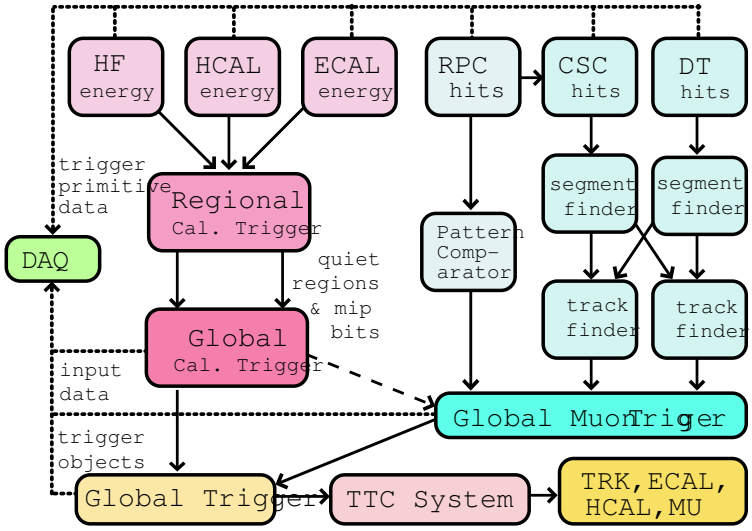

Figure 4.1: Overview of the Level-1 trigger system.

Chamber (RPC) trigger covering both barrel and endcap. The Level-1 muon trigger also has a global muon trigger that combines the trigger information from the DT, CSC and RPC trigger systems and sends it to the Level-1 global trigger.

A diagram of the Level-1 trigger system is shown in Fig. 4.1. The input data to the Level-1 trigger system as well as the input data to the global muon trigger, global calorimeter trigger and the global trigger are transmitted to the DAQ for storage along with the event read-out data. In addition, all trigger objects found, whether they were responsible for the Level-1 trigger or not, are also recorded. The decision whether to trigger on a specific crossing or to reject it is transmitted via the trigger Timing and Control system to all the detector subsystem front-end and read-out systems.

4.1.1 Calorimeter trigger

In order to build the Calorimetric trigger, towers of cells covering a solid angle of $(0.35\eta \times 0.35\phi)$ are grouped together in the upper level read-out trigger Primitive Generator (TPG) circuits.

For the ECAL, these energies are accompanied by a bit indicating the transverse extent of the electromagnetic energy deposit. For the HCAL, the energies are accompanied by a bit indicating the presence of minimum ionizing energy.

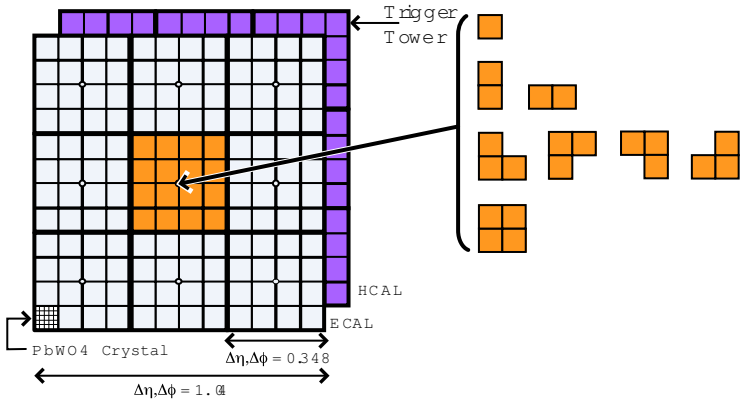

Figure 4.2: Jet trigger algorithms.

The TPG information is transmitted over high speed copper links to the Regional Calorimeter trigger (RCT), which finds candidate electrons, photons, τ leptons, and jets. The RCT separately finds both isolated and non-isolated electron/photon candidates, then it transmits the candidates together with the sums of the transverse energies to the Global Calorimeter trigger (GCT). The GCT sorts the candidate electrons, photons, τ leptons, and jets and forwards the top 4 of each type to the global trigger. The GCT also calculates the total transverse energy and the total missing energy vector. It transmits this information to the global trigger as well. The Regional Calorimeter trigger also transmits an (η,ϕ) grid of quiet regions to the global muon trigger for muon isolation cuts.

Jet triggers

The jet trigger uses the transverse energy sums (electromagnetic + hadronic) computed in calorimeter regions 4×4 trigger towers wide, except in the HF region where the trigger tower is directly used. The input tower E_T is coded in an 8 bit linear scale with programmable resolution. Values exceeding the dynamic range are set to the maximum. The subsequent summation tree extends to a 10 bit linear scale with overflow detection.
The jet trigger uses a 3×3 calorimeter region sliding window technique which spans the complete (η,ϕ) coverage of the CMS calorimeters (Fig. 4.2). The transverse energy measured in the central region is required to be higher than the energy seen by the eight neighbour regions. In addition, the central region

E_T is required to be greater than a fixed value, e.g. 5 GeV, to suppress spurious soft events.
The jets are characterized by the transverse energy E_T collected in 3×3 calorimeter tower regions. The summation spans over 12×12 trigger towers in the barrel and endcap or over 3×3 larger towers in the HF. The ϕ size of the jet window is the same everywhere. The η binning gets somewhat larger at high η due to the size of the calorimeter and trigger tower segmentation. The jets are labelled by (η,ϕ) position of the central calorimeter regions.
In addition, counters of the number of jets above programmable thresholds in various η regions are provided to give the possibility of triggering on events with a large number of low energy jets. Jets in the forward and backward HF calorimeters are sorted and counted separately. This separation is a safety measure to prevent high η regions with more background from masking the central jets. As the same reconstruction algorithm and resolutions are used for the entire $\eta - \phi$ plane, the central and forward jets are reconstructed in the same way and, although they are sorted and tracked separately by the trigger system, they can be used by the global trigger without any difference.
Single, double, triple and quadruple jet triggers are possible. The single jet trigger is defined by the transverse energy threshold, the (η,ϕ) coordinates of the calorimeter regions hit and eventually by a prescaling factor. Prescaling will be used for low energy jet triggers, necessary for efficiency measurements. The multi jet triggers are defined by the number of jets and their transverse energy thresholds, by a minimum separation in (η,ϕ), as well as by a prescaling factor. The global trigger accepts the definition, in parallel, of different multi jet trigger conditions. The four highest energy central and forward jets in the calorimeter are selected. Jets occurring in a calorimeter region where an electron is identified are not considered. The selection of the four highest energy central and forward jets provides enough flexibility for the definition of combined triggers, i.e. selections that take into account the presence of different physics objects in the event (jets, electrons and muons).
Another quantity of interest, which is also useful in making comparisons between different algorithms and different detectors, is the rate as a function of the jet E_T at the generator-level. Fig. 4.3 shows the rate for the 95% efficiency thresholds, i.e. the threshold for which a jet with that energy at generator-level has the 95% probability to pass the selection, for low and high luminosity.

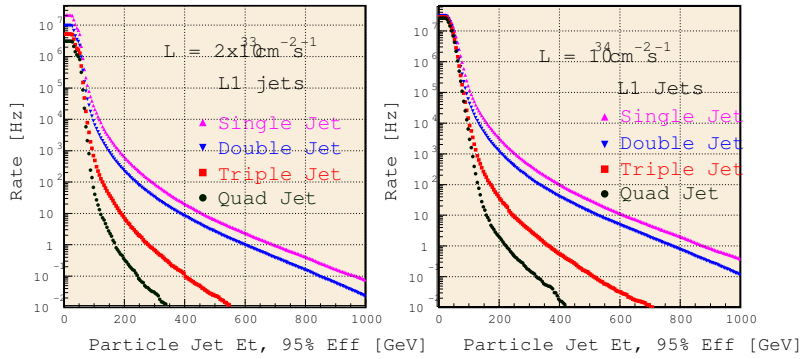

Figure 4.3: Level-1 jet trigger rates, for the 95% efficiency thresholds, for low and high luminosity.

$\hat{p_T}$, GeV	cross-section, mb	number of events
50-80	2.25 $\times 10^{-2}$	148000
80-120	3.22 $\times 10^{-3}$	148000
120-170	5.47 $\times 10^{-4}$	150000

Table 4.1: QCD 2-jet event samples.

τ trigger

First (Level-1) [108] (and High Levels [108, 109]) τ triggers are designed to efficiently select physics channels with a lepton and a τ-jet or with two τ-jets in the final states. The algorithms are studied at low and high luminosities. The evaluation of the algorithm performance consists of measuring the efficiency for the selection of benchmark signal samples and the corresponding efficiency for the QCD background. As benchmark signal the $A^0/H^0 \rightarrow \tau\tau$ and $H^+ \rightarrow \tau\nu$ channel has been chosen. An important element of the analysis is the measurement of the CPU time required for the selection.
The QCD two-jet events have been generated with PYTHIA in several different $\hat{p_T}$ bins and then processed through the full detector simulation (CMSIM 125, ORCA 6.2.0). These samples are presented in Table 4.1. It has been found that these bins ($50 < \hat{p_T} < 170$ GeV/c) give the biggest contribution to the Level-1 τ trigger rate (85-95%). The weights corresponding to the fraction of the Level-1 output rate from the individual bins have been taken into account when the High Level trigger rejection factor is calculated. Signal events have been selected at PYTHIA generation level with loose off-line analysis selection

cuts on leptons and τ-jets [110] in order to maximize the statistics after the Level-1 trigger:

- for $A^0/H^0 \rightarrow 2\tau \rightarrow 2\tau$-jets : $p_T^{\tau-jet} > 45$ GeV/c, $|\eta^{\tau-jet}| < 2.4$
- for $H^+ \rightarrow \tau\nu \rightarrow \tau$-jet : $p_T^{\tau-jet} > 80$ GeV/c, $|\eta^{\tau-jet}| < 2.4$

High luminosity running conditions are reproduced by superimposing on average 17.3 minimum bias events on top of every trigger event. Out of time bunches (5 before the trigger bunch and 3 after the trigger bunch) have also been simulated.
A dedicated Level-1 Tau trigger naturally complements the Level-1 Jet trigger design [112] and provides efficient triggering capability for a low mass (200-300 GeV) Higgs decaying into two τ leptons with one or both τ 's decaying hadronically.
The Level-1 Tau algorithm consists of the following steps:

- form generic jets as 12 $\times$ 12 groups of trigger towers, sliding in 4 $\times$ 4 steps, the value of E_T in the central 4 $\times$ 4 region being greater than the E_T's of its 4 $\times$ 4 neighbours (see Fig. 4.2);
- redefine a generic jet as a τ-jet if none of its nine 4 $\times$ 4 regions have a τ-veto bit on. τ-veto bits are formed by requiring that there be no more than 2 active ECAL or HCAL towers in the 4 $\times$ 4 region. In the present simulation, an ECAL (HCAL) tower is considered active if its E_T is greater than a programmable threshold of 2 (4) GeV.
- the 4 highest E_T Jets and 4 highest E_T τ-jets are then sent to the global trigger for consideration as trigger objects.

The efficiency of the Level-1 Tau algorithm for τ-jets is rather high, between 0.8 and 0.7, for low E_T τ-jets (50$< E_T <$ 100 GeV), such as those found in the decays of a low mass Higgs boson and is uniform over the η acceptance. The efficiency decreases to $\sim$0.5 for $E_T^{\tau-jet} \sim 250$ GeV. This is because the number of active towers increases as the E_T of the τ-jet increases. However, this drop in efficiency at high E_T can be recovered by using generic jets instead of τ-jets in the $H \rightarrow \tau\tau$ trigger when the jets are above an appropriate threshold.
The efficiency curve of a τ-jet (or Jet) trigger is affected in particular by the calibration and by the resolution of the combined calorimetric system. In the

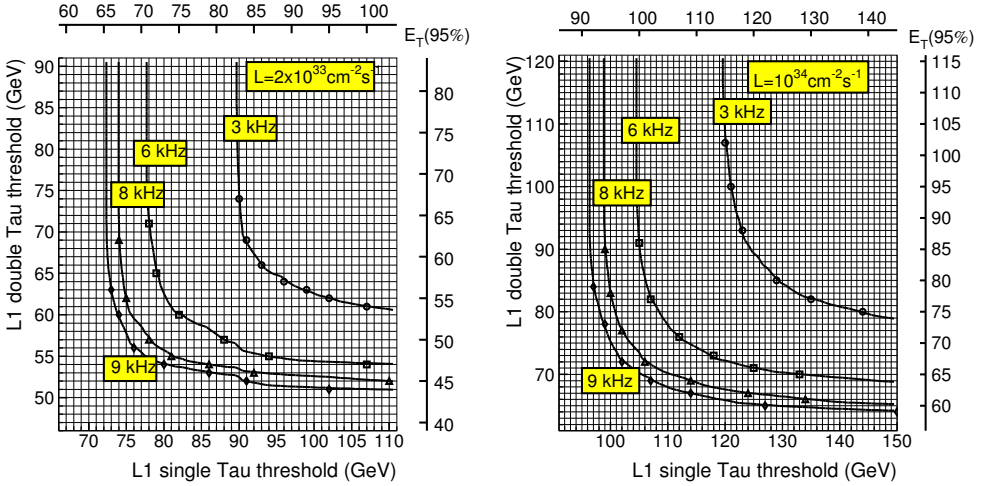

Figure 4.4: Isorate curves as a function of single and double Tau threshold. Left: low luminosity. Right: high luminsity.

present simulations the hadron calorimeter has been calibrated with single pions of E_T=50 GeV [112], and the electromagnetic calorimeter reconstructs the energies of electrons and photons. Level-1 trigger includes provision for energy scale corrections, the energy values being averaged over pseudorapidity $|\eta| < 2.4$.

The isorate curves as a function of single and double Tau threshold are shown in Figure 4.4 for both luminosity scenarios. For what concerns the next sessions of this chapter, a final rate of 3 (8) kHz for the low (high) luminosity has been considered.

The dependence of the 95% efficiency point of the Level-1 single Tau trigger versus trigger threshold is shown in Figure 4.5. For τ-jets with transverse energies between 50-110 GeV, the shift between trigger threshold and 95% efficiency point is less than 10 GeV.

According to the updated Jet trigger design, the calorimeter trigger will provide to the global trigger the 4 highest E_T Tau jets, the 4 highest Et Central Jets within $|\eta| < 3$ and the 4 highest Et Forward Jets in the region $3 < |\eta| < 5$ to be used in the higher trigger level decisions. In Figure 4.6 we present rates from the single-double Central Jet and the single-double Tau Jet trigger as a function of the trigger threshold for both low and high luminosity conditions. The Tau trigger is a vital element for the new design of the trigger for low mass Higgs bosons ($\sim$ 200 GeV). The transverse energies of τ-jets from low mass

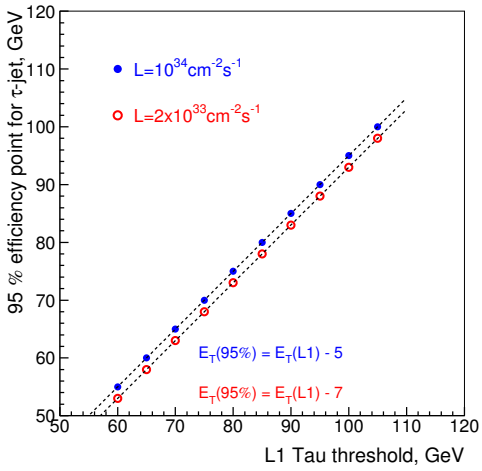

Figure 4.5: 95% efficiency point of the Level-1 single Tau trigger versus trigger threshold.

Higgs bosons are mostly concentrated in the interval 50-110 GeV. The limit on the rate from τ and jet triggers must be set at $\sim$ 3 kHz at low luminosity. From these plots, one can see that the Tau trigger allows to trigger in this interval with an acceptable rate. The efficiency for the signal events and the

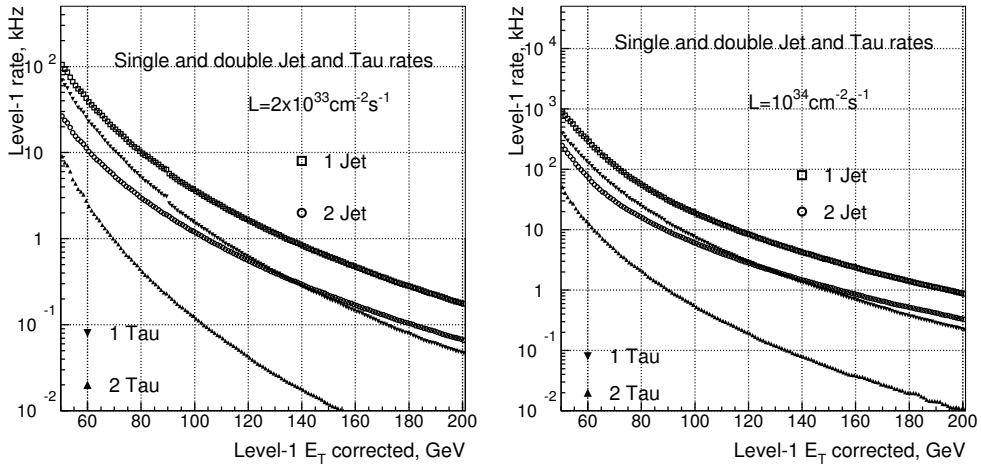

Figure 4.6: Rates of a Single-Double Central Jet trigger and Single-Double Tau Jet trigger as a function of the trigger threshold. Left: low luminosity. Right: high luminosity.

rates for the Jet triggers are presented in Table 4.2. Efficiecy are evaluated for $A^0/H^0 \rightarrow 2\tau \rightarrow 2\tau$-jets (double Tau Trigger) and $H^+ \rightarrow \tau\nu \rightarrow \tau$-jets (single Tau Trigger) events. The thresholds quoted in parenthesis corrispond to the

true τ-jet energy at which the trigger is 95% efficiency.
Signal purity can be improved by considering the single and double Central Jet triggers with appropriate thresholds.

Luminosity	rate, kHz	1 Tau threshold (95%), GeV	2 Tau threshold (95%), GeV	$\epsilon(H \to 2\tau)$ $M_H = 200GeV$	$\epsilon(H^+ \to \tau\nu)$ $M_H = 200GeV$
Low	3	93 (86)	66 (59)	0.78	0.81
High	8	106 (101)	72 (67)	0.62	0.76

Table 4.2: Effciency for Level-1 Tau Trigger for τ-jets.

Energy triggers

The E_T triggers use the transverse energy sums (electromagnetic + hadronic) computed in calorimeter regions covering 4×4 trigger towers in the barrel and in the endcap. E_x and E_y are computed from E_T using the coordinates of the centre of the calorimeter region.
The missing E_T is computed from the sums of the calorimeter regions E_x and E_y. The sum extends up to the end of forward hadronic calorimeter, i.e., $|\eta|$=5. The missing E_T triggers are defined by a threshold value and by a prescaling factor. The global trigger can use this selection alone or combined with other trigger strategy.
The total E_T is given by the sum of the E_T measured in all calorimeter regions. The sum extends up to the end of forward calorimeter, i.e., $|\eta|$=5. The total E_T triggers are defined by a threshold value and by a prescaling factor. The total energy trigger is implemented with a number of thresholds which are used both for trigger studies and for input to the luminosity monitor. Some of these thresholds are used in combination with other triggers. Other thresholds are used with a prescale and one threshold is used for a standalone trigger. The lower threshold E_T trigger can be used to check the calorimeter status and the trigger efficiencies.
The H_T trigger is defined as the scalar sum of the E_T of jets above a programmable threshold with a typical value of $E_T > 10$ GeV. This trigger is less sensitive than the total E_T trigger to noise and pileup effects. Although the total E_T is a necessary technical trigger, it has a limited use from the physics point of view. The H_T trigger can capture high jet multiplicity events such

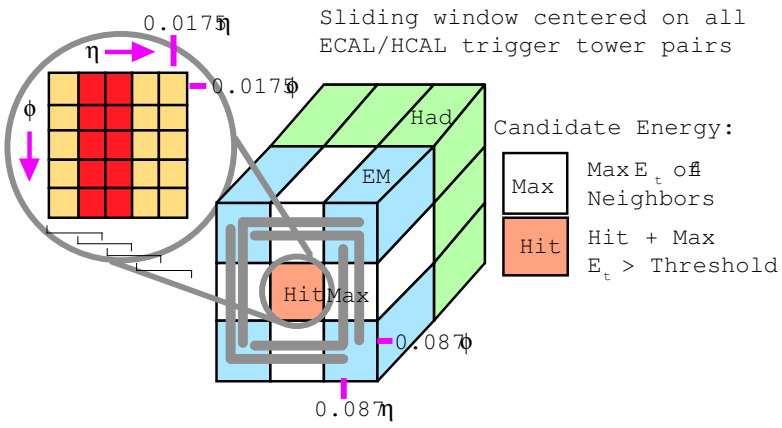

Figure 4.7: Electron/photon trigger algorithm.

as those from fully hadronic top decay and hadronic decays of squarks and gluinos. Although these events have an energy of several hundred GeV, they may actually fail the jet trigger because individual jet E_Ts may be individually softer than any sustainable threshold. In addition, the H_T trigger can use individually calibrated jet energies unlike the total E_T trigger which cannot be easily calibrated.

Electron/Photon triggers

Electrons and photons form a narrower shower than hadrons in the calorimeter and the energy is usually released in an isolated region. Almost every algorithm used to identify electron and/or photons is based on these characteristics. Clearly at Level-1, considering only calorimetric informations, there is no possibility to distinguish between electrons and photons candidates.
An overview of the electron/photon isolation algorithm, used in CMS, is shown in Fig. 4.7. This algorithm involves only the eight nearest neighbours around the central trigger tower and is applied over the entire (η,ϕ) plane. The transverse energy of the electron/photon candidate is determined by summing the E_T collected in the hit tower with the maximum E_T measured by one of the four broad side neighbours. This summed transverse energy provides a sharper efficiency turn-on when plotted against the true E_T of the particles. The non-isolated candidate has to pass two shower profile selection. One veto is based

on the finegrain ECAL crystal energy profile. The other is based on HCAL to ECAL energy comparison, e.g. the energy released in the Hadronic calorimeter should not be more than the 5% of the energy released in the Electromagnetic calorimeter.

The isolated candidate requires passing two additional conditions, the first requiring the signal to be larger than those of all eight nearest neighbours, and the second requiring at least one quiet corner, i.e. all the five towers, of at least one corner, must be below a programmable threshold (1.5 GeV). Each candidate is characterized by the (η,ϕ) indexes of the calorimeter region where the central hit tower is located. In each calorimeter region (4×4 trigger towers) the highest E_T non-isolated and isolated electron/photon candidates are separately found. The 16 candidates of both streams found in a regional trigger crate (corresponding to 16 calorimeter regions covering $\Delta\eta \times \Delta\phi$=3.0×0.7) are further sorted by transverse energy. The four highest-E_T candidates of both categories in each crate are transferred to the Global Calorimeter trigger where the top four candidates are retained to be processed by the CMS global trigger.

The nominal electron/photon algorithm allows both non-isolated and isolated streams. The non-isolated stream uses only the hit tower information except for adding in any leakage energy from the maximum neighbouring tower. This stream will be used at low luminosity to provide the B-electron trigger. The isolation and shower shape trigger cuts are programmable and can be adjusted to the running conditions. For example, at high luminosity the isolation cuts could be relaxed to take into account higher pile-up energies. The specification of the electron/photon triggers also includes the definition of the $\eta - \phi$ region where it is applicable. In particular, it is possible to define different trigger conditions (energy thresholds, isolation cuts) in different rapidity regions. The efficiency of the electron/photon algorithm, as a function of the electron transverse momentum, for different thresholds applied at Level-1, is shown in Fig. 4.8. Also shown in Fig 4.8 is the efficiency, as function of pseudorapidity for electrons with p_T =35 GeV/c.

To connect the Level-1 threshold to an effective requirement on the electron transverse momentum the electron p_T at which the Level-1 trigger is 95% efficient is determined as function of the Level-1 threshold. This is shown in Fig. 4.9. From this result, the rate for electron/photon triggers as a function of the cut on the effective E_T, i.e. the threshold at which the trigger is 95%

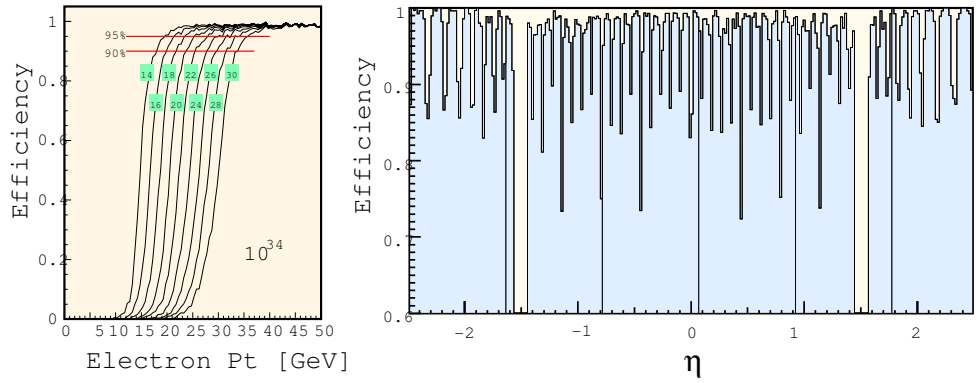

Figure 4.8: The efficiency of the Level-1 trigger for single electrons as a function of the electron p_T. On the right, the efficiency as function of η, for electrons with p_T =35 GeV/c.

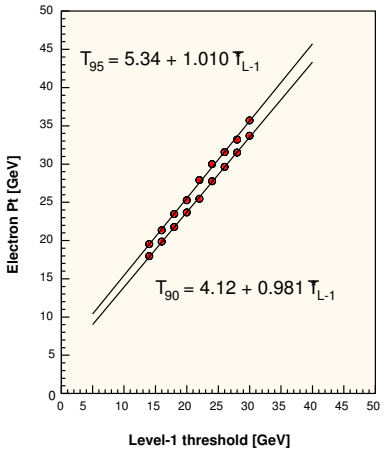

Figure 4.9: The electron E_T at which the Level-1 trigger is 95% efficient as a function of the Level-1 threshold.

efficient, can be computed. Fig. 4.10 shows the rates for single electrons as a function of the E_T of the electron (95% point). Double, triple and quadruple electron/photon triggers can be defined. The requirements on the objects of a multi electron/photon trigger, namely the energy threshold, the cluster shape and isolation cuts and the (η,ϕ) region, are set individually. Requirements on the (η,ϕ) separation between objects can also be defined. The rate for two-electron/photon triggers is shown in Fig. 4.11.

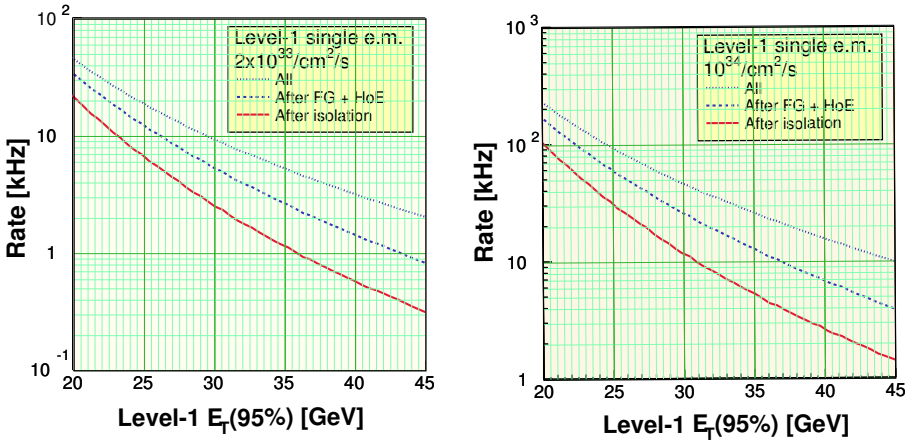

Figure 4.10: The rate of the single electron/photon Level-1 trigger at low (left) and high (right) luminosity.

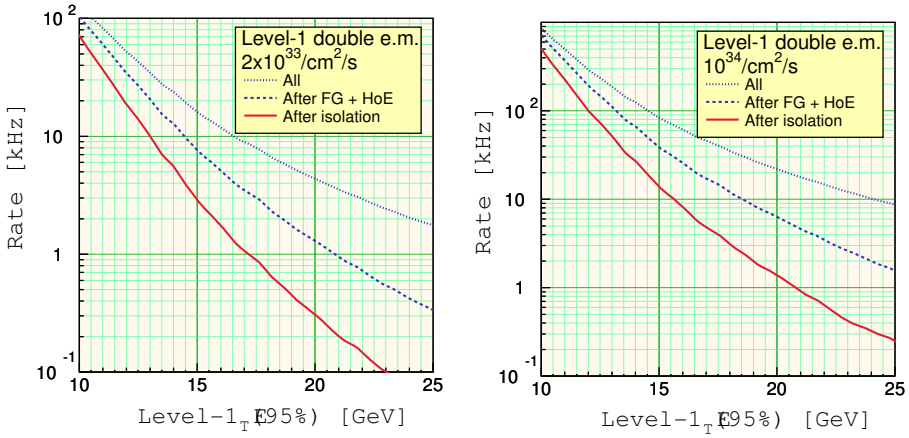

Figure 4.11: The rate of the double electron/photon Level-1 trigger at low (left) and high (right) luminosity.

4.1.2 Muon trigger

Muons are relatively easy to identify. They don't release much energy in the calorimeter and their passage can be traced both in the tracker and in the muon stations. The CMS muon identification sistem relies on the track reconstruction by the muon station, and by isolation criteria based on calorimetry and tracking.
The Level-1 muon trigger is composed by three subsystem: Resistive Plate Chambers (RPC), Cathode Strip Chambers (CSC) in the end-cap and Drift Tube (DT) in the barrel. The trigger selection is based on the measurement of the p_T of the reconstructed tracks, the quality of the reconstruction, the isolation of the energy released in the calorimeter and the track reconstructed with the Tracker.
The trigger uses two subsystem together, either the RPC and the CSC or the RPC and the DT. For example the RPC logic provides data to the CSC trigger system to improve resolution of ambiguities caused by 2 muons in the same CSC.
The Global Muon trigger sorts the RPC, DT and CSC muon tracks, converts these tracks into the same η, ϕ and p_T scale, and validates the muon sign. It then attempts to correlate the CSC and DT tracks with RPC tracks. It also correlates the muon tracks with an $\eta - \phi$ grid of quiet calorimeter towers to determine if these muons are isolated. The final ensemble of muons are sorted on the basis of their initial quality, correlation and p_T and then the 4 top muons are sent to the Global trigger.

Drift Tube trigger

The drift chambers deliver data for track reconstruction and for triggering on different data paths. The local trigger is based on two Super Layers in the ϕ view of the muon station. The trigger frontend, called the Bunch and Track Identifier (BTI), is used in the ϕ view and the θ view to perform a rough muon track fit in one station measuring the position and direction of trigger candidate tracks with at least three hits in different planes of a Super Layer. The algorithm fits a straight line within programmable angular acceptance regions. The BTI performs the bunch crossing assignment of every muon track

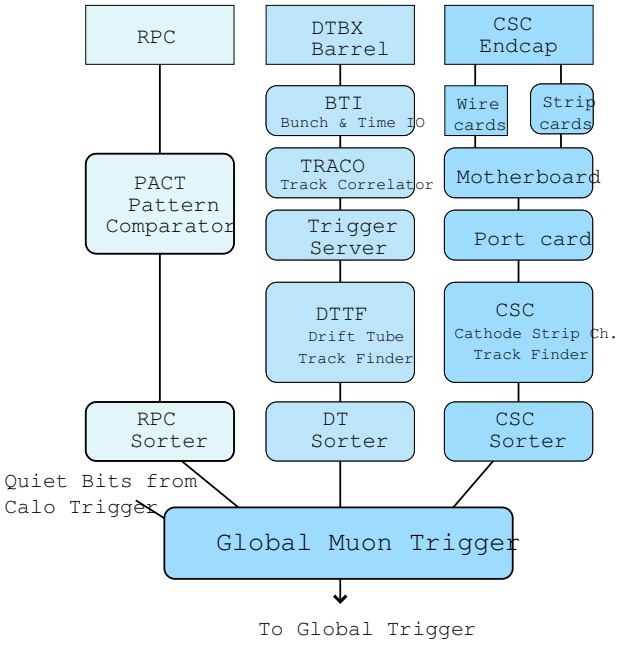

Figure 4.12: Block diagram of the Level-1 muon trigger.

candidate [107]. Since the algorithm must foresee alignment tolerances and has to accept also alignments of only three hits, it can generate false triggers. Hence in the bending plane a system composed by a Track Correlator and a chamber trigger Server is used to filter the information of the two ϕ Super Layers of a chamber in order to lower the trigger noise. Track segments found in each station are then transmitted to a regional trigger system called Drift Tube Track Finder. The task of the Track Finder is to connect track segments delivered by the stations into a full track and assign a transverse momentum value to the finally resolved muon track. The system is divided in sectors, each of them covering 30 in the ϕ angle. Each Sector Processor is logically divided in three functional units: the Extrapolator Unit (EU), the Track Assemblerand and the Assignment Units, as shown in Fig. 4.13.

The Extrapolator Unit attempts to match track segments pairs of distinct stations. Using the spatial coordinate ϕ and the bending angle of a seed segment, an extrapolated hit coordinate is calculated to the next layer. The two best extrapolations per each seed are forwarded to the Track Assembler. The Track Assembler attempts to find at most two tracks in a detector sector with the highest rank, i.e. exhibiting the highest number of matching track

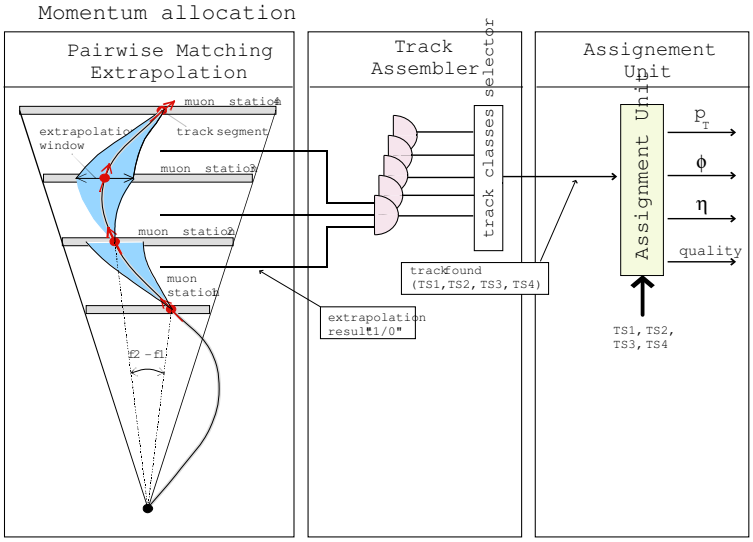

Figure 4.13: Principle of the Drift Tube track finder algorithm. The three step scheme utilized is shown. On the left side, the pairwise matching algorithm is described. An extrapolated hit coordinate is calculated using the f1 coordinate and the bending angle of the source segment. The match is considered successful if a target segment is found at the extrapolated coordinate, inside a certain extrapolation window.

segments and the highest extrapolation quality. Once the track segment data are available to the Assignment Unit, memory based look up tables are used to determine the transverse momentum, the ϕ and η coordinates, and a track quality.

CSC trigger

The task of the CSC Track Finder is to reconstruct tracks in the endcap muon system and to measure the transverse momentum (p_T), pseudo-rapidity (η), and azimuthal angle (ϕ) of each muon. The measurement of p_T by the CSC trigger uses spatial information from up to three stations to achieve a precision similar to that of the Drift Tube Track Finder despite the reduced magnetic bending in the endcap. The CSC Local trigger provides a high rejection power against background by finding muon segments, also referred to as Local Charged Tracks (LCT), in the 6-layer endcap muon CSC chambers. Muon segments are first found separately by anode and cathode electronics (see Fig. 4.14) and then time correlated, providing precision measurement of

the bend coordinate position and angle, approximate measurement of the non-bend angle coordinate, and identification of the correct muon bunch crossing with high probability.

The primary purpose of the CSC anode trigger electronics is to determine the exact muon bunch crossing with high efficiency. Since the drift time can be longer than 50 ns, a multi-layer coincidence technique is used to identify a muon pattern and find the bunch crossing.

The primary purpose of the CSC cathode trigger electronics is to measure the ϕ coordinate precisely to allow a good muon momentum measurement up to high momentum. The charge collected on an anode wire produces an opposite-sign signal on several strips, and a precise track measurement is obtained by charge digitization and precise interpolation of the cathode strip charges. The six layers are then brought into coincidence in LCT pattern circuitry to establish the position of the muon to an RMS accuracy of 0.15 strip widths. Strip widths range from 6-16 mm. Cathode and anode segments are brought into coincidence and sent to CSC Track Finder electronics which links the segments from the endcap muon stations. Each Track Finder unit finds muon tracks in a 60^o sector. A single extrapolation unit forms the core of the Track Finder trigger logic. It takes the three dimensional spatial information from two track segments in different stations, and tests if those two segments are compatible with a muon originating from the nominal collision vertex with a curvature consistent with the magnetic bending in that region. Each CSC Track Finder can find up to three muon candidates. A CSC muon sorter module selects the four best CSC muon candidates and sends them to the Global Muon trigger.

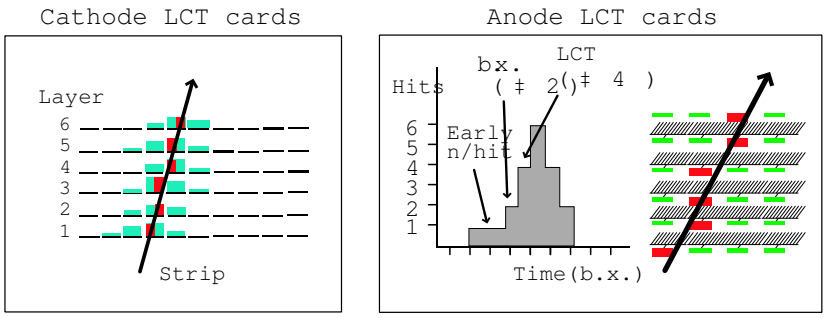

Figure 4.14: Principle of the CSC local trigger.

RPC trigger

The RPC pattern trigger Logic (PACT) is based on the spatial and time coincidence of hits in four RPC muon stations (see Fig. 4.15). Because of energy loss fluctuations and multiple scattering there are many possible hit patterns in the RPC muon stations for a muon track of defined transverse momentum emitted in a certain direction. Therefore, the PACT should recognize many spatial patterns of hits for a given transverse momentum muon. In order to trigger on a particular hit pattern left by a muon in the RPCs, the PACT electronics performs two functions: requires time coincidence of hits in patterns ranging from 3 (out of 4) muon stations to 4 (out of 6) muon stations along a certain road and assigns a p_T value. The coincidence gives the bunch crossing assignment for a candidate track. The candidate track is formed by a pattern of hits that matches with one of many possible patterns pre-defined for muons with defined transverse momenta. The p_T value is thus given. The pre-defined patterns of hits have to be mutually exclusive i.e. a pattern should have a unique transverse momentum assignment. The patterns are divided into classes with a transverse momentum value assigned to each of them. PACT is a threshold trigger; it gives a momentum code if an actual hit pattern is straighter than any of the pre-defined patterns with a lower momentum code. The patterns will depend on the direction of a muon i.e. on ϕ and η.

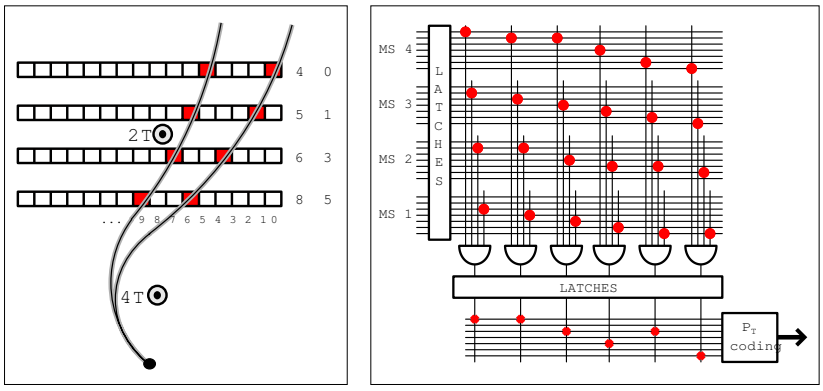

Figure 4.15: RPC trigger principle.

Global Muon trigger

The Regional Muon trigger reconstructs muon candidates in both the barrel and the endcap regions out of hits or track segments found at the muon stations. The Global Muon trigger receives the best four barrel DT and the best four endcap CSC muons and combines them with 4+4 muons sent by the RPC. It performs a matching based on the proximity of the candidates in (η , ϕ) space. If two muons are matched their parameters are combined to give optimum precision. If a muon candidate cannot be confirmed by the complementary system, quality criteria can be applied to decide whether to forward it. The Global Muon trigger also contains logic to cancel ghost tracks that arise when a single muon is found by more than one muon system and is not otherwise matched, such as at the boundary between the DT and CSC muon systems. The selected muon candidates are ranked on the basis of their transverse momentum, quality and to some extent pseudorapidity. The best four muon candidates in the entire CMS detector are sent to the Global trigger.

The Global Muon trigger also receives information from the calorimeters. The Regional Calorimeter trigger sends two bits based on energy measurements representing isolation and compatibility with a minimum ionizing particle in $\Delta\eta \times \Delta\phi = 0.35 \times 0.35$ trigger regions. The GMT extrapolates the muon tracks back to the calorimeter trigger towers and appends the corresponding isolation and minimum ionizing particle bits to the track data consisting of p_T, sign of the charge, η , ϕ and quality.

A simulation of the Level-1 Muon trigger has been implemented in the ORCA software, with emphasis on performing operations that are exactly bit-compatible with the operations performed by those electronic boards for which prototypes and firmware exist. The efficiency of the Global Muon trigger to identify single muons as a function of the generated transverse momentum is shown in Fig. 4.16 for several Level-1 thresholds. The muons were generated flat in pseudorapidity in $|\eta| <2.1$. The Level-1 thresholds shown are defined to correspond to 90% efficiency. The sharpness of the turn-on curves is determined by the p_T resolution obtained by the Global Muon trigger.

The single muon trigger rate as a function of the p_T threshold for both low and high luminosity is shown in Fig. 4.17. Also shown is the generated single muon rate and the trigger rates that would occur if the RPC system or

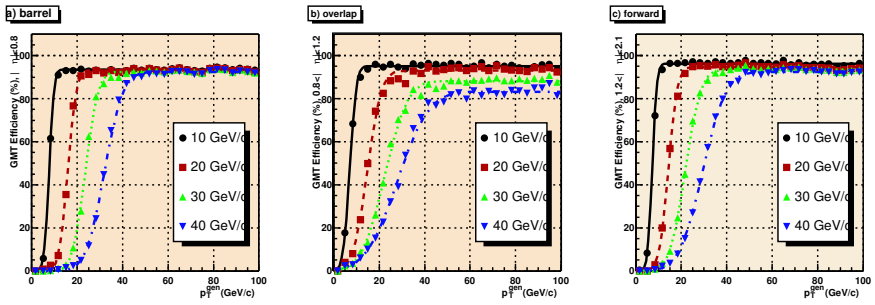

Figure 4.16: Efficiency of the Level-1 Muon trigger to identify single muons above several p_T thresholds as a function of the generated p_T , for three pseudorapidity intervals: a) $|\eta|$ <0.8, b) 0.8< $|\eta|$ <1.2, and c) 1.2< $|\eta|$ <2.1, $|\eta|$ <1.2.

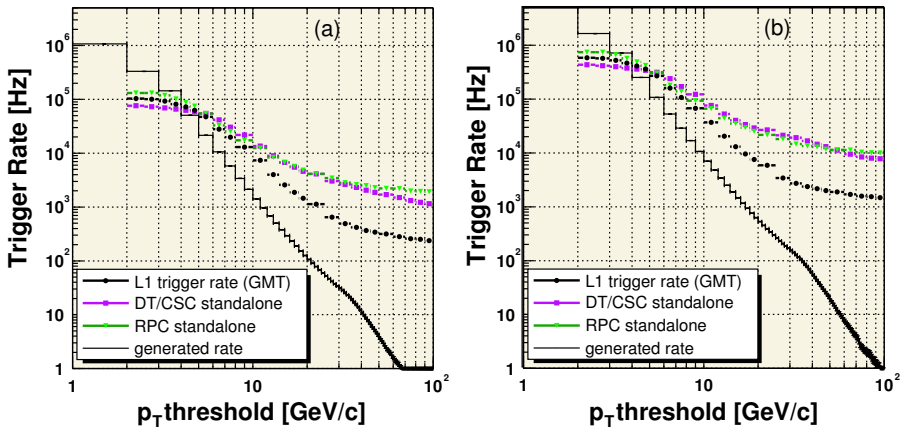

Figure 4.17: Level-1 muon trigger rate as a function of p_T threshold for low (a) and high (b) luminosity.

the combined DT/CSC systems would be operated standalone, without the optimization of the Global Muon trigger. Contours of equal rate from the Level-1 single and di-muon triggers, in the plane of the applied p_T thresholds, are shown in Fig. 4.18 for low and high luminosity. The threshold for the di-muon trigger applies to both muons. A bandwidth of 4 kHz is available for muon triggers at low luminosity, 8 kHz at high luminosity. The operating thresholds are 14 GeV/c and 3 GeV/c for the single and di-muon triggers at low luminosity, and 20 GeV/c and 5 GeV/c at high luminosity.

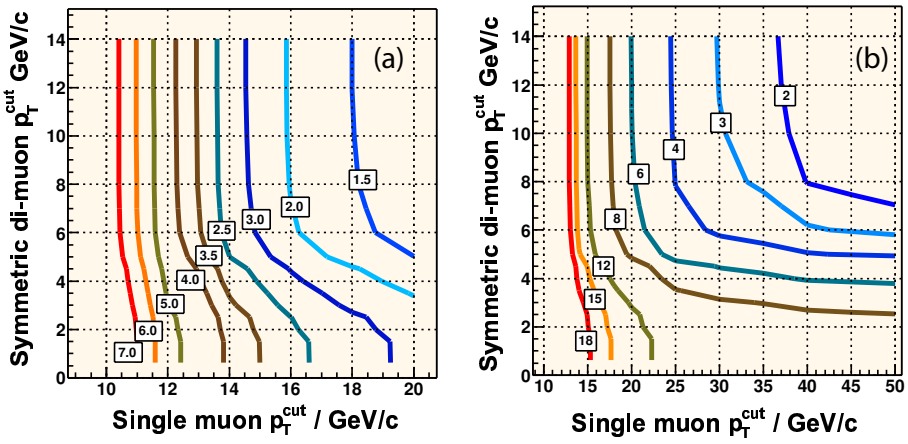

Figure 4.18: Contours of equal rate in the plane of p_T thresholds for Level-1 single and di-muon triggers at (a) L=$2 \times 10^3 3cm - 2s - 1$ and (b) L=$10^3 4cm - 2s - 1$.

4.1.3 Global trigger

The Global trigger accepts muon and calorimeter trigger informations, synchronizes matching sub-system data arriving at different times and communicates the Level-1 decision to the timing, trigger and control system for distribution to the sub-systems to initiate the read-out. The global trigger decision is made using logical combinations of the trigger data from the Calorimeter and Muon Global triggers.

The Level-1 trigger system sorts ranked trigger objects. This allows all trigger criteria to be applied and varied at the Global trigger level rather than earlier in the trigger processing. All trigger objects are accompanied by their coordinates in (η , ϕ) space. This allows the Global trigger to vary the thresholds based on the location of the trigger objects. It also allows the Global trigger to require trigger objects to be close or opposite from each other. In addition, the presence of the trigger object coordinate data in the trigger data, which is read-out first by the DAQ after the event is accepted at Level-1, permits a quick determination of the regions of interest where the more detailed higher level trigger analyses should focus. Besides handling physics triggers, the Global trigger is used in test runs and in calibration runs, not necessarily in phase with the machine, and for prescaled triggers, as this is an essential requirement for checking trigger efficiencies and recording samples of large cross section data. The Global Level-1 trigger transmits a decision to either accept

or reject a bunch crossing. The trigger Throttle System allows the reduction by prescaling or shutting off of accepted signals in case the detector read-out or DAQ buffers are at risk of overflow.

A summary of the Level-1 trigger threshold is presented in Table 4.3 for low luminosity and in Table 4.4 for high luminosity. The thresholds quoted correspond to the E_T or p_T value at which the efficiency of the trigger is 95% of its maximum value. In both cases, a 1 kHz bandwidth is allocated to minimum-bias events which will be used for calibration and monitoring purposes. There is no need for a muon+jet trigger at low luminosity owing to the low inclusive muon threshold.

Trigger	**Threshold (GeV)**	**Rate (kHz)**	**Cumulative Rate (kHz)**
Inlcusive isolated electron/photon	29	3.3	3.3
Di-electrons/di-photons	17	1.3	4.6
Inclusive isolated muon	14	2.7	7.0
Di-muons	3	0.9	7.9
Single tau-jet trigger	86	2.2	10.1
Two tau-jets	59	1.0	10.9
1-jet, 3-jets, 4-jets	177, 86, 70	3.0	12.5
Jet*E_T^{miss}	88*46	2.3	14.3
Electron*Jet	21*45	0.8	15.1
Minimum-bias (calibration)		0.9	16.0
Total			**16.0**

Table 4.3: Level-1 trigger table at low luminosity. Thresholds correspond to values with 95% efficiency.

Trigger	**Threshold (GeV)**	**Rate (kHz)**	**Cumulative Rate (kHz)**
Inlcusive isolated electron/photon	34	6.5	6.5
Di-electrons/di-photons	19	3.3	9.4
Inclusive isolated muon	20	6.2	15.6
Di-muons	5	1.7	17.3
Single tau-jet trigger	101	5.3	22.6
Two tau-jets	67	3.6	25.0
1-jet, 3-jets, 4-jets	250, 110, 95	3.0	26.7
Jet*E_T^{miss}	113*70	4.5	30.4
Electron*Jet	25*52	1.3	31.7
Muon*Jet	15*40	0.8	32.5
Minimum-bias (calibration)		1.0	33.5
Total			**33.5**

Table 4.4: Level-1 trigger table at high luminosity. Thresholds correspond to values with 95% efficiency.

4.2 High Level Trigger selection

The CMS DAQ/HLT complex processes all events accepted by the Level-1 trigger in a single processor farm. There is therefore no Level-2 or Level-3 trigger in CMS, but a single entity, the High Level Trigger, or HLT. Nevertheless, as in a traditional multi-level system, the selection of events can be optimized by rejecting background events as quickly as possible. The key aspect of the HLT

is the realtime nature of the selection. This imposes significant constraints on the resources that the algorithms can use and on the reliability of these algorithms. Events rejected by the HLT, with the exception of very small samples retained for monitoring the HLT performance, are lost forever. The correct functioning of the HLT is therefore a key issue for the CMS physics program. The main requirement from the physiscs point of view are:

- the selection must be as inclusive as possible. The LHC represents a new energy frontier, and unexpected new phenomena may appear. The selection requirements must not reject events of potential use in such exotic searches;
- all thresholds and other requirements applied by the selection should be such that detailed knowledge of calibration constants and other run conditions is not necessary in realtime;
- the final selection of events should include data samples for the calculation of all trigger and reconstruction efficiencies at the offline level;
- the rate of events accepted by the HLT should be within predefined limits approximately $\mathcal{O}(10^2)$ Hz;

For these reasons the basic strategy is to reconstruct those parts of each physics object that can be used for selection, minimizing the overall CPU usage.
As an example, reconstruction of an electron includes the reconstruction of a cluster in the electromagnetic calorimeter, the matching of hits in the pixel detector and the subsequent reconstruction of a full charged particle track in the tracker. At the end of each step a set of selection criteria results in the rejection of a significant fraction of the events accepted by the previous step. The rate of events that need to be processed through the remaining algorithms decreases step by step thus reducing the required CPU. Reconstruction and selection are therefore closely intertwined in the online environment of the filter farm. For an optimal system the HLT should reconstruct the minimum amount of detector information that reject background events while keeping the desired physics events for further processing.
The reconstruction and selection in the HLT takes place in steps which correspond roughly to what would have been distinct Level-2 and Level-3 trigger systems. It is thus convenient to use this terminology, and to refer to a Level-2

trigger or a Level-3 step to describe the selection algorithms and criteria of the HLT. Clearly, in the CMS HLT there is no sharp division between these trigger steps, other than the order in which they are applied.
In what follows, the convention used is that "Level-2" triggers, algorithms and requirements refer to the first selection step in the HLT process. Typically, a Level-2 trigger, which has the maximum rate, uses information only from the calorimeters and the muon detectors. In contrast, Level-3 refers to selection that includes the reconstruction of full tracks in the tracker. Traditionally, because of the high number of channels, the complex pattern recognition and the high combinatorics, track reconstruction is a process that demands large amounts of CPU time. Carrying the analogy even further, in what follows there are references to Level-2.5 triggers, which indicate algorithms that use partial tracker information, e.g. pixel hits for a fast confirmation of an electron candidate. The numbering, 2.5, attempts to indicate the intermediate nature of the selection, that occurs between the Level-2 selection based only on calorimeters, and the Level-3 selection based on the full CMS tracker information.
Reconstruction of charged particle tracks in the CMS detector has turned out to be a task that demands less CPU time than previously expected, so that some of the selection algorithms may change in the future. As an example, if full charged-track reconstruction becomes faster than the fast pixel reconstruction in the electron selection, the two steps will be interchanged in the HLT. This flexibility is the major advantage of executing the full selection in a single processor farm: the system can make optimal use of the most recent advances not only in computing but also in the algorithms and in the corresponding software tools.
To minimize the CPU required by the HLT, a key feature of the algorithms is to reconstruct only partially the available information in the CMS detector. For instance in many cases the decision on whether an event should be accepted by the HLT or not, can be restricted to a limited region of the detector. As an example, for an event accepted by the Level-1 trigger in the inclusive muon stream, only the parts of the muon chambers pointed to by the Level-1 trigger and the corresponding road in the tracker, need to be considered for the validation of the muon.
The idea of partial event reconstruction has been embedded in the CMS reconstruction code from the very beginning. In the case of the HLT, the reconstruc-

tion of physics objects is driven by the corresponding candidates identified by the Level-1 trigger. Except in a few cases, which are indicated, all reconstruction described in this chapter starts from the Level-1 trigger information. This approach leads to significant CPU savings, however it also leads to rejecting events that contain objects that were allocated in other trigger chain and did not pass the Level-1 trigger. This disadvantage is mitigated by the fact that, in general, it is very difficult to understand the properties of such objects in later offline analyses. It is clearly always possible, albeit with an increased CPU cost, to look for additional objects in each event if a particular physics analysis raises such a requirement.
The possibility to use the tracker information at HLT level permits the definition of a physics object which cannot be defined at the Level-1 trigger stage: the b-jet. Starting from a generic jet, using the algorithm implemented for off-line analysis to tag b-jet (see next chapter for more details), it is possible to say if it comes from the fragmentation of a b quark or not. In the next sections I will concentrate on the HLT analysis chains, putting more emphasis on the τ-jet selection which has been the most significant contribution of the candidate.

4.2.1 τ-jets identification

The identification of τ-jets involves informations from the calorimeters and from the tracking detectors. The following definitions will be used in the discussion that follows:

- first (second) "Level-1 τ-jet" is the first (second) jet from the τ-jet list provided by the Global Calorimeter trigger. Jets in this list are ordered by E_T (first jet has the highest E_T).
- first (second) "Calo jet" is a jet reconstructed with the calorimeters in a region centred on the first (second) Level-1 τ-jet.
- staged Pixel Detector (staged pixels): the pixel detector configuration with 2 barrel layers and 1 forward disk; full Pixel Detector (full pixels): 3 barrel layers and 2 forward disks.

Level-2 calorimeter based τ selection

The τ lepton decays hadronically 65% of the time, producing, together with a ν_τ, a "τ-jet", which is a jet-like cluster in the calorimeters, containing a relatively small number of charged and neutral hadrons. When the p_T of the τ-jet is large compared to its mass, these hadrons have relatively small transverse momentum with respect to the jet axis. In 77% of hadronic decays, the τ-jet consists of only one charged hadron and a number of π^0s. These decays are referred to as "one prong" decays. The features of hadronic decays listed above lead to the fact that they produce relatively narrow jets in the calorimeter. Defining a radius as $\sqrt{(\Delta\eta)^2 + (\Delta\phi)^2}$ (with ϕ measured in radians), about 90% of the τ-jet energy is contained in a very small cone of radius 0.15-0.20 and about 98% in a cone of 0.4 for τ-jets with $E_T > 50$ GeV. Another feature of τ-jets is a localised energy deposition in the electromagnetic calorimeter. This feature is quantified by the electromagnetic isolation parameter which is defined as:

$$P_{isol} = \sum_{\Delta R_i < 0.4} E_{T,i} - \sum_{\Delta R_i < 0.13} E_{T,i} \tag{4.1}$$

where the sum runs over the crystals of the electromagnetic calorimeter, ΔR_i is the distance in $\eta - \phi$ space from the τ-jet axis to the i-th crystal and $E_{T,i}$ is the transverse energy measured in this i-th crystal. The identification of a τ-jet proceeds with the reconstruction of a jet in a region centered on the Level-1 τ-jet. To find the jet the Iterative Cone algorithm [113] with a cone size of 0.6 is used. The algorithm searches the maximum transverse energy object and throws a cone around its direction. Any object within that cone will be merged to form a proto-jet. The proto-jet direction is calculated from the energy weighted directions of the constituents, and a cone is thrown around the new direction to form a new proto-jet. The procedure is repeated until the proto-jet does not change significantly between two iterations, what means that the jet energy change is smaller than a tunable value (1% by default) and is below a tunable threshold (0.01 GeV by default). The constituents are removed from the list of objects, and the procedure is repeated until no objects are left in the list. To speedup the jet finding process only the calorimeter towers located within a cone of radius 0.8 around the Level-1 τ-jet directions are used as input. For each jet found, the electromagnetic isolation parameter P_{isol} is calculated. Jets with $P_{isol} > P_{isol}^{cut}$ are considered as τ candidates.

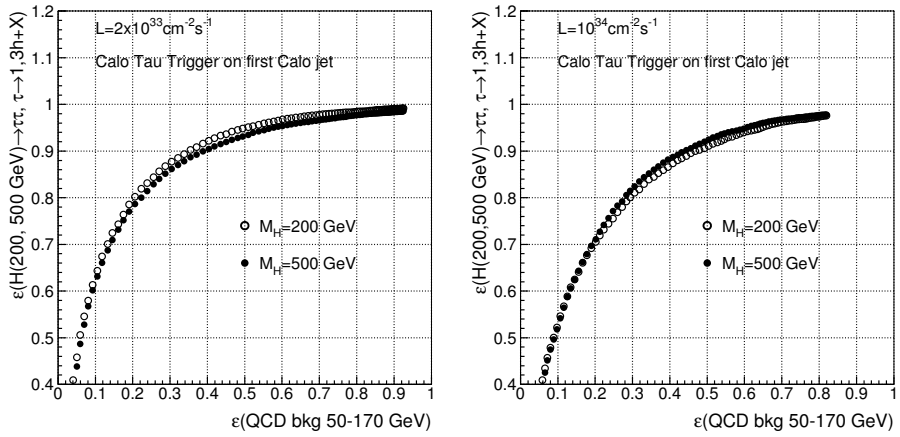

Figure 4.19: Efficiency for the Calo τ trigger for the first Calo jet in $A^0/H^0 \to 2\tau \to 2\tau$-jets and QCD 2-jet events. $M_H = 200$ and 500 GeV/c^2 for the low (left) and high (right) luminosity

The identification of a τ-jet with the algorithm described above will be referred to as the "Calo Tau trigger". The efficiency of the Calo Tau trigger for $A/H \to \tau\tau$, with both τ leptons decaying hadronically, and for QCD background events (with at least two jets in the final state) when the value of P_{isol}^{cut} is varied, is shown in Fig. 4.19, for both low and high luminosities. The Calo τ identification has been applied on the first Calo jet only. It can be seen that the efficiency of the Higgs selection is essentially independent of the Higgs mass. The reason is that the efficiency of τ-jet identification using the parameter P_{isol} does not depend on the E_T and η of the τ-jet. Details of the Calo τ trigger optimization can be found in [108]. The entire selection procedure is very fast as can be seen in Table 4.5 where the time required to build groups of calorimeter towers and the time needed for regional jet finding and for the calculation of the isolation parameter P_{isol} are listed.

algorithm step / luminosity	L=$2 \times 10^3 3cm^{-2}s^{-1}$	L=$10^3 4cm^{-2}s^{-1}$
build calorimeter tower	24	39
regional finding of Calo jets and P_{isol} calculation	9	15
Total time (msec)	33	54

Table 4.5: Time, in ms, for τ-jet identification with the calorimeters for QCD events.

Level-2 τ selection based on tracker isolation

In this paragraph we describe an algorithm to select τ-jets using the information from reconstructed tracks. It will be referred to as the "Trk τ trigger". Due to CPU time limitations it is not possible to perform a full tracker reconstruction on all events accepted by the Level-1 trigger; it will be anyway possible to read and reconstruct a selected part of the tracker data. The Trk τ trigger performs the reconstruction only of tracks confined in restricted regions of interest ("regional tracking") [114], defined by cones around each jet direction identified by the Calo jet reconstruction. Another important piece of information is the position of the signal vertex (also called primary vertex) defined as the vertex with the maximum $\sum |p_T|$ of the associated tracks. A track is associated to a vertex if the distance of the z_{imp} (i.e. the z coordinate of the helix at the point of minimum distance from the z axis) of the track from the signal vertex position in z is below a certain value. To find the signal vertex an iterative algorithm is usually used. The tracks are clustered on the basis of their z_{imp} and the position of the vertex is calculated with the average of the z_{imp} of the tracks in the same cluster. Then the tracks are clustered again considering the position of the vertices found in the previous step. The new position of the vertex is calculated and the algorithm is run again. The algorithm stops as soon as the positions of the vertices converge.
In order to speed up the vertex reconstruction, tracks reconstructed only with the hits in the three pixel layers, instead of the full tracker, are used. Tracks reconstructed is such a way are named pixel lines.
Once the primary vertex is found the regional track reconstruction starts. The regional reconstruction algorithm is based on the standard track reconstruction, but it selects seeds only in a region of interest. In our case the region of interest corresponds to the jet cone. Only the tracks having z_{imp} compatible with the signal vertex are taken into account. A further improvement of the timing performance is obtained by stopping the track reconstruction as soon as a given condition is fulfilled (conditional track finding). Track reconstruction is stopped when six hits have been associated with a helix. This gives an acceptable resolution on the track parameters and a low ghost rate. The possibility to start with the two pixel barrel layers (staged pixels scenario) has also been studied at low luminosity. An isolation made with the reconstructed tracks is then performed. This step is named Trk τ trigger.

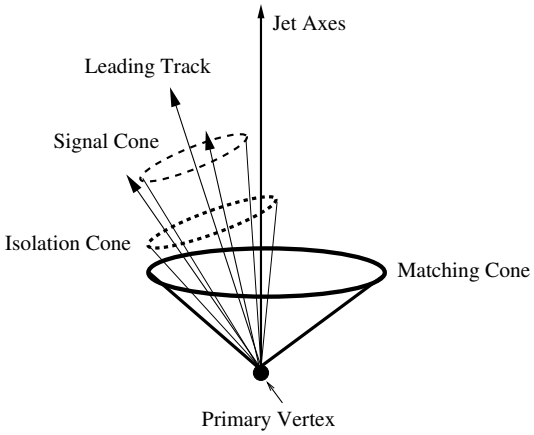

Figure 4.20: Sketch of the basic principle of τ-jet identification using charged particle tracks.

The Trk τ trigger [109] relies on a tagging criterion based on an isolation requirement for the reconstructed tracks. Figure 4.20 shows a sketch of the isolation procedure. To reduce the contamination from soft tracks, only tracks with $p_T > 1$ GeV/c and z_{imp} compatible with the z position of the signal vertex are considered; such tracks are referred to as "good tracks". The isolation-based tagging compares the number of good tracks within a "signal cone" ($R = R_{SIG}$) and within an "isolation cone" ($R = R_{ISO} > R_{SIG}$). Each cone is defined around the direction of the leading track i.e.the highest p_T track found in the "matching cone" ($R_M = 0.1$), around the Calo jet direction. Trk τ trigger requires zero good tracks in the ring $R_{SIG} < R < R_{ISO}$. The sizes of R_{SIG} and R_{ISO} cone are chosen in order to optimise the signal over background ratio. Higher background reduction can be obtained by requiring the transverse momentum of the leading track to exceed a few GeV/c. Due to the strong dependence of the track p_T spectrum on the Higgs mass and on the hadronic decay mode, particular attention is required in optimising the cut on the leading track transverse momentum (P_T^{LT}). The Trk τ algorithm is found to provide the same efficiency for one and three prong decays, as shown in Table 4.6 where $R_{ISO} = 0.45$, $R_{SIG} = 0.06$, $P_T^{LT} > 5GeV/c$ (from $A^0/H^0 \rightarrow 2\tau \rightarrow 2\tau$-jets events).

The uniformity of the tagging efficiency with respect to one-prong and three-prong decays is not surprising since the broadening of the three-prong jets, which degrades the isolation, is compensated by the harder leading track spectrum. Infact in a one-prong decay a small number of neutral pions are also pro-

	M_H=200 GeV/c^2		M_H=500 GeV/c^2	
	one-prong	three-prongs	one-prong	three-prongs
1st jet	62%	63%	67%	70%
2nd jet	61%	54%	62%	67%

Table 4.6: Efficiency of Trk τ trigger algorithm for first and second calo jets for 1 and three-prong τ decays.

duced, while in the three-prong decay the number of neutral pions is smaller. On average the number of particle produced in both decays is the same, but in the three-prong decay the probability that a charged particle has the maximum p_T is greater than in the one-prong case.

Trk τ trigger performance

Figure 4.21 (left plot) shows the Trk τ trigger performance at low luminosity for both the full and staged pixel systems in terms of the signal vs background algorithmic efficiency. Trk τ identification has been applied for the first Calo jet in $A^0/H^0 \rightarrow 2\tau \rightarrow 2\tau$-jets and QCD events. The different points correspond to the different size of the isolation cone R_{ISO} varied between 0.2 and 0.45. It can be seen that, at the same QCD background efficiency, the signal efficiency reduces by about of 15% in the staged pixels scenario. Figure 4.21 (right plot) shows the results obtained at high luminosity. Since the algorithm has to fulfill stringent CPU time limitations (discussed later in this chapter), particular attention has been put in its optimization. To improve the timing performance without affecting signal and background efficiencies the track reconstruction has been divided in two steps:

1. reconstruct tracks inside a cone of radius $R_M = 0.1$ around the Calo jet direction, searching for the leading track. If the leading track does not exist or it is not isolated in the ring $R_{SIG} < R < R_M$, the reconstruction is stopped and the event is rejected; otherwise the second step starts.

2. reconstruct tracks inside a ring between R_M and 0.45 around the jet axis. At the end of the second step all tracks in the region of interest have been reconstructed and isolation is applied again.

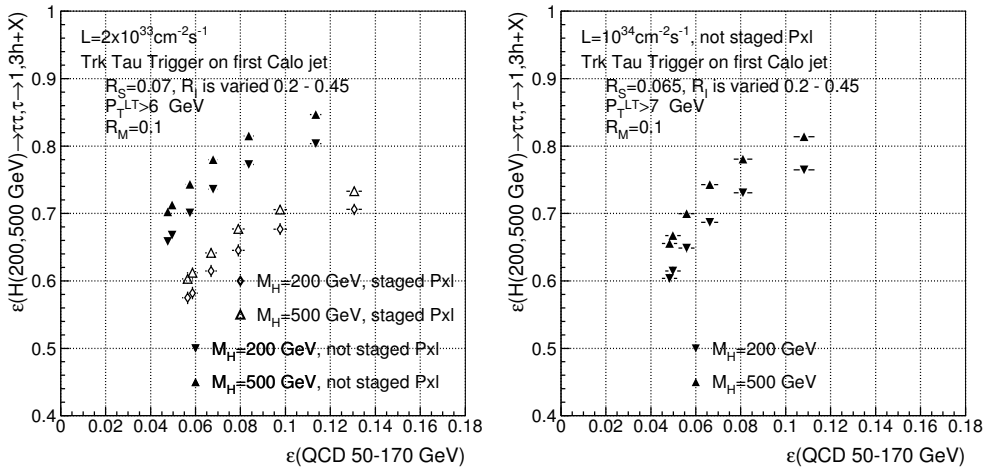

Figure 4.21: Efficiency of Trk τ trigger for the first Calo jet in $A^0/H^0 \rightarrow 2\tau \rightarrow 2\tau$-jets vs that in QCD event. Left: for L=$2\times10^{33}cm^{-2}s^{-1}$, for both the full and staged pixel systems. Right: for L=$10^{34}cm^{-2}s^{-1}$. Two Higgs masses M_H=200 and 500 GeV/c^2, are shown.

From Fig. 4.21 it is clear that the nedded background rejection ($\sim$ 1000) cannot be achieved triggering only on the first Calo jet. It is necessary to consider also the second Calo jet in the event. So the Trk τ trigger is applied not only to the first Calo jets, but also to the second one. If there is only one Calo jets the event is rejected. Figure 4.22 (left plot) shows the signal vs. background algorithmic efficiency, at low luminosity, for the complete and staged pixel detector. The different points correspond to the different sizes of the isolation cone R_{ISO} which is varied between 0.2 and 0.45: it is possible to see that, at a QCD background efficiency of $\sim 10^{-3}$, the signal efficiency with the staged pixel detector is reduced by about 12% (20%) for 200 (500) GeV Higgs.
Figure 4.22 (right plot) shows the results obtained at high luminosity. A cut on p_T of the leading track of 6 (7) GeV/c is required for low (high) luminosity to reach the background rejection factor of 10^3.

The Trk τ trigger time distribution is shown in Fig. 4.23 for the Higgs events and for the QCD background at low luminosity. The time needed for the double tag is only slightly larger than the time needed for a single tag, since the second Calo jet is analysed only in the $\sim$6% of the background events which pass the selection on the first Calo jet. From the same plot one can see that only 10% of the QCD events require more than 500 ms to be analysed. Timing at high luminosity represents a problem, because the time for the pixel recon-

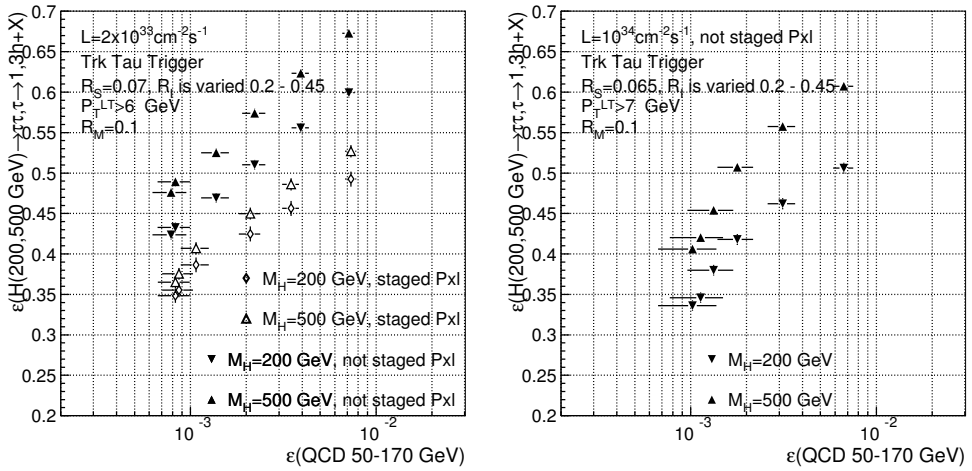

Figure 4.22: Efficiency of Trk τ trigger applied to both Calo jet in $A^0/H^0 \rightarrow 2\tau \rightarrow 2\tau$-jets vs that in QCD events. Left: for L=$2 \times 10^{33} cm^{-2} s^{-1}$, for both the full and staged pixel systems. Right: for L=$10^{34} cm^{-2} s^{-1}$. Two Higgs masses M_H=200 and 500 GeV/c^2, are shown.

struction step increases too much with respect to the low luminosity scenario. To achieve the desired goal, i.e. less than 500 msec per event, we can use the tracker isolation plus the calorimetric criterion described in section 4.2.1. Indeed, applying Trk τ trigger only to those events passing the Calo tau selection on the first jet, we can reduce the needed time to the desired quantity. Considering a calorimetric efficiency on background events of about 33% the total time for analyzing a double-jet event with this method becomes less than 400 msec/event, which is acceptable. As shown in Fig. 4.24 the efficiency of this method is similar to the efficiency presented above. In this last period another algorithm for track reconstruction is being implemented for the high luminosity scenario. Preliminary results show that this algorithm permits the same efficiency as the one used for this thesis and is much faster. If the preliminary results are confirmed with higher statistics it will be possible to use Trk τ trigger also at high luminosity without using the calorimeter preselection.

Results similar to those described in the pages above can be achieved using Level-2 calorimeter isolation on the first Calo jet and the tracker isolation algorithm to both jets using the pixel lines instead of the reconstructed tracks. This method is slightly faster than using full tracker tracks but the signal efficiency is about 14% lower. However the resolution in p_T achieved using only

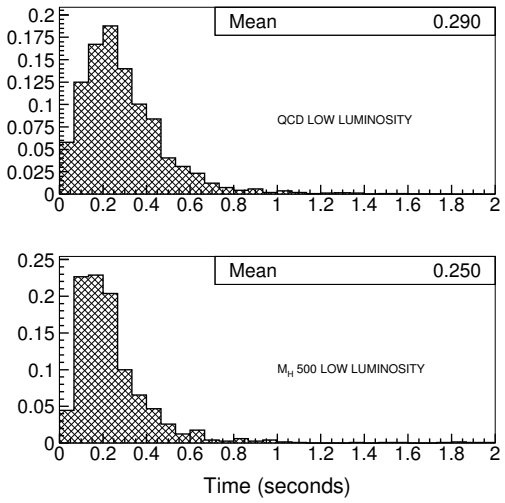

Figure 4.23: Trk τ trigger reconstruction time (in seconds) for double tagging with Trk τ trigger at low luminosity. Upper plot: QCD events. Lower plot: $A^0/H^0 \rightarrow 2\tau \rightarrow 2\tau$-jets events.

the pixel reconstruction is not enough to permit a hard cut on the p_T of the leading track (bigger than 5 GeV) and this fact doesn't allow the use of pixel detector to trigger events with only one τ-jet. As explained in the next session, the only way to achieve an acceptable background rejection, for the single τ trigger case, is to increase the cut on p_T of the leading track to 20-25 GeV/c.
Tab. 4.7 summarizes the efficiency for 200 and 500 GeV Higgs mass, in different situations (staged and full pixel scenario, tracker and tracker+calorimeter selection) for low and high luminosity at a fixed background rejection of about 10^3. In a scenario with staged pixel detector the efficiency are lower than in the full pixel scenario. At high luminosity we expect a degradation of performances due to the bigger number of pile-up event superimposed.

Single τ-jet selection

The Trk τ trigger will work as the final part of the trigger path selecting MSSM charged Higgs boson in the process $gb(g) \rightarrow H^+t(b)$, $H^+ \rightarrow \tau\nu \rightarrow \tau$-jet, $t \rightarrow bjj$ [120]. Level-1 single τ trigger, followed by a selection with the High Level trigger of the events with large E_T^{miss} ($>$ 70 GeV at low and $>$ 100 GeV at high luminosity), gives an output rate of about 30 Hz. The Trk

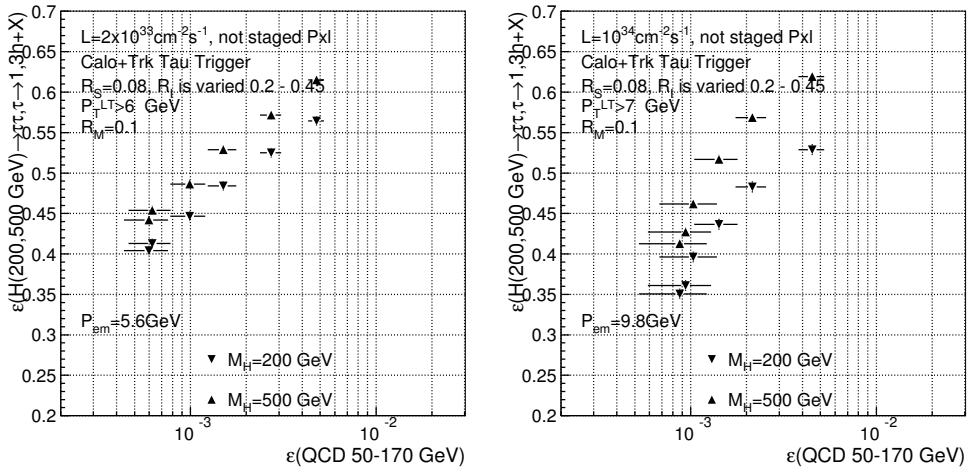

Figure 4.24: Efficiency when the Calo τ trigger selection applied on the first Calo jet is followed by Trk τ trigger on both Calo jets for $A^0/H^0 \rightarrow 2\tau \rightarrow 2\tau$-jets vs that in QCD event. Left: for L=$2 \times 10^{33} cm^{-2} s^{-1}$, for both the full and staged pixel systems. Right: for L=$10^{34} cm^{-2} s^{-1}$. Two Higgs masses M_H=200 and 500 GeV/c^2, are shown.

Luminosity	**Configuration/Trigger**	M_H **= 200 GeV**	M_H **= 500 GeV**	**QCD**
Low	staged pixels, Trk τ	0.355 ± 0.006	0.375 ± 0.005	(8.6 ± 1.6)×10^{-4}
Low	full pixels, Trk τ	0.433 ± 0.006	0.489 ± 0.005	(8.3 ± 1.6)×10^{-4}
Low	full pixels, Calo+Trk τ	0.446 ± 0.006	0.486 ± 0.005	(1.0 ± 0.2)×10^{-3}
High	Trk τ	0.346 ± 0.006	0.420 ± 0.005	(1.13 ± 0.4)×10^{-3}
High	Calo+Trk τ	0.361 ± 0.006	0.427 ± 0.005	(9.4 ± 3.0)×10^{-4}

Table 4.7: Summary of Trk τ trigger efficiency when applied to two Calo jets. The third and fifth rows show the results when also the Calorimeter τ trigger selection is applied on the first Calo jet. Due to the limited Monte Carlo statistics, some efficiency errors for QCD background are large.

τ trigger has to provide then a suppression factor of roughly 30 or more, to match the bandwidth requirements. Trk τ trigger selection is applied on the Calo jet reconstructed in the region of the 1st Level-1 τ jet. The purity of the Calo jet is 85%. Isolation criteria, used in Pxl or Trk τ triggers, cannot provide the required suppression factor of 30, but with Trk τ trigger it is possible to apply a cut on the momentum of the leading track to obtain an additional rejection of the QCD background. Fig. 4.25 shows the Trk τ trigger algorithmic efficiencies for the signal and QCD background events selected by Level-1 single τ trigger. As shown in the plots a background rejection of 30

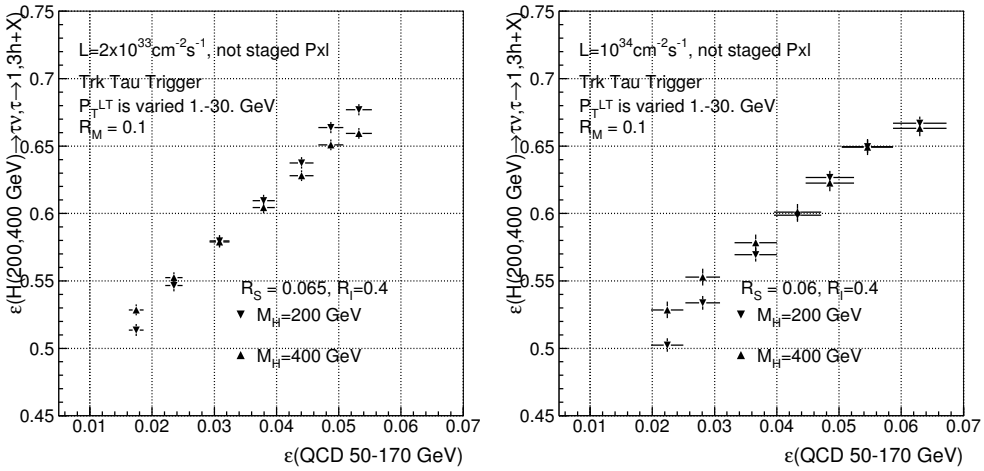

Figure 4.25: Trk τ trigger efficiency for $H^+ \to \tau\nu \to \tau$-jet events vs the QCD background efficiency. The results are given for M_H= 200 GeV/c^2 and M_H= 400 GeV/c^2. Isolation parameters are: R_M=0.1, R_{SIG}=0.065 (0.060) for low (high) luminosity, R_{ISO}=0.4; cut on p_T of the leading track is varied from 1 to 30 GeV/c. Left: for L=$2 \times 10^{33} cm^{-2} s^{-1}$, for the full pixel systems. Right: for L=$10^{34} cm^{-2} s^{-1}$.

can be achieved with a signal efficiency of about 55%.

4.2.2 Electron identification

The selection of electrons and photons proceeds in three steps. The first step, Level-2.0, uses the Calorimeter information alone. The next steps, Level-2.5 and Level-3, demand hits in the pixel detectors consistent with an electron candidate and uses full track reconstruction. This attempt to match a special ECAL cluster, called supercluster, to hits in the pixel detector divides the electromagnetic triggers into two streams: electron candidates (single and double), and, above significantly higher thresholds, photon candidates. The selection of photons can use isolation cuts and rejection of π^0s based on lateral shower shape and on the reconstruction of converted photons.
In order to reconstruct with good quality and efficiency even low energy electrons (i.e. electrons with p_T of order of 20 GeV) the ECAL clustering has to include all energy radiated by electrons in the tracker material. The algorithms used to reconstruct efficiently the electrons allow also an adequate reconstruction of photon, even those that have converted in the tracker material.

For the final reconstruction of photons with high precision it is envisaged that unconverted photons will be reconstructed using energy sums of fixed arrays of crystals (probably 5×5 crystals), and that the tracker information will be used to assist in the clustering for converted photons. These algorithms to refine the photon energy resolution are not needed for the HLT selection, and have not yet been fully developed, although much of the necessary work has been started in studies of π^0 rejection.

Calorimeter reconstruction

The first step in the reconstruction of an electron (photon) in the High Level Trigger is the clustering of the energy deposits in the electromagnetic calorimeter (ECAL) and the estimation of the electron (photon) energy and position from this information. In the barrel section this involves the energy deposited in the lead tungstate crystals alone, while in the endcaps energy is also deposited in the $\sim 3X_0$ thick preshower detector.
Electrons radiate in the material between the interaction point and the ECAL. The bending of the electron in the 4T magnetic field results in a spray of energy detected in the ECAL. The spreading of this spray is, to good approximation, only in the ϕ direction. The electron energy can be collected by making a cluster of clusters along a ϕ road. This cluster of clusters is called a *super-cluster*. There exists two algorithms for the calorimetric reconstruction:

- the *Island algorithm* starts with a search for seeds that are defined as crystals with an energy above a certain threshold. Starting from the seed position, adjacent crystals are examined, scanning first in ϕ and then in η. Along each scan line crystals are added to the cluster. Only crystals with energy deposits which decrases monotonically from the seed crystal are added. The algorithm stops either when a crystal with a higher energy is found or when a crystal without an energy deposition is found.
  In the same way as energy is clustered at the level of calorimeter cells, non-overlapping clusters can in turn be clustered into calorimetric superclusters . The procedure is seeded by searching for the most energetic cluster and then collecting all the other nearby clusters in a very narrow η-window and a much wider ϕ-window;

- the *Hybrid algorithm* uses the η-ϕ geometry of the barrel crystals to exploit the knowledge of the lateral shower shape in the η direction (taking a fixed bar of three or five crystals in η), while searching dynamically for separated (bremsstrahlung) energy deposit in the ϕ direction. The Hybrid algorithm is designed to reconstruct relatively high energy electrons in the barrel (so far we have used it for electrons with p_T >10 GeV/c). By contrast, when looking for small deposits of energy in individual clusters, for example when making a calorimetric isolation cut, the basic clusters of the Island algorithm are more appropriate objects to work with.

Further details about the clustering algorithms can be found in [121]

Energy and position measurement

A simple position measurement of the shower can be obtained by calculating the energy-weighted mean position of the crystals in the cluster. The crystals in the CMS ECAL are quasi-projective, and do not exactly point to the nominal interaction vertex. So the lateral position (η,ϕ) of the crystal axis depends on the depth as illustrated in Fig. 4.26. A depth t_{max} thus needs to be defined. This depth is something like the longitudinal centre of gravity of the shower, and its optimal mean value varies logarithmically with the shower energy. There is a dependence on particle type, electron showers have a maximum about one radiation length less deep than photon showers. In the position measurement used for both Island and Hybrid super-clusters the depth is measured from the front face of the crystals along the direction identified from the nominal vertex position to the approximate shower position. This position is calculated using the energy weighted mean of the centres of the shower front face. The second issue that requires a more detailed treatment is related to the lateral shower shape. Since the energy density does not fall away linearly with the distance from the shower axis, but rather exponentially, a simple energy weighted mean of crystal energies is distorted and the measured position is biased towards the centre of the crystal containing the largest energy deposit. This bias is removed by applying a position correction algorithm. The weighted mean is calculated using the logarithm of the crystal energy:

$$x = \frac{\sum x_i W_i}{\sum W_i} \tag{4.2}$$

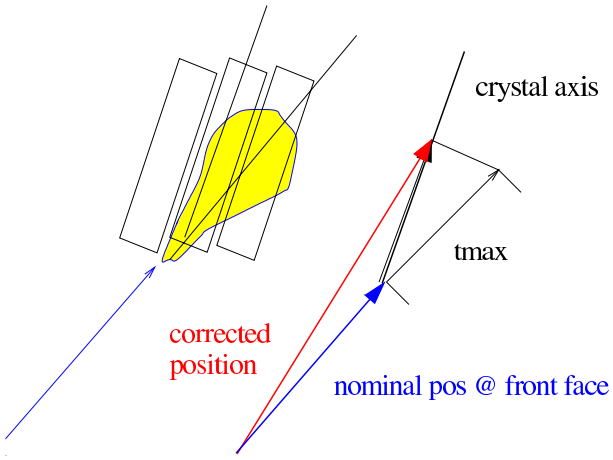

Figure 4.26: Illustration of crystal off-pointing.

where x_i is the position of crystal i, and W_i is the logarithmic weight of the crystal,i.e. the logarithm of the fraction of the cluster energy contained in the crystal, calculated with the formula:

$$W_i = W_0 + \log\left[\frac{E_i}{\sum E_i}\right] \tag{4.3}$$

where the weight is constrained to be positive, or is otherwise set to zero. W_0 then controls the smallest fractional energy that a crystal can have and still contribute to the position measurement. More details can be found in [121].
So far what has been described refers to the measurement of the position of a single cluster. The position of a super-cluster is calculated by making the energy-weighted mean of the positions of its component clusters. An important point here is that the energy-weighted mean impact position of an electron and of the photons it has radiated in its passage through the tracker material corresponds to the position at which a non-radiating electron would have impacted. It is this position that we have to measure to enable the correct reconstruction of the original electron path from the vertex. So, although it is unimportant for the energy measurement whether the crystal energy deposits of the electron and its radiated photons are all collected into a single cluster or into separate clusters, correctly clustering the energy deposits improves the ϕ measurement of an electron impact point. If the electron and a bremsstrahlung photon fall into the same cluster then the weighting of their contributions is the logarithmic weighting and not the linear weighting.

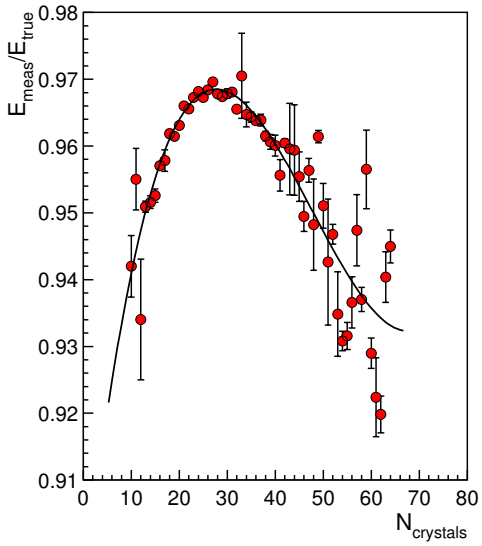

Figure 4.27: E_{meas}/E_{true} as a function of the number of crystals in a Hybrid super-cluster together with a fitted polynomial function.

Energy measurement and corrections

The measurement of energy in the crystals is obtained by simple addition of the deposits measured in the crystals.
Even in the areas not covered by the preshower detector the energy containment of the clustered crystals is not complete. The reconstructed energy distribution, E_{meas}/E_{true}, shows a peak at a few percent less than unity and a long tail on the low side due to unrecovered bremsstrahlung energy. The Gaussian part of the distribution corresponds, roughly, to the energy that would be reconstructed as an electron in absence of bremsstrahlung. The amount of tracker material varies strongly with η, and so does the amount of bremsstrahlung radiation, so a variation in the fraction of events falling in the tail as a function of η is expected. This inevitably leads to a small variation in the peak position as a function of η. The energy scale is calibrated using corrections designed to place the peak in E_{meas}/E_{true} at 1.0. The corrections are parameterized in terms of the number of crystals in the cluster. This helps to minimize the residual dependence of the energy scale on E and η. Fig. 4.27 shows, as an example, E_{meas}/E_{true} as a function of the number of crystals in a reconstructed Hybrid super-cluster, for electrons with $10 < p_T < 50$ GeV/c, together with a fitted polynomial function. Fig.4.28 shows the distribution of

E_{meas}/E_{true} for $p_T = 35$ GeV/c electrons reconstructed using the Hybrid algorithm in the barrel, and using the Island algorithm and the preshower in the endcap. The energy resolution is parametrized in two ways: in terms of the fitted width of the Gaussian part of the distribution (fitted between -1.5σ and +2.0σ), and in terms of σ_{eff} , defined as the half-width containing 68.3% of the distribution. If the distribution is Gaussian then σ_{eff} is just the Gaussian sigma, if the distribution has more significant tails then σ_{eff} provides some measure of this. The parameter σ_{eff} reflects more adequately than σ the final physics performance. Fig. 4.29 shows the position resolution in η and ϕ for the same sample. It is clear how the distribution in η is narrower than in ϕ.

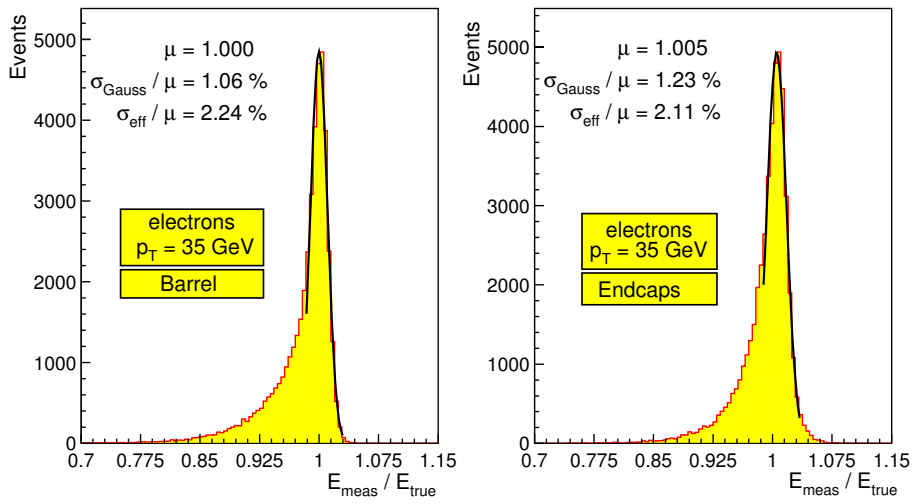

Figure 4.28: Distribution of E_{meas}/E_{true} for $p_T = 35$ GeV/c electrons, a) in the barrel ECAL fully digitized without pileup, and reconstructed with the Hybrid super-clustering algorithm, b) the same distribution for electrons in the endcap, reconstructed with the Island super-clustering algorithm, and with preshower energy included.

HLT electron/photon selection

The first step of the High Level Trigger, using only calorimeter information, is to reconstruct an ECAL super-cluster in a region specified by the Level-1 trigger. The super-cluster is then required to have E_T above a threshold chosen to give 95% efficiency for electrons at the same point on the E_T scale at which the Level-1 trigger has 95% efficiency. The same threshold is required

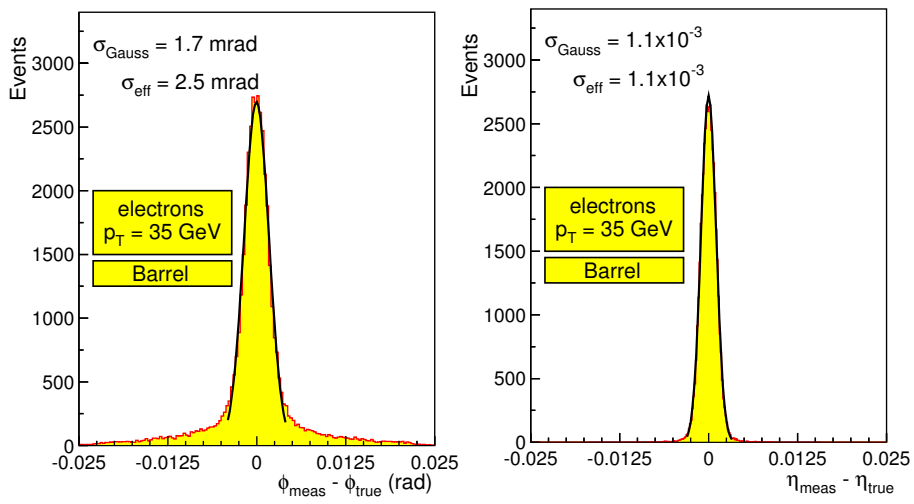

Figure 4.29: Position resolution for p_T = 35 GeV/c electrons in the barrel ECAL, fully digitized without pileup, and reconstructed with the Hybrid super-clustering algorithm.

for both objects in the double trigger. At low luminosity the thresholds are 26 GeV for the single, and 14.5 GeV for the double trigger. The corresponding thresholds at high luminosity are 31 GeV and 16.9 GeV.

The matching of super-clusters reconstructed in the calorimeter to hits in the pixel detector is the Level-2.5 step. It takes advantage of the fact that the energy-weighted average impact point of an electron together with the bremsstrahlung photons it has radiated is precisely the point where a non-radiating electron would have impacted. It is this space-point that the position measurement of the super-cluster attempts to determine. This point can be propagated back through the field to obtain an estimate of the direction of the electron at the vertex, and the hit positions expected in the pixel detector. Since most of the tracker material lies after the pixel detector, most electrons do not radiate significantly before it, and most photon conversions take place after it. So matching hits are found for most electrons and for very few photons.

The Level-3 selection includes all further requirements needed to reach an acceptable rate for final offline storage. The full event information, including tracks, is available, but some of the cuts used, as the hadronic/electromagnetic energy fraction and calorimetric isolation, that are based on calorimetric informations only might, in a fully optimized selection chain, be made at an earlier stage.

	Low Luminosity	**High Luminosity**
Single electron	33Hz	75Hz
Double electron	1Hz	4Hz
Single photon	2Hz	7Hz
Double photon	5Hz	8Hz
Total	**43**Hz	**94**Hz

Table 4.8: Electron and photon rates output of the HLT at low and high luminosity.

For electrons this Level-3 steps includes cuts on p_T and on E/p.
Further E_T thresholds, higher than those applied at Level-2.0, are applied to super-clusters of single and double triggers that fail the Level-2.5 pixel matching. The events passing these cuts form the photon stream. The double photon thresholds are asymmetric, chosen to be 5 GeV less than the offline analysis cuts envisaged for the Standard Model $H \rightarrow \gamma\gamma$ [122].
For the low luminosity selection a loose calorimetric isolation has been applied to the photon streams, but no isolation (beyond that of the Level-1 trigger) has been applied to the electron streams. To control the two-photon rate the thresholds can be raised to E_T^1 >40 GeV, $E_T^2 > 25$ GeV (equal to the offline analysis cuts for the $H \rightarrow \gamma\gamma$ channel). This reduces the rate from 11Hz to 5Hz, and has a negligible effect on the signal efficiency. A fully optimized selection would probably involve track isolation on the photon streams (wholly or partly replacing the calorimetric isolation and the raised threshold) and track isolation in the single electron stream. This would reduce the total rate to about 26 Hz, of which only half is background, with the introduction of only a small additional inefficiency. For the high luminosity selection, the isolation of the pixel line (i.e. tracks reconstructed only using the pixel detector) has been required for the electron stream, and full track isolation has been required for the photon streams (no track with $P_T > 2$ GeV/c in a cone of ΔR=0.2).
Table. 4.8 shows the total rates (background plus signal) for single and double-electron/photon trigger. As electron signal sample the process $W \rightarrow e\nu$ has been chosen. The electron efficiency of the HLT selection at low and high luminosity are listed in Tab. 4.9. Events are preselected requiring the generated electrons to be within the ECAL fiducial region. The geometrical acceptance is approximately 60% and is not included in the efficiency. The second and fourth columns list the efficiencies for electrons that have p_T greater than the Level-1 and Level-2 95% efficiency point. The efficiencies at high luminosity

	Low Luminosity		**High Luminosity**	
	All fiducial e	**Fiducial** e **with** p_T **>29 GeV**	**All fiducial** e	**Fiducial** e **with** p_T **>34 GeV**
Level-1	63.2%	87.2%	51.1%	83.2%
Level-2.0	88.8%	99.4%	82.9%	94.1%
Level-2.5	93.1%	94.6%	92.8%	94.1%
Level-3	81%	82%	77%	78%
HLT	**67%**	**77%**	**59%**	**73%**
Bkg Rate (Hz)	**43**		**94**	

Table 4.9: Efficiency for electrons from W decay through the complete selection chain.

	Both photons in fiducial region	**Photons passing offline** p_T **cuts**
Level-1	90.8%	92.3
Level-2.0	98.7%	99.4
Level-2.5	93.4%	99.1
Level-3	92%	92
HLT	**77%**	**83.7%**

Table 4.10: Efficiency for $H \rightarrow \gamma\gamma$ ($M_H = 115 GeV/c^2$) through the complete selection chain, at low luminosity.

are only slightly lower. The main difference comes from the loss due to the additional isolation cuts, typically a 5% loss per object. Table. 4.10 lists the efficiency for $H \rightarrow \gamma\gamma$ for a Higgs with mass $M_H = 115 GeV/c^2$ through the complete selection chain, at low luminosity. As in the previous table, events are preselected requiring that the generated photons fall within the ECAL fiducial region. The geometric acceptance is 65%. The second column shows the efficiency for events where the two generated photons satisfy, in addition, the cuts currently assumed for offline analysis in this channel.

4.2.3 Muon identification

The muon selection for the High Level Trigger proceeds in two steps: firstly, muons are reconstructed in the muon chambers confirming the Level-1 decision and refines the p_T measurement using more precise informations. In a second step the muon trajectories are extrapolated into the tracker volume, what further refines the p_T measurement. After each step, isolation is applied

to the muon candidates, the calorimeters being used after the first step and the tracker after the second.
The muon track reconstruction algorithm used by the High Level Trigger is seeded by the muon candidates found by the Level-1 Global Muon trigger (no more than four), including those candidates that did not necessarily lead to a Level-1 accepted event by the Global trigger. The algorithm uses the reconstructed hits built from the digitized signals in the muon system, and constructs tracks according to the Kalman filter technique. The resulting trajectories are used to validate the Level-1 decision as well as to refine the muon measurement at the Level-2. The basis of the Level-3 muon selection is the addition of the silicon tracker hits to the muon trajectory, thus greatly improving the muon momentum measurement and sharpening the trigger threshold. Isolation criteria can be applied to the muon candidates to provide additional rejection: at Level-2 using the calorimetric energy sum in a cone around the muon, and at Level-3 using the number of pixel tracks in a region around the projected muon trajectory. This suppresses non-prompt muons coming from b, c, π, and K decays.

Muon Reconstruction

Reconstructed track segments from the muon chambers are used for muon identification and selection at Level-2. The state vectors (track position, momentum and direction) associated with the segments found in the innermost chambers are propagated outwards through the iron yoke using the GEANE package [123], which takes into account the muon energy loss in the material, the effect of the multiple scattering, and the non-constant magnetic field in the muon system. The estimate of the momentum from the Level-1 Global Muon trigger is used initially for the track propagation in the magnetic field. The predicted state vector at the next layer is compared with the measured points and the reconstructed track is accordingly updated using a Kalman filter technique. In the barrel chambers, reconstructed track segments are used as measurements in the Kalman filter procedure; in the endcap chambers, where the magnetic field is inhomogeneous, the individual reconstructed hits belonging to the track segments are used. Reconstructed hits from RPC chambers are also included. The procedure is iterated until the outermost station of the muon system is reached, at which point a constrained fit to the track

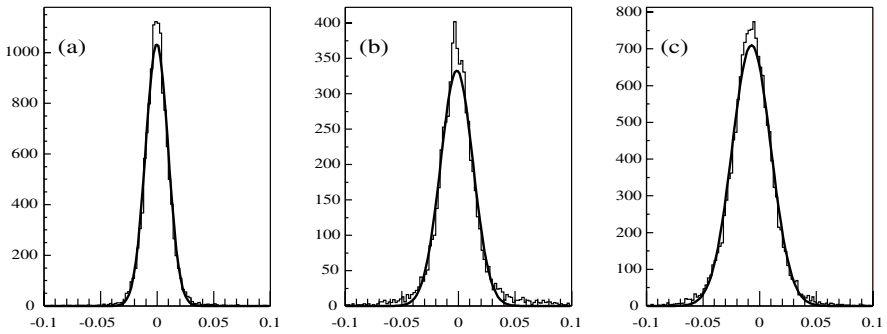

Figure 4.30: Distribution of $(1/p_T^{rec}$ - $1/p_T^{gen})$ / $(1/p_T^{gen})$, where p_T^{gen} and p_T^{rec} are the generated and reconstructed transverse momenta respectively, shown in three pseudorapidity intervals: a) $|\eta|$ <0.8 , b) 0.8< $|\eta|$ <1.3, and c) 1.3< $|\eta|$ <2.1.

parameters, working from the outside in, is performed under the assumption that the muon candidate originated from the interaction region (defined by the beam spot size: $\sigma_{x,y}$ =15 μm and σ_z =5.3 cm). In both the forward and backward propagations just described, a measurement is not added to the muon trajectory if its contribution to the total χ^2 exceeds 25. The resulting track parameters, propagated inward to the collision vertex, are used to reject or accept the event for further Level-3 processing. More details on this muon reconstruction can be found in [124]. The Level-3 muon reconstruction consists of extending the muon trajectories to include hits in the silicon tracker system. Starting from a Level-2 reconstructed muon, the muon trajectory is extrapolated from the innermost muon station to the outer tracker surface, taking into account the muon energy loss in the material and the effect of multiple scattering. As with Level-2, the GEANE package is currently used for the propagation through the iron and calorimeters. Silicon layers that have recorded hits compatible with the muon trajectory are then identified, and a region of interest within them is defined to perform the same regional track reconstruction described in the previous sections.

Fig. 4.30 shows the resolution in transverse momentum determined by the Level-3 reconstruction as expressed by the distribution of the quantity $(1/p_T^{rec}$ - $1/p_T^{gen})$ / $(1/p_T^{gen})$, where p_T^{gen} and p_T^{rec} are the generated and reconstructed transverse momenta. Muons from W decays at high luminosity are used as the reference sample. The distributions are broken up into three pseudorapidity intervals: barrel ($|\eta|$ <0.8), overlap (0.8< $|\eta|$ <1.3) and endcap (1.3< $|\eta|$ <2.1).

In these three regions, the fitted p_T resolutions are 1.0%, 1.4%, and 1.7%, respectively. The improvement over the muon measurement from Level-2 is substantial. The efficiency for the Level-3 tracking algorithm is higher than 98% for $|\eta| < 2.1$

Muon Isolation

The integrated rate of muons at LHC is dominated by muons from b, c, K, and ϕ decays. These muons are generally accompanied by other nearby particles, so they can be suppressed by isolation cuts.
Three isolation techniques have been studied. The first (*calorimeter isolation*) is based on the standard technique of summing the calorimeter energy in a cone around the muon, and can be used with the standalone muon reconstruction at Level-2. However, as it is based on the calorimeter, this technique becomes less effective at high luminosity as more and more pile-up is included in the sum. The second technique (*pixel isolation*) is based on the partial reconstruction of tracks in the silicon pixel detector; in this case, isolation is determined on the basis of the sum of the transverse momenta of the tracks in a cone around the muon. This method, which can be applied when tracker information is included at Level-3 (as for the τ-jet isolation algorithm), is less sensitive to pile-up, as only tracks originating from the same collision vertex are considered. However, it requires the reconstruction of three pixel hits out of the three layers of the pixel detector. For this reason it is sensitive to inefficiencies and may not be useful in staging scenarios where only two pixel layers are installed. The third technique, tracker isolation, uses full tracks reconstructed regionally. This method is more robust than the pixel isolation, but is more time consuming especially at high luminosity.
For all three techniques, cones are defined by the condition $\Delta R < \Delta R_{max}$. The $\sum E_T$ deposited in the cone in the case of calorimeter isolation or the $\sum p_T$ of tracks in the cone in the case of pixel and tracker isolation are computed after subtracting the muon contribution (veto value) and compared with a predefined threshold. For each algorithm, both the cone size and the thresholds are chosen by maximising the rejection for a reference background sample while keeping the efficiency for a reference signal sample above a given nominal value (*nominal efficiency*). The threshold is determined independently in 52 bins in η, in order to guarantee a flat signal efficiency as a function of η.

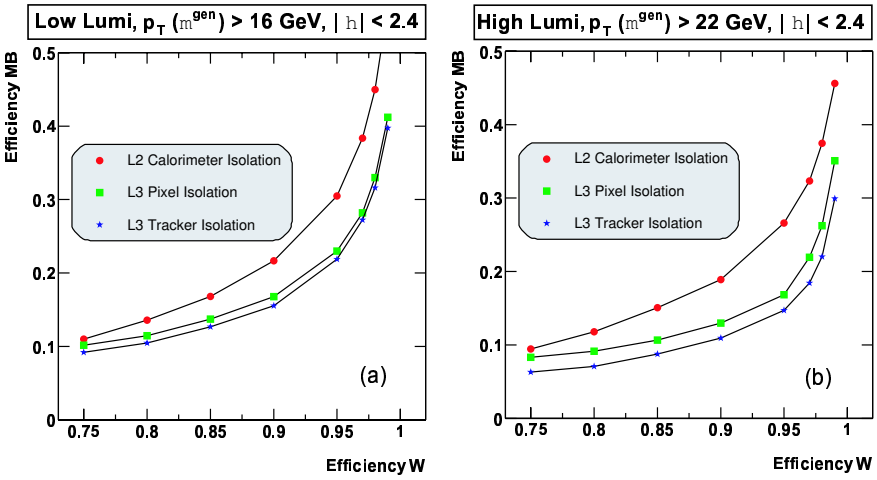

Figure 4.31: Efficiency of the three isolation algorithms on the reference background muons as a function of efficiency for the reference signal muons at (a) low and (b) high luminosity.

The Level-2 background rate is dominated, for any p_T threshold, by the feed-through of very low p_T muons, that cannot be rejected by the isolation algorithms but should be rejected by the refined p_T threshold at Level-3. So the isolation criteria becomes important on high p_T muons where the contamination of the p_T spectrum from the feed-through of low-p_T muons is smaller. To study the algorithmic efficiency of the isolation criteria on these high p_T muons a background sample of minimum-bias events containing only muons with p_T above 22 GeV/c (16 GeV/c) for high (low) luminosity is used. The direct $W \rightarrow \mu\nu$ decay is used as reference signal since it contains well isolated muons with adequate p_T spectrum. The result of the optimisation procedure is that, for any predefined nominal efficiency value, a cone size is chosen with thresholds defined in bins of pseudorapidity. For all three isolation techniques, typical values of the optimal cone size ΔR_{max} vary from 0.2 to 0.3. A detailed description can be found in [125].

Fig. 4.31 shows the efficiency for reference background muons versus the efficiency for reference signal muons, at low luminosity with p_T^{gen} >16 GeV/c and at high luminosity with p_T^{gen} >22 GeV/c. The background rejection can be adjusted by choosing different efficiencies for the reference signal.

The efficiency turn-on curves as a function of the generated p_T for several different p_T thresholds are shown in Fig. 4.32. The efficiency shown is the cumulative Level-1 through Level-3 efficiency. The threshold at each trigger

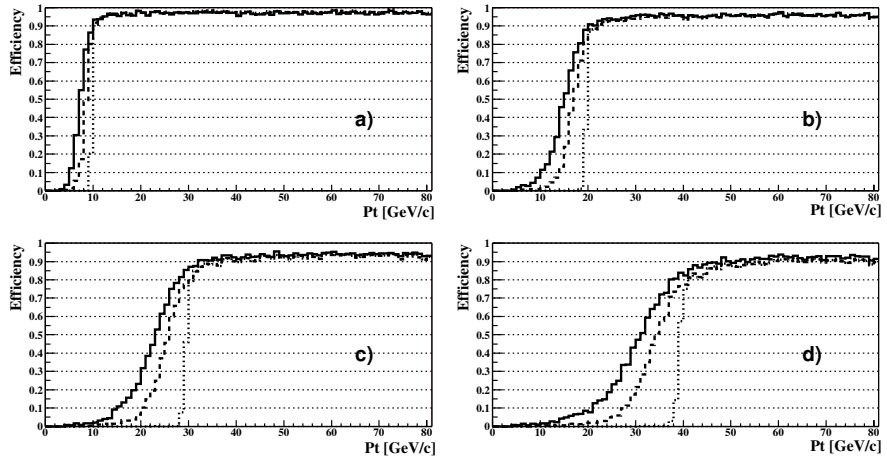

Figure 4.32: Cumulative efficiency for single muons to pass the Level-1 (solid), Level-2 (dashed), and Level-3 (dotted) triggers as a function of the generated p_T for several trigger thresholds: a) p_T >10GeV/c, b) p_T > 20 GeV/c, c) p_T > 30 GeV/c, and d) p_T >40 GeV/c.

level is defined at 90% efficiency (relative to the plateau efficiency). It can be seen how the improved p_T resolution at each successive level sharpens the turn-on curve. The efficiency at Level-3 for high p_T muons varies from 97% (no threshold) to 90% (p_T >40 GeV/c). Additionally, for the HLT, Level-2 muon candidates must satisfy the calorimeter isolation criteria at the 97% efficiency point for the reference signal. At Level-3, candidates must satisfy either the tracker or pixel isolation criteria both at the 97% efficiency point for the reference signal. The selection described above can be used to trigger either events with single muons or on events with two muons in the final state. The selection criteria for each muon in an inclusive di-muon trigger are the same as those for the single muon trigger, except that the isolation criteria have to be satisfied by one of the two muons. In addition, at Level-3, both muons are required to have originated from the same vertex in z to within 5 mm (to reduce triggers from muons in separate pp collisions), whereas di-muons that have $\Delta\phi$ <0.05, $\Delta\eta$ <0.01, and Δp_T < 0.1 GeV/c are rejected in order to remove ghost tracks. The combined single and di-muon trigger rates are shown in Fig. 4.33 as a function of the symmetric di-muon p_T threshold and the single muon p_T threshold for low and high luminosity. A possible working point at low luminosity for a target rate of 30 Hz is a single muon p_T threshold of 19 GeV/c and a symmetric di-muon threshold of 7 GeV/c. Possible working points at high luminosity are

a single muon p_T threshold of 38 GeV/c and a symmetric di-muon threshold of 12 GeV/c for a combined rate of 33 Hz, or a single muon p_T threshold of 31 GeV/c and a symmetric di-muon threshold of 10 GeV/c for a combined rate of about 55 Hz.

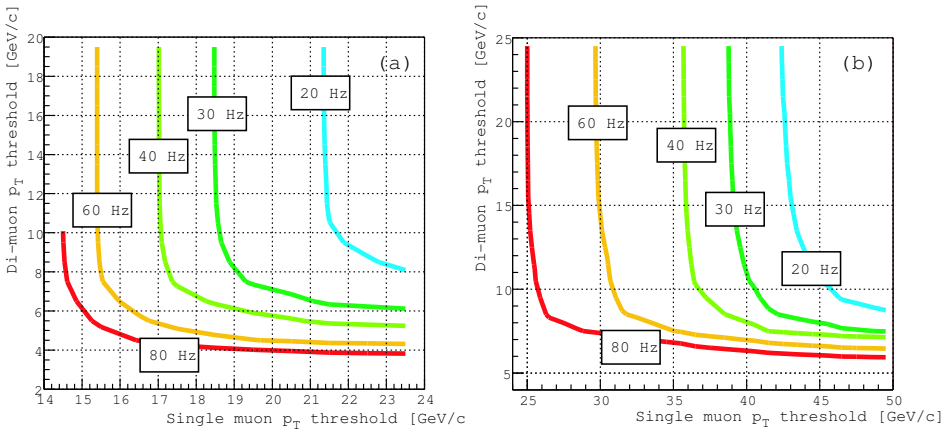

Figure 4.33: Combined single and di-muon trigger rates as a function of both the symmetric di-muon p_T threshold and the single muon p_T threshold for (a) low and (b) high luminosity.

4.2.4 Combined trigger

To achieve the best performance on different signal events, other trigger selections have been studied combining two different trigger streams together. For example μ+τ-jet and e+τ-jet triggers are used to select events with two τ leptons, one of them decaying semileptonically and the other hadronically. The HLT selections are the same described in the previous sections, but in some cases the thresholds at Level-2 can be lowered. More information are described in the next chapter where these combined triggers have been used to trigger on the channel: $\phi \rightarrow \mathrm{hh} \rightarrow \tau\tau\mathrm{bb}$.

Chapter 5

Analysis

As already stated in the first chapter of this thesis, the existence of a scalar particle, the radion, would be a proof of the presence of extra dimensions. The radion search can be performed in the same final states used for the discovery of the Standard Model Higgs boson. The mixing among the two scalars affects their cross section and branching ratios and in some (catastrophic) scenario the Higgs discovery at LHC could be missed due to this mixing [126]. There are some regions of parameters space in which the significance for a Higgs bosons of about 120 GeV/c^2 mass decreases below 5 σ, with respect to the SM previsions. In this regions it would be possible to detect a radion of about 300 GeV/c^2 mass, but further measurements would be necessary to claim the discovery of the extra dimensions. In this optics it becomes important to search for new interesting discovery channels. May be the most interesting one is the production of a Higgs pair via a radion resonance: gg $\rightarrow \phi \rightarrow$ hh, which would allow the study of the two scalar particles at the same time, and so all the ambiguities would be removed.
The aim of this thesis is to understand if and how much CMS will be sensitive to this scenario. Having this idea in mind the example of a Higgs mass of 125 GeV, and of a radion mass of 300 GeV with three different final states has been considered:

- gg $\rightarrow \phi \rightarrow$ hh $\rightarrow \tau\tau$ bb
- gg $\rightarrow \phi \rightarrow$ hh $\rightarrow \gamma\gamma$ bb
- gg $\rightarrow \phi \rightarrow$ hh $\rightarrow$ bb bb

The candidate has analyzed in detail the first channel, when one τ decays semileptonically and the second hadronically. Then the results of the other two analyses (performed by Alexandre Nikitenko and Livio Fanò) have been considered to optimize the signal significance for this scenario.
The most important backgrounds for the $\tau\tau$bb final state are: $t\bar{t}$ events (with one W decaying leptonically and the other decaying into jets or τ lepton), Z+jets, Z+bb and W+jets. The most dangerous background is the $t\bar{t}$ sample with about 7.5×10^6 expected events after 30 fb^{-1} (see Tab. 5.3 for more details). As shown in the following section, the Trigger and off-line selection can reduce this number of events by several orders of magnitude.
Another possible background source is the associate production of a Higgs boson with a pair of jets or a vector boson (W or Z). The final states are similar to the signal and even if there are no radion resonances in these processes they may spoil the signal detection. The following processes are the most similar to the signal:

- gg, qq$\rightarrow$ hbb $\rightarrow \tau\tau +$ bb $\rightarrow$ l $+ \nu + \tau$jet + bb,
- qq$\rightarrow$ hqq $\rightarrow \tau\tau +$ qq $\rightarrow$ l $+ \nu + \tau$jet + qq,
- qq$\rightarrow$ hZ $\rightarrow$ bb $+ \tau\tau \rightarrow$ bb + l $+ \nu + \tau$jet,
- qq$\rightarrow$ hW $\rightarrow \tau\tau +$ qq $\rightarrow$ l $+ \nu + \tau$jet + qq.

The cross section times branching ratios for these processes are similar to cross section in the Standard Model and are shown in Tab. 5.1. For more details see Section 5.2.1. The gg $\rightarrow \phi \rightarrow$ hh $\rightarrow \tau\tau$bb $\rightarrow$ l $+ \tau$jet $+ \nu$+bb maximal cross

process	σ **(pb)**	$\sigma \times BR$ **(pb)**
gg$\rightarrow$ hbb $\rightarrow \tau\tau +$ bb $\rightarrow$ l $+ \nu + \tau$jet + bb	~ 0.8	0.03
qq$\rightarrow$ hqq $\rightarrow \tau\tau +$ qq $\rightarrow$ l $+ \nu + \tau$jet + qq	$\sim$350.8	1.1
qq$\rightarrow$ hZ $\rightarrow$ bb $+ \tau\tau \rightarrow$ bb + l $+ \nu + \tau$jet	~ 1	0.01
qq$\rightarrow$ hW $\rightarrow \tau\tau +$ qq $\rightarrow$ l $+ \nu + \tau$jet + qq	3	0.07

Table 5.1: Cross section times branching ratios (in pb) for the associate production of Higgs boson with jets or vector boson (Z or W). See text for more details.

section times branching ratios is about 0.96 pb. Only the process qq$\rightarrow$ $h$qq has a comparable cross section, but the off-line analysis would suppress this

reducible background as it does for the Z+jets one. In conclusion these background rates are negligible with respect to the signal one and they will not be considered anylonger in the following analysis.
As already stated above, if Extra Dimensions exist, the Higgs boson discovery in the "standard channels" (i.e. the channels that, accordingly to the Standard Model prediction, have the highest probability to see Higgs events) could be missed. To take into account this possibility, in the $\tau\tau$bb final state two different analyses have been performed: in the first, the Higgs boson has not yet been discovered, and its mass is unknown; in the second analysis the assumption that the Higgs boson has already been discovered is considered and a kinematical fit has been performed using a constraint on the Higgs boson mass.
The analysis has been performed assuming CMS standard running condition at the LHC start. The muon chambers trigger read-out has a limited acceptance of $|\eta|$ <2.1, while the standard pixel scenario (3 layers and 2 disks) has been assumed. The low luminosity period ($\mathcal{L} = 2 \times 10^{33}\text{cms}^{-2}\text{s}^{-1}$), equivalent to an integrated luminosity of 30 fb^{-1} has been considered.
A similar study has been performed by the ATLAS Collaboration, few years ago [127]. The work presented in this thesis considers a more reliable simulation of the signal events and takes into account some dangerous background which were not forseen in the previous ATLAS study. Moreover for the first time the four b jets final states has been fully studied.
In order to extract any signal from the huge multijet background it is fundamental to have tools to tag jets coming from the fragmentation of a b quark or from a τ hadronic decay. For what concerns τ leptons, the selection described in the High Level Trigger analysis (namely the L2Tk isolation algorithm, see section 4.2.1 for more details) has been used. The reconstructed tracks are used to identify jets coming from the fragmentation of a b quark or to identify hadronic decay of τ lepton. The use of these tagging algorithm allows the rejection of background events. The τ tagging performance has been presented in Chapter 4, while in the next section it is described how the reconstructed track parameters can be used to tag b jets.
In the following sections the b-tagging tool used in this analysis is described.

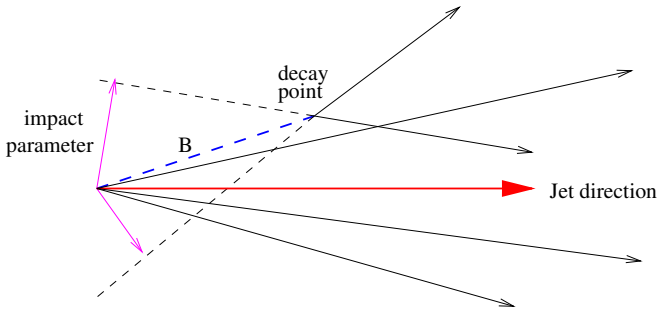

Figure 5.1: Schematic view of a B hadron decay.

5.1 b-tagging tools

The identification of b-quark decays allows the selection of processes in which b quarks are produced in heavy particle decays. Inclusive b-tagging has played a crucial role in past experiments: examples are the measurement of the Z$\rightarrow$ b$\overline{\text{b}}$ branching ratio at LEP and the top quark discovery with t$\rightarrow$ Wb at the Tevatron. At LHC b-tagging will play a crucial role for the Higgs discovery.
The identification of hadron jets originating from b quarks relies on the properties of B decays. B hadrons have a lifetime $\tau_B \sim 1.56$ ps, which corresponds to a $c\tau_B \sim 470$ μm, and produce on average 5 charged particles per decay.
The lifetime information can be exploited in different ways. In the analysis presented in this thesis the method is based on tracks with a large impact parameter. As shown in Fig. 5.1, tracks from B decays have a large impact parameter because they originate from a displaced vertex, while the impact parameter of tracks coming from the primary vertex is compatible with the tracking resolution. The power of this methods is limited both by inefficiency in track reconstruction and by the experimental resolution of track parameters. The mistagging rate is due to secondary interactions and decays of long-lived particles. Secondary interactions with the tracker material can produce secondary vertices and thus tracks with a large impact parameter. Long-lived particles, such as K^0_S, Λ^0, and charm can provide real decay vertices and therefore constitute a physical irreducible background. This is particularly true for charmed particles.

b-tagging based on the Track Impact Parameter

The track impact parameter can be computed either in the plane transverse to the beam axis (*transverse impact parameter*) or in three dimensions (three-

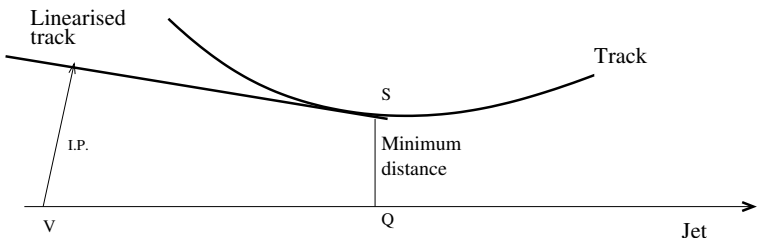

Figure 5.2: Three-dimensional impact parameter.

dimensional impact parameter). Due to the small size of the beam in the transverse plane at LHC, the transverse impact parameter is weakly affected by the uncertainty on the primary vertex position. In the case of the three-dimensional impact parameter, a greater amount of information is exploited, but the error is larger due to the uncertainty on the z coordinate of the primary vertex.

In both cases, the computation is performed starting from the trajectory parameters at the innermost measurement point. Figure 5.2 shows the three-dimensional impact parameter, where V identifies the primary vertex position. The VQ segment is called the *decay length* and approximates the flight path of the B hadron. The impact parameter is signed as positive (or negative) if the decay occurs downstream (or upstream) the jet direction, i.e. if the scalar product between the jet direction and the impact parameter direction (i.e. the arrow labeled with 'i.p.' in Fig. 5.2) is positive (or negative). Since the jet direction approximates the flight direction of the B hadron, the tracks from a B decay have positive impact parameter. Effects due to badly measured track parameters, badly reconstructed jet directions or fake primary vertices can flip the sign of the impact parameter. To take into account the experimental resolution, the track impact parameter significance, i.e. the ratio between the track impact parameter and its error is introduced. Figure 5.3 shows the distribution of the transverse impact parameter significance for b and u jets with $E_T = 100$ GeV and $|\eta| < 0.7$. Tracks from u jets are more or less distributed according to a Gaussian function with center in 0 and width 1 because they come from the primary vertex and thus their impact parameter is compatible with zero within the experimental resolution. Tracks from b jets show an asymmetric distribution at positive values, as a result of the measurable lifetime.

The simplest way to use the impact parameter to tag a b jet is to require

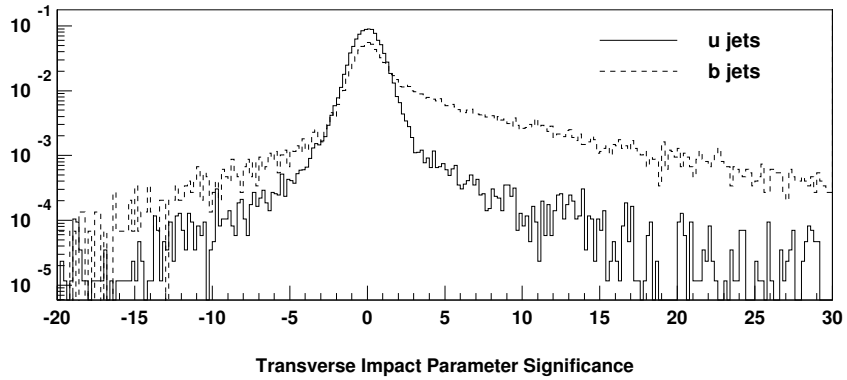

Figure 5.3: Significance distribition for the two-dimensional impact parameter.

a minimum number of "good quality tracks" with an impact parameter significance exceeding a given threshold [128]. Different performances can be achieved by tuning the required number of tracks and by choosing an appropriate threshold on the significance: the optimal choice of these parameters depends on the type of physics process under study. The main advantage of this method is its simplicity: it only relies on the selection of "good quality tracks" and a cut on impact parameter significance. "Good quality tracks" means p_T >1 GeV and at least 8 associated hits, with 3 of them belonging to the pixel detector. An upper threshold on the transverse impact parameter is also used (2 mm) to avoid K decays and nuclear interaction. To evaluate the performance, several samples of di-jet events are used. In these events, the primary interaction is generated with PYTHIA 6.152 and the detector simulation is performed with CMSIM 122. Pile-up is not included in these studies. Jets are produced in three different η bins, $|\eta| < 0.7$, $1.2 < |\eta| < 1.6$ and $2.0 < |\eta| < 2.4$, corresponding to the barrel region, the region of overlap between barrel and end-caps and the very forward region. Different E_T bins, corresponding to $E_T = 50$, 100 and 200 GeV, are taken into account: in $E_T =$ 50 GeV jets, the track p_T spectrum is softer, so the performance is limited by the multiple scattering, while in $E_T = 100$ GeV jets the performance is degraded by the very high particle density. Jet momenta are provided by the PYTHIA's PYCELL routine. This routine performs a coarse simulation of the calorimeter response starting from the stable particle information. The same resolution and segmentation of the CMS calorimeter are applied. A simple clustering algorithm is applied to compute the jet momenta. QCD samples

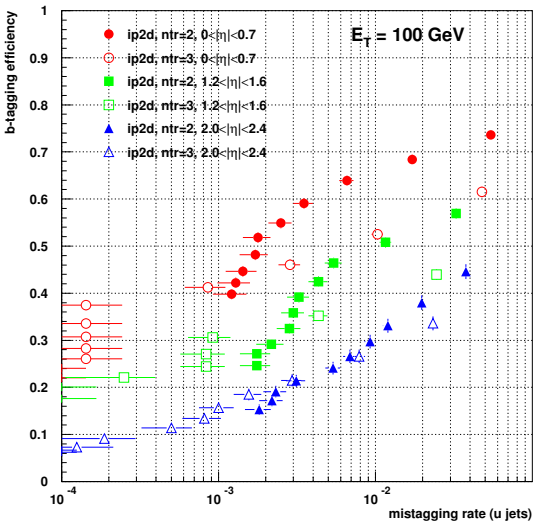

Figure 5.4: b-tagging efficiency using the two-dimensional impact parameter.

with 50< p_T <170 GeV have been generated with PYTHIA 6.125. For the event reconstruction the ORCA packege has been used.

The b-tagging performance is analysed in terms of the b-tagging efficiency (ϵ_b) and mistagging rate (ϵ_u, ϵ_c). Both variables are related to the single jet: the b-tagging efficiency is the fraction of jets tagged as b in bb samples, while the mistagging rate is the fraction of non b jets tagged as b in the $u\overline{u}$ or $c\overline{c}$ samples. The mistagging rate is computed for uds jets, c jets and gluon jets separately. Each point in the ϵ_b versus ϵ_u plane is defined by a set of parameter cuts in the algorithm. The optimal values of the parameters depend on the specific physics process: a typical value required for the mistagging rate is around 10^{-2}.

Figure 5.4 shows the performance of the track counting algorithm based on the two-dimensional impact parameter in different η regions and for jets of E_T = 100 GeV. Each point corresponds to a different cut on impact parameter significance (ranging between 0.5 and 4.5) with the request that the minimum number of tracks fulfilling the cut (ntr) be 2.

These analysis confirm that it is possible to achieve a b-tagging efficiency of about 50% with a mistagging rate of 10% for c jets and 1% for light quark (gluon) jets as shown in Tab. 5.2.

	b	c	uds	gluon
Efficiency	0.5	0.1	0.01	0.01

Table 5.2: b-tagging and mistagging efficiency computed with the impact parameter method using 2 tracks with significance greater than 2.

5.2 $\tau\tau$bb $\rightarrow$ l + τ jet $+\nu's+$ bb final state

In the following section the analysis, performed by the candidate, of the $\tau\tau$bb final state is presented. The main background processes, the trigger and the off-line selections are described in details. At the end of the section the results are summarized in a 5 sigma discovery plot, in the (λ,ξ) plane, which consider statistical and systematical background uncertainties.
Two different analyses have been performed: in the first one the Higgs boson has not yet been discovered, and its mass is unknown; in the second analysis the assumption that the Higgs boson has already been discovered is considered and a kinematical fit has been performed using a constraint on the Higgs boson mass.
The $\tau\tau$ bb final state offers the possibility to test the CMS reconstruction software for almost all the physics objects used in standard analyis: muons, electrons, τ and b jets. Indeed it has been usefull to demonstrate that for very low energy τ jet (E_T around 50 GeV) a High Level Trigger selection slightly different from the one presented in the past chapters must be adopted, in order to increase the signal efficiency to an acceptable value.

5.2.1 Monte Carlo Samples

Signal and background samples (apart from Zbb events that have been simulated using CompHEP [129]) have been generated with PYTHIA 6.158. Signal events have been processed with CMSIM 125 and ORCA 6.2.0 to have full simulation and reconstruction. Pile-Up events have been added in agreement with the low luminosity rate.
The background samples have been processed with the CMSJET package [130], that offers a fast simulation of the detector.
For what concerns τ-tagging, b-tagging and High Level Trigger selection, the efficiency computed with fully simulated samples (the same used for the vari-

ous CMS Technical Reports) have been applied to the fast simulation, in order to have reliable estimates of the expected background rate.

Background Samples

Background events have one isolated lepton, neutrinos and at least 3 jets in the final states. The background processes considered are shown in Tab. 5.3. Cross sections times branching ratios and number of expected events for 30 fb^{-1} are also shown in the same table. The k-factors used to evaluate NLO cross sections from the LO ones are taken from [131] and are shown in Tab. 5.4. The errors on the k-factors, also shown in Tab. 5.4, range from about 5% to about 15%. These errors have been considered as the systematical uncertainties on the cross sections.
The most dangerous process is $t\bar{t}$ production, mainly due to the presence of the two b jets and the lepton coming from one W. The other W may decay either in hadrons (tt_{had} sample) or into a τ lepton that then decays hadronically (tt_{tau}). The following branching ratios have been used to computed the final cross sections and expected number of events:

- $t\bar{t} \rightarrow Wb + W\bar{b} \rightarrow l + \nu +$ jets $+ b\bar{b}$: the final state is represented by a lepton, two b-jets and two generic jets one of wich should be mistagged as τ jet. The BR(W $\rightarrow$ e/μ) is 22%, while the BR(W$\rightarrow$jets) is 68%;

- $t\bar{t} \rightarrow Wb + W\bar{b} \rightarrow l + \nu + \tau + b\bar{b} \rightarrow l + \nu + \tau$jet $+ b\bar{b}$: The final state is represented by a lepton, two b-jets and a τ jet coming from the decay of the τ lepton coming from the W. The BR(W $\rightarrow$ e/μ) is 22%, while the BR(W$\rightarrow \tau \rightarrow \tau+\nu$) is about 7%, while the probability for $\tau\tau \rightarrow$ l+ν+τjet is about 46%;

- Zbb $\rightarrow \tau\tau +$ bb $\rightarrow$ l + $\nu + \tau$jet $+ b\bar{b}$: the final state consist of a lepton and a τ jet coming from the Z decay into τ leptons and a pair of b jet produced in association with the Z. The BR(Z$\rightarrow \tau\tau$) is about 3%, while the probability for $\tau\tau \rightarrow$ l + $\nu + \tau$jet is about 46%;

- Z + jets $\rightarrow \tau\tau +$ jets $\rightarrow$ l + $\nu + \tau$jet+jets: in this sample the jets produced in association with the Z can be both light and b jets.

bkg Samples	σ **(pb)**	$\sigma \times BR$ **(pb)**	**N. of events**
$t\bar{t} \rightarrow Wb + W\bar{b} \rightarrow l + \nu + jets + b\bar{b}$ (tt_{had})	825	245	7.3×10^6
$t\bar{t} \rightarrow Wb + W\bar{b} \rightarrow l + \nu + \tau jet + b\bar{b}$ (tt_{tau})	825	27	8×10^5
$Zb\bar{b} \rightarrow \tau\tau + b\bar{b} \rightarrow l + \nu + \tau jet + b\bar{b}$	525	8	2.4×10^5
$Z + jets \rightarrow \tau\tau + jets \rightarrow l + \nu + \tau jet + jets$ ($\hat{p_T} > 20$)	23300	355	10.6×10^6
$W + jets \rightarrow l + \nu + jets$ ($\hat{p_T} > 80$)	4100	900	27×10^6

Table 5.3: Cross section (NLO), branching ratios and expected number of events, after 30 fb^{-1}, for the main background samples. See text for more details.

bkg Samples	**k-factor**	k_{min}**-factor**	k_{max}**-factor**
$t\bar{t}$	1.35	1.28	1.45
$Zb\bar{b}$	1.49	1.3	1.7
Z + jets	1.16	1.13	1.19
W + jets	1.13	1.10	1.17

Table 5.4: Error on k-factors used in this analysis for the NLO cross sections. k_{min} and k_{max} show the uncertainties on the central value.

The Z+jets sample has been generated with a $\hat{p_T}$ cut of 20 GeV for the two jets, in order to save statisitcs and not to produce events with low energy jets, that would not have passed the analysis selection. For the $W + jets$ a $\hat{p_T}$ cut of 80 GeV is used to increase the rate of events with at least three jets in the final state. The two top sample, are the most important ones. We have not simulated the case in which both Ws decay into τs (tt_{2tau} sample) but its contribution has been estimated to be about about 1/3 of the tt_{tau} sample, that means a 10% of the total number of background events. The contamination from events with jets which are neither τ nor b can be reduced appling τ and b-tagging algorithms as described in the previous sections.

Signal Sample

At present there is no generation package to deal with the radion processes. In order to generate the signal sample, the MSSM process: gg$\rightarrow$ H $\rightarrow$hh has been used. This process provides the final state we are interested in, while the cross section is obtained with the following formula:

$$\sigma(gg \rightarrow \phi) = \sigma_{SM}(gg \rightarrow h)\frac{\Gamma(\phi) \cdot BR(\phi \rightarrow gg)}{\Gamma_{SM}(h) \cdot BR_{SM}(h \rightarrow gg)}, \qquad (5.1)$$

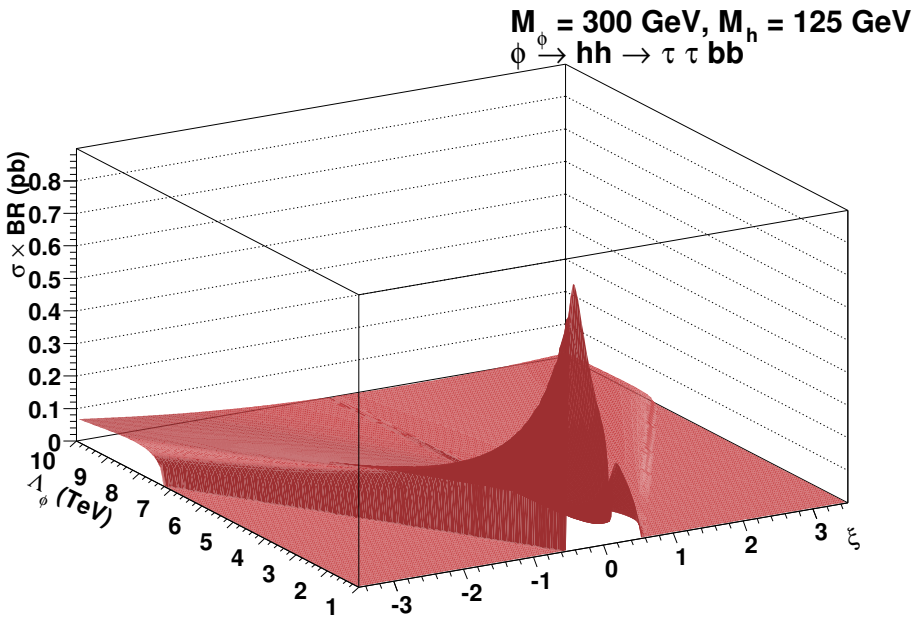

Figure 5.5: Cross section times branching ratios for the process: gg $\rightarrow$ ϕ $\rightarrow$ hh $\rightarrow$ $\tau\tau$bb, with one τ decaying semileptonically and the other hadronically, as a function of ξ and Λ_ϕ. The radion mass is fixed at 300 GeV while Higgs mass is 125 GeV.

where $\Gamma(\phi)$ ($\Gamma_{\rm SM}$(h)) is the total width of the radion (SM Higgs) and $BR(\phi \rightarrow$ gg) ($BR_{\rm SM}(h \rightarrow$ gg)) is the ϕ (SM Higgs) branching ratio into gluons. The codes by Spira and Dominici [46] have been used to get the next to leading order values for the $\sigma_{\rm SM}$ and the other widths.

As discussed in the first chapter, the radion cross section and branching ratios, once chosen the Higgs and the radion masses, depend on two parameter: ξ and Λ_ϕ. Fig. 5.5 shows the cross section times branching ratio for a radion mass of 300 GeV and a Higgs mass of 125 GeV. The highest cross section for the process gg $\rightarrow$ ϕ is obtained with ξ= -0.35 and Λ_ϕ=1 TeV, and it is around 100 pb, while the branching ratio $\phi \rightarrow$ hh is around 26%, the branching ratio for the Higgs boson to a pair of τ lepton is about 7% and the probability for $\tau\tau \rightarrow$ l + ν + τjet is about 46%. The overall $\sigma\times$BR is 0.96 pb. With these numbers about 29,000 events are expected after $30 fb^{-1}$. The following section describes the trigger selection used in the analysis.

Trigger	**Threshold (GeV)**
Inlcusive isolated electron/photon	29
Inclusive isolated muon	14
Single tau jet trigger	86
Electron*Jet	21*45

Table 5.5: Level-1 trigger table at low luminosity. Thresholds correspond to values with 95% efficiency, see the trigger chapter for more details.

5.2.2 Trigger

This channel is a perfect candidate to test the CMS combined trigger. The lepton and the τ jet have too low energy to efficiently pass the Level-1 electron or Tau trigger which require an electron with energy greater than 29 GeV or a τ jet with energy greater than 86 GeV. The combined *electron* + τ trigger has lower thresholds (21 GeV for the electron and 45 GeV for the τ jet), as shown in Tab. 5.5, and it is the only trigger which can be efficiently used in this analysis. The inclusive muon threshold is low enough (14 GeV) to allow good efficiency, however to increase background rejection a Level-1 τ jet with E_T >35 GeV is required. All the thresholds quoted refer to values with 95% efficiency, i.e. the threshold for which a jet, or a particle, with that energy at generator-level, has the 95% probability to pass the selection (see the trigger chapter for more details). The trigger selection starts with the lepton and τ identification at Level-1, then High Level muon or electron trigger are applied. If the event is accepted the High Level τ trigger is performed. The Level-2 tracker isolation (L2Tk) would then be applied to the first, i.e. the most energetic, τ jet in the τ jet list provided by Level-1 selection. The purity of the Level-1 τ trigger for low energy τ jets of $E_T < 60$ GeV is not high and depends on the event topology: it may happen that the real τ jet is not correctly identified by the algorithm. From Monte Carlo studies it has been understood that only in $\sim 30\%$ of the events the Level-1 Tau trigger selects the real τ jet, while in the other 70% of the cases the τ jet is reconstructed in the Central jet list. In order to increase the signal efficiency the L2Tk algorithm has been applied to the three most energetic jets, independently of if they are in the Central or in the τ list, so that the Level-1 τ trigger inefficiency can be recovered. Fig. 5.6 shows a sketch of how the algorithm has been used in this analysis. As soon as one out of the three jets is tagged as a τ jet, the

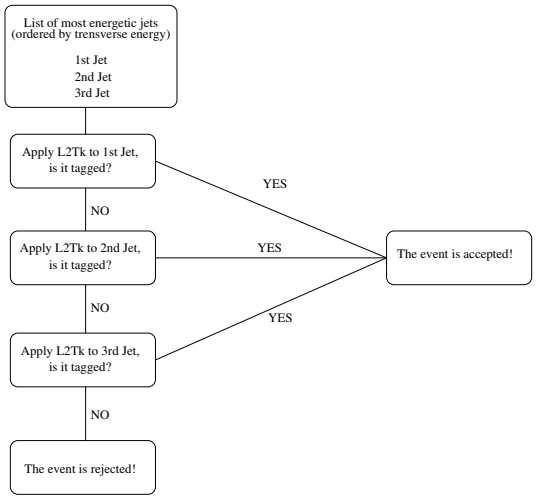

Figure 5.6: Sketch of how the L2Tk algorithm is applied for the High Level Trigger selection.

Samples	**L1 e*τ (%)**	**L1 μ*τ (%)**	**HLT e*τ (%)**	**HLT μ*τ (%)**	**Total (%)**
$\phi \rightarrow \tau\tau$bb	44.3 $\pm$ 0.7	54.8 $\pm$ 0.7	7.0 $\pm$ 0.3	5.9 $\pm$ 0.3	**6 $\pm$ 0.2**
tt_{had}	28.7 $\pm$ 0.2	32.1 $\pm$ 0.2	0.35 $\pm$ 0.02	0.49 $\pm$ 0.02	**0.57 $\pm$ 0.02**
tt_{tau}	22.6 $\pm$ 0.2	42.5 $\pm$ 0.2	1.4 $\pm$ 0.2	2.8 $\pm$ 0.2	**3.1 $\pm$ 0.2**
Zbb	5.6 $\pm$ 0.2	10.7 $\pm$ 0.2	2.0 $\pm$ 0.2	3.1 $\pm$ 0.2	**1.4 $\pm$ 0.2**
Z+jets	2.6 $\pm$ 0.2	4.6 $\pm$ 0.2	0.55 $\pm$ 0.02	0.74 $\pm$ 0.02	**0.35 $\pm$ 0.02**
W+jets	22.8 $\pm$ 0.2	23.1 $\pm$ 0.2	0.22 $\pm$ 0.02	0.31 $\pm$ 0.02	**0.039 $\pm$ 0.002**

Table 5.6: Trigger efficiency for the signal and bacground samples.

algorithm is stopped and the event is accepted, otherwise (no jet is tagged) the event is rejected. Tab. 5.6 shows signal and background efficiency for the trigger selection. The efficiencies computed with QCD and single lepton fully simulated samples have been used for the fast simulation package. The Level-1 τ identification has a mistagging efficiency which varies from 66% to 85% (depending on the jet energy), while the efficiency for High Level Trigger lepton isolation is around 35% for electrons and 50% for muons (including geometrical acceptance).

In order to reduce the background rate the following parameters for the L2Tk algorithm have been used: Isolation Cone = 0.4, Signal Cone = 0.07, p_T^{LT} >10 GeV and only isolated events with 1 or 3 reconstructed tracks in the Signal Cone have been accepted. Sometimes it may happen that the identified electron is also found as a jet in the jet list. In order to avoid a mistagging of

the electron as a τ jet, we required the ΔR between the electron and the τ jet ($\Delta\mathrm{R}_{\mathrm{l}\tau}$) to be greater than 0.1.
The isolation efficiency for fake τ jet, with this set of parameters, is around 1.8%.
The trigger efficiencies for the various signal and background samples are shown in Tab. 5.6. The first two columns show the efficiencies for the Level-1 trigger (electron+τ and muon+τ), the second two show the efficiencies for the HLT selection. The last column gives the total trigger efficiency. From these efficiencies it is clear how the HLT selection is important to reject events without real τ jets ($\mathrm{tt}_{\mathrm{had}}$ and W+jets samples).
In the next section the details of the off-line analysis are presented.

5.2.3 Off-line analysis

After the trigger selection almost all the physics objects needed for the analysis are provided: leptons and τ jets. The next step is to recover the momenta of the neutrinos to reconstruct the τ-τ invariant mass. Then the b jets coming from the other Higgs boson will be considered. Dealing with b jets the following definitions will be used:

- b jet: jet coming from the fragmentation of a b-quark. They are accessible only via Monte Carlo information;
- b-tagged jet: jet tagged as a b jet, even if it comes from the fragmentation of a lighter quark.

τ jets invariant mass

In order to reconstruct the τ jets invariant mass, it is fundamental to identify the neutrinos and to reconstruct their momenta. With the CMS calorimeters it is possible to measure the total missing energy in the event. However if there is more than one neutrino in the final state it is impossible, without any further information, to separate the contribution of the different neutrinos.
In the Higgs decay the τ's are boosted in such a way that the *collinear approximation* can be used. The angle between the neutrino flight direction and the τ jet, or lepton, flight direction is so small that the neutrino and the τ jet, can be considered collinear. For example we can take the τ jet flight direction

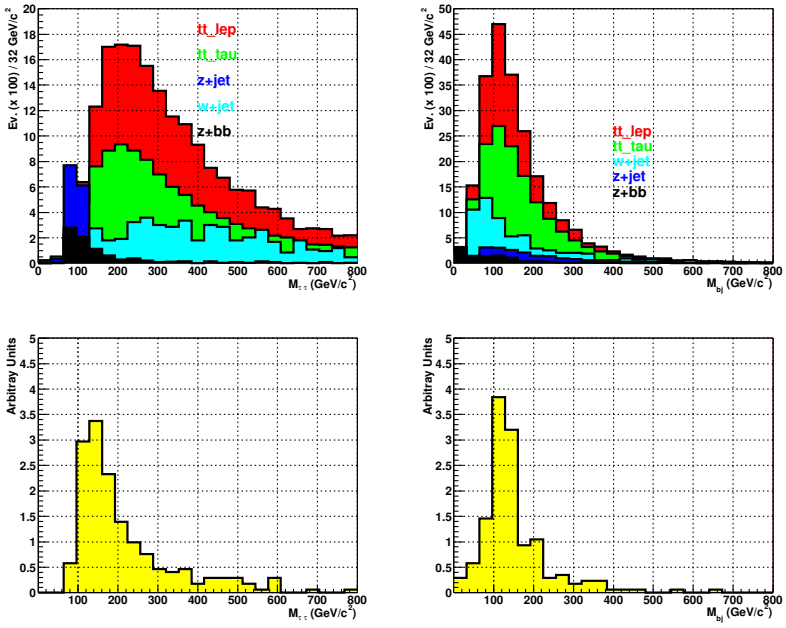

Figure 5.7: Invariant mass distributions of the τ and b-tagged jets for the background (upper plots). Invariant mass distributions of the τ and b-tagged jets for the signal (bottom plots).

as the flight direction of the neutrino. We still miss the information about the energy of the neutrino. It can be recovered using the total transverse missing energy. Projecting the vector representing the flow of the transverse missing energy onto the neutrino flight direction (in the r, ϕ plane) is thus possible to separate the contributions of the energy of the neutrinos from the two different τ decays. At the end we have both the direction and the energy of the neutrinos and we can reconstruct the momenta of the two τ leptons before their decay. Once we have the momentum of the τ leptons, the invariant mass can be computed. The invariant mass distribution is shown in Fig. 5.7 for both signal and background samples (left plots).

The collinear approximation is not always a good approximation. A gaussian fit to the signal distribution in Fig. 5.7 gives a Higgs mass value of about 140 GeV/c^2 ($\sim$ 10% higher then the simulated mass of 125 GeV/c^2) and a sigma of about 35 GeV/c^2, mainly because no energy correction was applied to the missing energy. The long tail on the right part of the plot is due to events in which the τ lepton are produced back-to-back and part of the missing energy cannot be recovered. The b-tagged jets invariant mass gives a better fit as

shown in the next section.

b-tagged jets invariant mass

As mentioned above, to tag b jets the impact parameter b-tagging method has been used. For what concerns the fast simulation, a b-tagging efficiency of 0.5 has been used for the b jets, a mistagging efficiency of 0.1 for the c jets and 0.01 for uds jets and gluons. Only jets with $|\eta|$ <2.1 have been considered, to be sure that all the tracks inside the jet cone could be reconstructed . In order to increase the signal statistics it is required to tag at least one b jet. If more than two jets are tagged, then the two most energetic jets are considered. If only one jet is tagged then the most energetic jet (not tagged as τ or b) is considered. In order to avoid fake jets a cut on jet's E_T of 30 GeV is applied. In the following "First b jet" is the b jet with the highest Monte Carlo transverse energy, while "Second b jet" is the other. The algorithmic efficiency to tag the First b jet is 66%, the Second is 52%. These efficiencies don't include the geometrical acceptance and the reconstruction efficiency. The global efficiency becomes 55% for the First b jet and 22% for the Second b jet. The requirement to tag at least one of them has an overall efficiency of $\sim$ 65%.
Once the jets coming from the Higgs boson have been selected their energy is calibrated (using a parametrization in terms of jet energy and η) and the Higgs mass can be reconstructed. The b-tagged jets invariant mass distribution is shown in Fig. 5.7 for both signal and background samples (right plots). A gaussian fit to the signal distribution gives a mean value of 124 GeV/c^2 for the Higgs mass and a sigma of 30 GeV/c^2, which is better than the fit from the τ jets invariant mass.
The effect of the energy calibration is shown in Fig. 5.8, where the invariant masses without the energy correction (left plot) and with energy correction (right plot) are shown. This plot represents an ideal situation, when both b jets have been identified matching the jet direction with the b-quark direction and it is used only to show the energy calibration effects. The algorithm for the energy correction is described in [132]. The energy calibration can shift the mean value of the gaussian fit by about 20 GeV, with no relevant effect on the mass resolution. The requirement of tagging at least one b jet (instead of both) decreases the invariant mass resolution. Fig. 5.7 clearly shows how it gets worse with respect to the ideal situation described in Fig. 5.8.

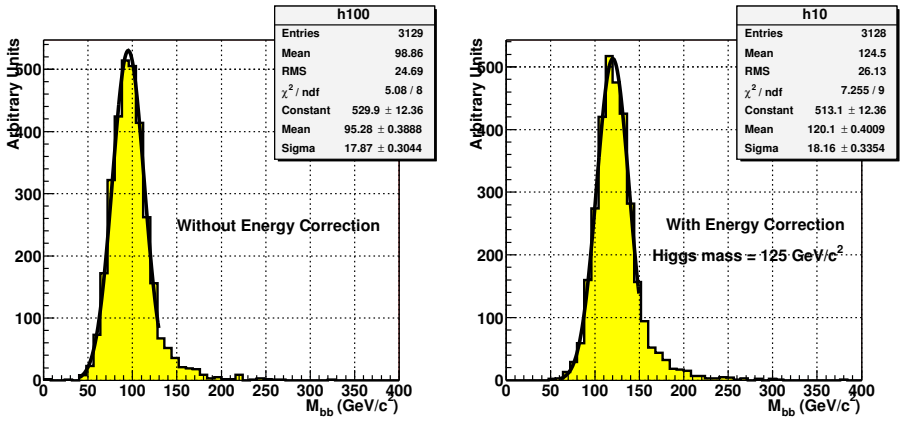

Figure 5.8: Invariant mass of b jets from the Higgs decay.

Selections

A foundamental background rejection comes from the HLT selection, but is not enough to extract the signal. A lot of kinematical variables have been examined, but in almost all of the them the signal and background distributions are very similar and do not provide a clear signature for the signal. The following list illustrates the off-line selections that have been used in the analysis (after having tagged the b jets):

- p_T of the b-tagged jets greater than 30 GeV, and p_T of the most energetic one greater than 55 GeV;
- transverse invariant mass of lepton and missing energy smaller than 35 GeV/c^2;

The max(p_T) and transverse invariant mass of lepton and missing energy distribution are shown in Fig. 5.9. The transverse invariant mass for the lepton and the total missing energy is used to efficiently suppress the W+jets background, while the max(p_T) of the b-tagged jets is used to suppress the Z+jets background.
The elicity angular distributions, i.e. the angle distribution of the jets with respect to the Higgs flight direction in the center of mass of the Higgs boson

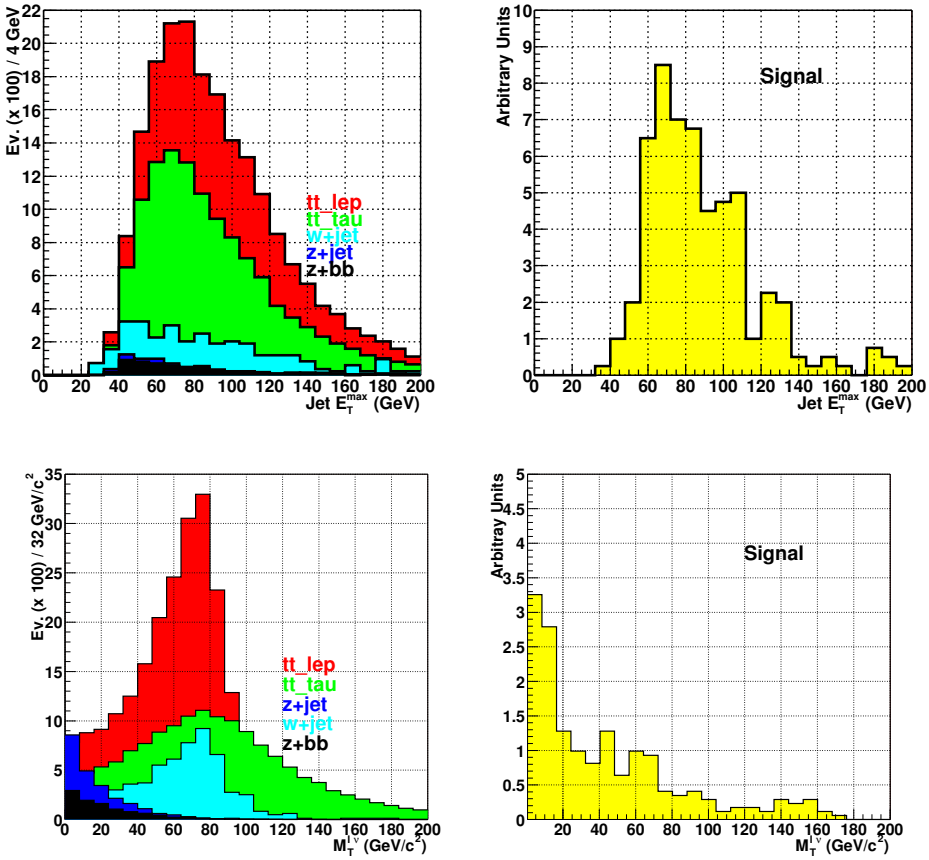

Figure 5.9: Max(p_T) of the b-tagged jets distributions (upper plots). Transverse invariant mass of lepton and missing energy (bottom plots). The plots on the left refers to the background samples, the plots on the right refers to the signal one.

and the angular distribution of the Higgs boson with respect to the radion flight direction in the center of mass of the radion, have also been considered. For scalar particles these distribution should be flat. However they have been found not to be discriminant with respect to the background selection, mainly due to the fact that the Higgs bosons are not relativistic.
After these selections, which are mainly independent from the Higgs and radion masses, the analysis is divided into two cases:

- The Higgs boson has not yet been discovered and we don't know its mass;
- The Higgs boson has been discovered and we can use some constraints on its mass to search for the radion.

The two cases are investigated in the following sections. The second case offers more discovery possibilities and will be discussed with more details.

5.2.4 Analysis strategy when the Higgs boson has not yet been discovered

In the case in which we don't know the mass of the Higgs boson, we can scan, through a sliding windows technique, the invariant mass distributions of the τ and b-tagged jets to search for an excess of events. As shown in the invariant mass distributions, the signal and background have similar shapes, and there is no way to extract the signal significance through a fit procedure. We can only measure an excess of signal events with respect to the expected background. In order to extract the significance of the signal events the following definition of significance has been considered: $N_{\rm sig}/\sqrt{N_{\rm bkg}}$, where $N_{\rm sig}$ and $N_{\rm bkg}$ are the number of expected signal and background events after all selections (including the mass selection on τ jets and b jets invariant masses). In order to find the Higgs mass, a sliding window procedure has been used. A scan in the mass distribution of the two reconstructed Higgs bosons has been done. Two mass windows have been moved both centered on the same value, untill a significant excess of expected number of signal events has been found: 50 GeV/c^2 ($\pm$ 25 GeV/c^2) for the b-tagged jets invariant mass (M_{bj}) and 60 GeV/c^2 (-25 and +35 GeV/c^2) for the τ jets invariant mass ($M_{\tau\tau}$). Figure 5.10 shows how a peak would appear (in the τ jets invariant mass distribution) when a mass window, centered around the simulated Higgs mass, is applied on the b-tagged jets invariant mass. In the upper and bottom plots a mass window in a region with very little signal is considered, while in the middle plot (when the mass window is around the simulated Higgs mass) the peak reaches the best significance. As we can see the signal events are consistent with the decay of a second particle with the same invariant mass of the b-tagged jets pair. Figure 5.11 (left plot) shows how the significance of a possible radion signal changes as a function of the center of the mass windows of the b-tagged jets and τ jets invariant masses when the selection is applied to both invariant masses. The plot has been done considering the maximal signal cross section. The maximum significance clearly falls at a reconstructed b-tagged jets invariant mass of 125 GeV/c^2. After the off-line selections and the following cuts:

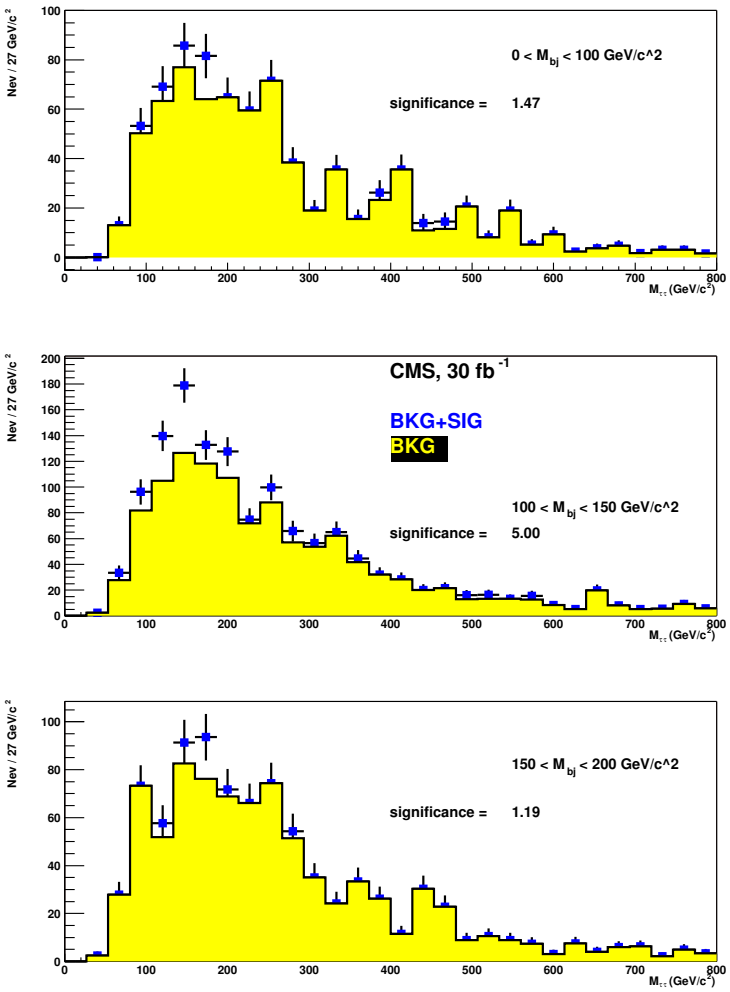

Figure 5.10: τ jets mass peak, with its significance, for three different mass windows of the b-tagged jets invariant mass. Upper and bottom plots are for mass windows out of the signal region, while the middle plot shows the peak when the mass window is centered around the simulated Higgs mass. The significance is evaluated using the selection on the b-tagged jets invariant mass, and without the selection on the τ jets invariant mass.

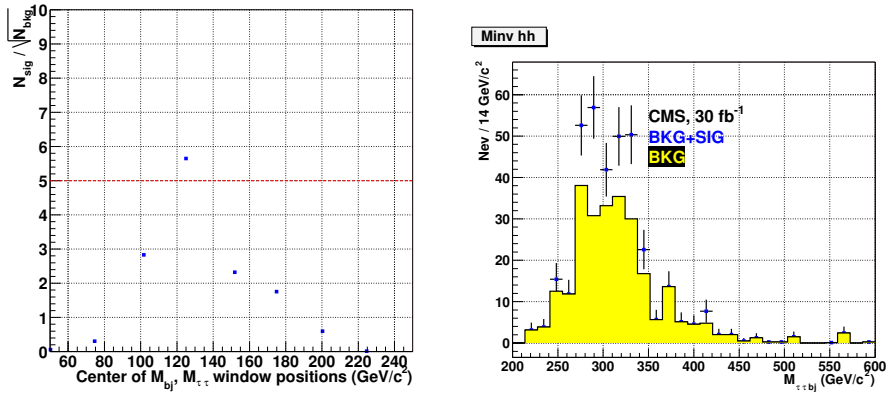

Figure 5.11: Left plot: Significance of the signal events as a function of the center value of the mass windows, when selecting on both b-tagged jets and τ jets invariant masses, for the maximal signal cross section. Right plot: Reconstructed radion mass, for signal plus background.

- $100 < M_{bj} < 150$ GeV/c^2;
- $100 < M_{\tau\tau} < 160$ GeV/c^2;

about 96 signal events (for the maximal cross section case) and 281 background events are expected, see Tab. 5.7 for more details. The significance in this case is above 5.7. The probability to see a positive excess of 5.7 sigma (accordingly to a gaussian distribution) is about 6×10^{-9}. This probability has to be multiplied by the number of *trials* we have done to see such a fluctuation. Indeed the background can fluctuate in any considered mass window, and we have to take into account all these trials. In this case we have to multiply 1.9×10^{-8} by a factor 5.6, that is the ratio between the total mass interval we have explored (from 110 to 250 GeV) divided by the window steps (25 GeV). The final significance is reduced to 5.4. Figure 5.11 (right plot) shows how the excess of events would appear in the invariant mass distribution of $\tau\tau bj$ ($M_{\tau\tau bj}$). The signal and the background have similar shapes and so no further information can be extracted from this plot.
A much better situation is indeed achieved in the case in which the Higgs boson has been already discovered, as described in the next section.

5.2.5 Analysis strategy when the Higgs boson has already been discovered

If the Higgs boson has already been discovered, a selection using the *true* Higgs mass value can be performed, without using the sliding windows procedure. The *true* Higgs mass means the value measured in other channels. For a Higgs boson of about 125 GeV/c^2 the best way to measure its mass is through its decay into two photons. In this way it will be possible to measure it with a precision better than 1%. The Monte Carlo simulation can give important informations on the resolution of the reconstructed Higgs mass and a selection on both τ jets and b-tagged jets invariant masses can be applied:

- b-tagged jets reconstructed invariant mass: $100 < M_{bj} < 150$ GeV/c^2;
- τ jets reconstructed invariant mass: $100 < M_{\tau\tau} < 160$ GeV/c^2.

Then the energy of the reconstructed jets can be rescaled using a kinematical fit imposing that the reconstructed invariant masses to be equal to the *true* Higgs mass. In this way a much better resolution on the radion mass can be achieved. The following section describes how a kinematical fit can be performed.

Kinematical Fit

The squared invariant mass of two jets, considering the jets as massless, is given by the following formula:

$$\mu^2 = 2\omega_1\omega_2(1 - \cos\theta),$$

where ω_1 and ω_2 are the measured energies of the jets and θ is the angle between the two jet directions. Usually dealing with jets, the effect of the angle uncertainty on the mass resolution is negligible. Only in the case of Higgs decaying into photons the angular resolution plays an important role in the reconstruction of the invariant mass. This fit has the aim to rescale the jet energies without modifying their directions.
E_1 and E_2 will identify the new, corrected, jet energies. A method to obtain them is minimizing the chi-square form:

$$\chi^2 = \left(\frac{E_1 - \omega_1}{\sigma_1}\right)^2 + \left(\frac{E_2 - \omega_2}{\sigma_2}\right)^2 + \lambda\left(m^2 - 2E_1E_2(1 - \cos\theta)\right),$$

where $\sigma_{1,2}$ are the energy resolutions, m is the true Higgs mass and λ is the Lagrange multiplicator which introduces the constraint on the invariant mass. The χ^2 can be minimized with respect to E_1, for example, and get the following fourth-order equation:

$$f(E_1) = a_4 E_1^4 + a_3 E_1^3 + a_2 E_1^2 + a_1 E_1 + a_0 = 0, \tag{5.2}$$

where $a_4 = \sigma_1^2/\sigma_2^2$, $a_3 = -\omega_1 a_4$, $a_1 = \omega_1\omega_2^2 m^2/\mu^2$, $a_0 = -(\omega_1\omega_2 m^2/\mu^2)^2$. The above equation has two real and positive solutions. The exact solution is too complicated and an approximated solution can be achieved linearizing eq. 5.2. The solution can be further simplified considering the resolution for the jet energy as: $\sigma_i = a\sqrt{\omega_i}$.
The simplified solution for E_1 and E_2 are given in the following formulas, where the jet energies are rescaled by the factor $E_{1,2}/\omega_{1,2}$. For more details see [133].

$$E_1 = \omega_1 + \left(\frac{m^2 - \mu^2}{\mu^2}\right) \times \frac{\omega_1\omega_2}{\omega_1 + \omega_2}, \tag{5.3}$$

$$E_2 = \omega_2 + \left(\frac{m^2 - \mu^2}{\mu^2}\right) \times \frac{\omega_1\omega_2}{\omega_1 + \omega_2}. \tag{5.4}$$

Figure 5.12 shows the rescaling factors for the two τ (upper plots) and the two b jets (bottom plots) used in the analysis. For what concerns the τ leptons, the jets corrected for the missing energy of the neutrinos have been used. In this case considering the formula $\sigma_E = a\sqrt{E}$ as the τ lepton energy resolution is an approximation which should be checked since missing transverse energy is involved. The distributions for the τ leptons are peaked at a value below 1, mainly due to the long tail on their reconstructed invariant mass, while for the first b jet (the one which is always tagged) the distribution shows a sharp peak near 1. For the second b jet (not always tagged) the distribution is broader. Figure 5.13 shows the effect of the kinematical fit on the reconstructed radion mass ($M_{\tau\tau bj}$) for background (left plots) and signal (right plots). The upper plots are made before appling the kinematical fit, the bottom plots after. Even if the correction factors for the energies comes from an approximated solution the effect on the signal events is impressive.

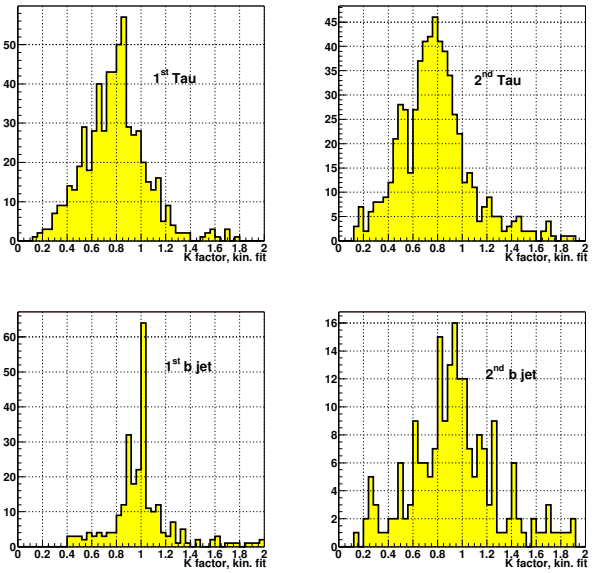

Figure 5.12: Rescaling factor for the jet energies for the τ (upper plots) and the b jets (bottom plots). See text for more details.

Signal extraction

After the kinematical fit, and all the selections described above, we have still to separate the signal events from the background. Figure 5.14 (left plot) shows the reconstructed radion mass for signal plus background after all selections and the kinematical fit (the plot is made using the maximal signal cross section). The solid line is the result of the fit to the signal+plus background distribution, while the dashed one is the result of the fit to the background only. The background shape can be extracted with good precision from the data themself as shown in the next section. For a radion mass of 300 GeV/c^2 a mass resolution of about 5% is expected. The signal plus background fit has been performed using two gaussian functions. disregarding the mass region below 250 GeV/c^2 which is not kinematically accessible. The signal gaussian has a mean of 300 GeV/c^2 and a σ of 15 GeV/c^2. The background function is centered around 285 GeV/c^2 with a σ of about 45 GeV/c^2. In the fit only the relative weights have been left free in order to extract the number of signal and background events from the fit itself. The fit procedure gives an estimate of the number of the background events with a precision better than 10%.

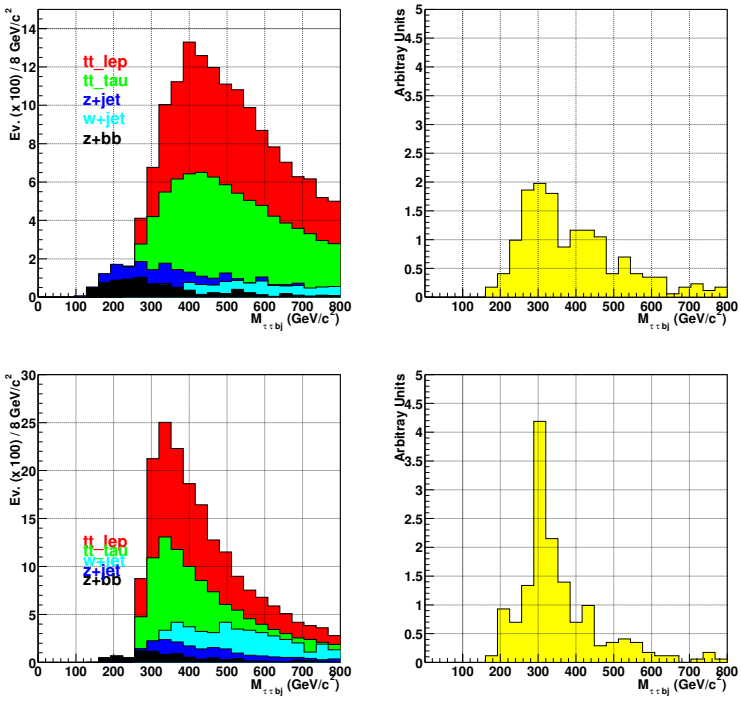

Figure 5.13: Reconstructed radion mass before selections on the τ jets and b-tagged jets invariant masses, for background (left plot) and signal (right plot). Upper plot are made before appling the kinematical fit, bottom plot after.

Figure 5.14 (right plot) shows the same distribution after subtraction of the fitted background.

A further selection on this reconstructed mass is then applied: $290 < M_{\tau\tau bj} < 330$ GeV/c^2. Table 5.7 shows the signal and background cumulative efficiencies for trigger, off-line and invariant mass selections. The final signal efficiency is around 0.27%, while the background efficiency is less than 3×10^{-5}. The total number of background events after all selections (for 30 fb^{-1}) is 84, in which the $t\bar{t}$ sample gives the biggest contribution (64 events) and the W+jets sample is negligible. The contribution of the tt_{2tau} sample to the background (which has not been simulated, and for which the same efficiency as for the tt_{tau} sample has been used) has been estimated to be only 10% of the total number of events, so that the number of background events increases to ~ 92. The number of signal events depends on the choice of the ξ and Λ_ϕ parameters. For the highest cross section of 0.96 pb, (ξ= -0.35 and Λ_ϕ=1 TeV) about 79 signal events are expected in the same running period, for a significance

Selection	**Samples efficiency (%)**					
	$\phi \rightarrow$ hh	$t\bar{t}_{had}$	$t\bar{t}_{tau}$	Z+bb	Z+jets	W+jets
Trigger	6.0± .2	.57±.02	3.1±.2	1.4±.2	.35±.02	.039±.002
b-tagging	2.8±.2	.324±.002	1.740±.005	.44±.02	.0250±.0005	.0084±.0003
$\Delta R_{l\tau} > 0.1$	2.6±.2	.255±.002	1.091±.004	.30±.02	.0188±.0005	.0071±.0003
$p_T^b > 30$ GeV, $\max(p_T^b) > 55$ GeV	1.98±.15	.199±.002	.736±.003	.10±.01	.0030±.0002	.0025±.0002
M_T lep+$\nu < 35$ GeV	1.1±.1	.039±.001	.118±.001	.071±.008	.0021±.0001	.0005±.0001
100 GeV $< M_{\tau\tau} < 160$ GeV	.52±.07	.0054±.0003	.0285±.0006	.0244±.005	.00067±.00008	.00002±.000015
100 GeV $< M_{\rm bj} < 150$ GeV	.33±.05	.0018±.0002	.0087±.0004	.0090±.003	.00028±.00005	0
290 GeV $< M_{\tau\tau bj} < 330$ GeV	.27±.05	.00054±.0001	.0030±.0002	.0054±.002	.000063±.00002	0
Number of expected events	**79**	**40**	**24**	**13**	**7**	**0**

Table 5.7: Cumulative efficiency for the overall analysis (trigger and off-line).

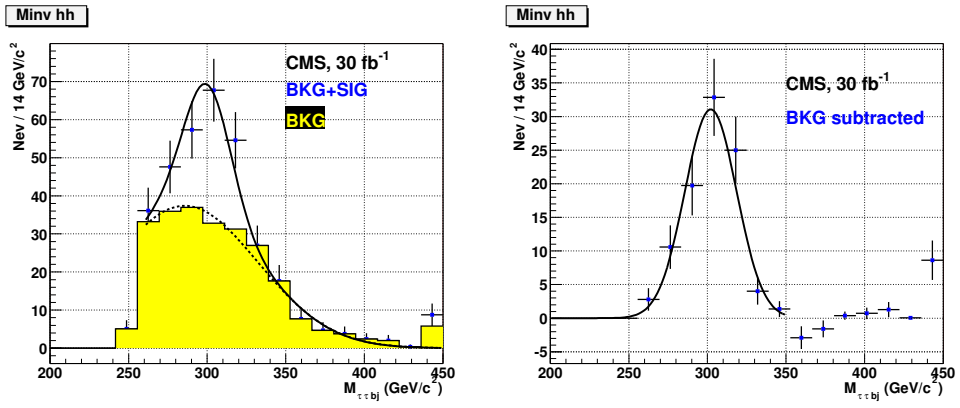

Figure 5.14: Left plot: reconstructed radion mass, for signal plus background. Right plot: reconstructed raion mass after having subtracted the fitted background.

greater than 8. In Fig. 5.15 (left plot) the central curve shows the 5 σ discovery contour in the (ξ, Λ_ϕ) plane (i.e. the region where $N_{sig}/\sqrt{N_{bkg}}$ is greater than 5), considering only statistical uncertainties. To take into account the uncertainties on the NLO cross section other two curves have been drawn in the same plot. The area with the maximum extension is obtained assuming the k_{min}-factor while the smallest corrisponds to assume the k_{max}-factor (see Tab. 5.4). The plot on the right shows the excluded region at the 95% Confidence Level in the (ξ, Λ_ϕ) plane. The assumption of having observed a total number of events equal to the expected number of background events has been made. The maximal number of signal events compatible with this assumption is 21, see [135] for more details.
The next section describes how the background shape and number of events can be extracted from the data and the effect of systematical uncertainties on the background estimation.

Evaluation of background from the data and effect of systematics

In order to minimize the uncertainties on the background and to extract the shape of the invariant mass distribution ($M_{\tau\tau bj}$) for the various background samples, they have to be measured after the trigger and off-line selections, in a signal free region.
For what concerns the Z+jets background, the leptonic Z decays (electrons and muons) can be treated as a pure control sample. In this case the value of the τ-tagging efficiency and the efficiencies for the $M_{\tau\tau}$ invariant mass selection

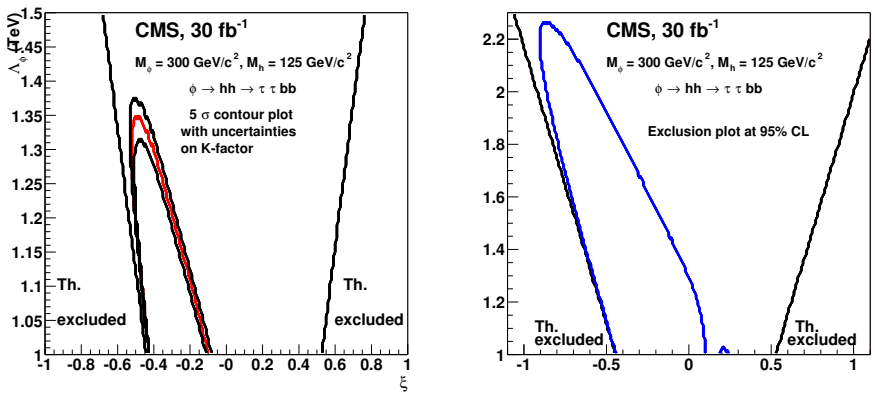

Figure 5.15: 5 σ discovery contours considering the k_{min} and k_{max}-factor, only statistical uncertainties have been considered (left plot). Right plot: 95% CL exclusion plot. No NLO uncertainties have been considered in the plot.

must be known. They can be measured using pure Z events, evaluating the ratio between the number of events in which the Z decays into τ leptons (with one τ jet in the final state) and the number of events in which the Z decays into electron and muons. Detailed studies have never been done, but statistics should allow these measurements to be done with an accuracy of the order of 5% level.

For what concerns the top and W backgrounds, the request that the transverse invariant mass distribution of lepton and missing energy be larger than 30 GeV/c^2 ensures that events are selected in a signal free region. In this region, the signal contamination is below 1.5% (with the maximum cross section), while the contribution of the Z+jets events is negligible. In Fig. 5.16 the curve is the sum of the three background samples, without the signal. Using this selection it is possible, having a background control sample, to extract the contribution of top and W backgrounds to the $M_{\tau\tau bj}$ distribution. A gaussian fit to the distribution gives a mean value of about 285 GeV/c^2, while the fit to the sum of top and W backgrounds has a mean value of 292 GeV/c^2. The sigma of the gaussian is about 46 GeV/c^2 in both cases (total background and top and W+jets samples only). The shift of few GeV is related to the contribution of the Z+jets background. Detailed studies are needed to understand better the precision with which these backgrounds will be known at LHC. A reasonable systematical uncertainty can be considered of order 5-10%.

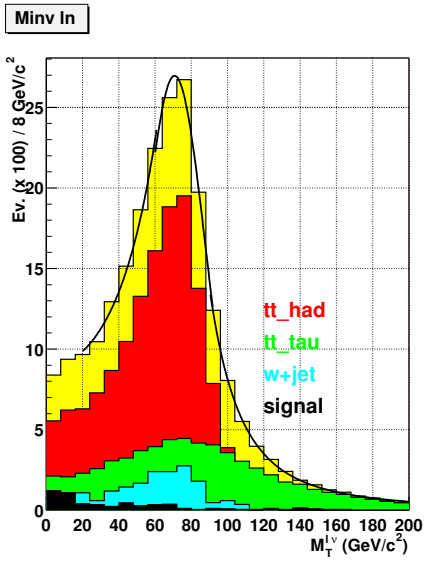

Figure 5.16: Transverse invariant mass of lepton and missing energy distribution for the top sample and the signal. In yellow the sum of the two background sample (without the signal) is fitted in order to measure its contribution.

When systematic uncertainties are present, the following formula for the significance has been adopted:

$$N_{\rm sig}/\sqrt{N_{\rm bkg} + (\epsilon_{\rm sys} * N_{\rm bkg})^2},$$

where $\epsilon_{\rm sys}$ is the systematic uncertainty. Figure 5.17 shows how the contour plots change when a systematic uncertainties of 5% (left plot) and a more conservative 10% (right plot) are considered. For what concerns the 95% CL exclusion plot, with a systematic uncertainty of 5% the maximal number of compatible signal events is 23. This number increase to 27 with a systematic uncertainty of 10%. In this case only Λ_ϕ values below 2 TeV can be excluded, instead of 2.2 TeV as happens in the absence of systematical uncertainties.

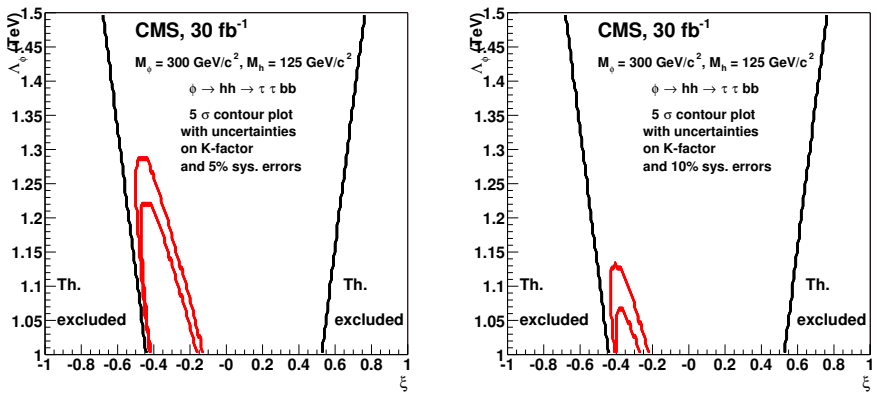

Figure 5.17: 5 σ discovery contours considering the k_{min} and k_{max}-factor and systematic uncertainties of 5% (left plot) and 10% (right plot) on the background.

5.3 $\gamma\gamma$bb final state

In this section the analysis of the $\gamma\gamma$ bb decay channel, is presented. The background processes, trigger and off-line selections are described without entering too much in details. At the end of the section a comparison between this final state and the $\tau\tau$ bb is given.

The possibility to reconstruct the Higgs mass with extreme precision due to the Higgs decay in two photons allows the $\gamma\gamma$bb final state to be the most interesting. As in the previous case the signal events have been processed with the full detector simulation and reconstruction. Irreducible di-photon backgrounds were generated with CompHEP for the $\gamma\gamma$jj (j=u,d,s,g) process and with MadGraph [138] for the $\gamma\gamma c\bar{c}$ and $\gamma\gamma b\bar{b}$ processes. The generator level preselections are $p^{\gamma}_{T,max\ (min)}$ >35 (20) GeV/c, p^{j}_{T} >20 GeV/c, $|\eta|$ <2.5, $\Delta R_{\gamma j}$ >0.3, ΔR_{jj} >0.3. Cross sections are shown in Tab. 5.8. Fast detector simulation with realistic resolutions for the photon and jet energies and for the track momentum has been used. Track reconstruction efficiency has been assumed to be 0.9.

Events are required to pass Level-1 and High Level Trigger (HLT) selections

	$\gamma\gamma$jj	$\gamma\gamma c\bar{c}$	$\gamma\gamma b\bar{b}$
cross-section, fb	13310	778	76

Table 5.8: Background cross sections.

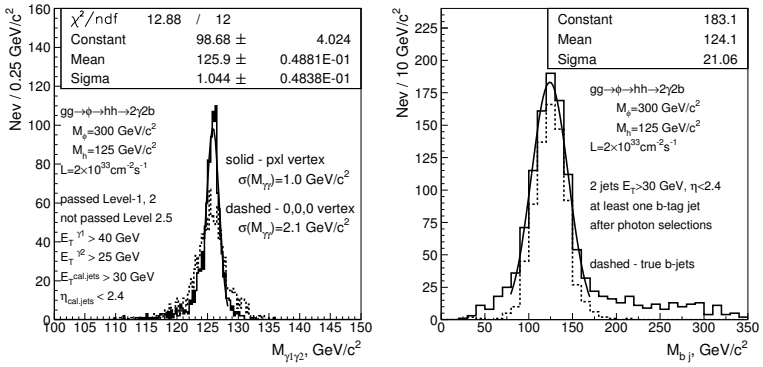

Figure 5.18: The reconstructed di-photon mass without and with the vertex position corrections (left) and reconstructed b j invariant mass (right) for the signal events.

for the di-photon stream with HLT thresholds on photons of 40 and 25 GeV/c. Photons are then required to be isolated in the tracker and in the electromagnetic calorimeter.

The choice of the b jet candidates is similar to the one presented in the previous analysis: the two highest E_T jets of $E_T > 30$ GeV and $|\eta| < 2.4$ reconstructed with the calorimeters are taken as b jet candidates from $h \rightarrow b\bar{b}$ decay. At least one of these two jets has to be tagged as a b jet. The efficiency of the single b-tagging (for signal events) is 0.61. For what concerns the background samples an efficiency of b-tagging of 0.5 for b jets and a mistagging probability of 0.01 (0.1) for u,d,s,g (c) jets have been used. The signal vertex in the event is reconstructed with the Pixel Detector. In 97 % of the events the vertex identified for the signal is found within a $\pm$ 200 μm window around the true position of the signal vertex. The presence of two calorimeter jets with $E_T > 30$ GeV and $|\eta| < 2.4$ is required before vertex reconstruction. For the di-photon mass reconstruction the energies and the directions (corrected for the vertex position) of the two highest E_T Level-2 e/γ candidates are used.

Figure 5.18 shows the reconstructed di-photon mass without and with the vertex position corrections (left plot) and M_{bj} (right plot) for signal events with arbitrary normalization. Figure 5.19 shows the di-jet M_{bj} and di-photon $M_{\gamma\gamma}$ mass distributions for background, after selections 1-3 of Tab. 5.10 and b-tagging, and for signal after selections 1-8 of Tab. 5.9 with 30 fb^{-1}. The signal is shown for the point with maximal cross section times branching ratio in the (ξ, Λ_ϕ) plane. Figure 5.20 (left plot) shows the $M_{\gamma\gamma bj}$ mass distribution

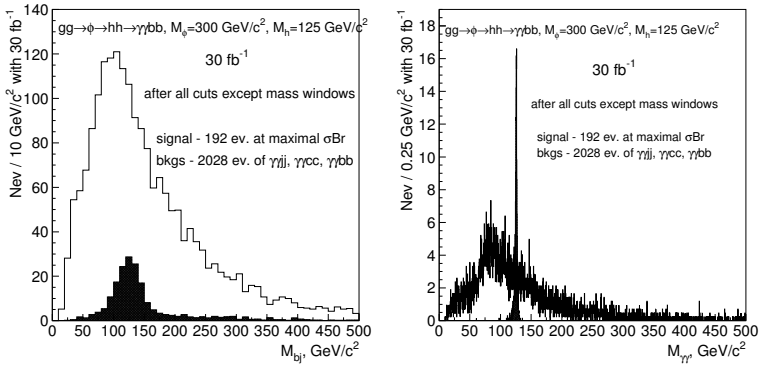

Figure 5.19: Background after selections 1-3 in Tab. 5.10 and b-tagging and signal after selections 1-8 in Tab. 5.9 with 30 fb^{-1}. Di-jet mass (left plot) and di-photon mass (right plot). Signal is shown for the maximal cross section times branching ratios point in the (ξ, Λ_ϕ) plane.

for the background after selections 1-3 in Tab. 5.10 and b-tagging and for the signal after selections 1-8 in Tab. 5.9 with 30 fb^{-1}. Signal is shown for the point with maximal cross section times branching ratio in the (ξ, Λ_ϕ) plane.

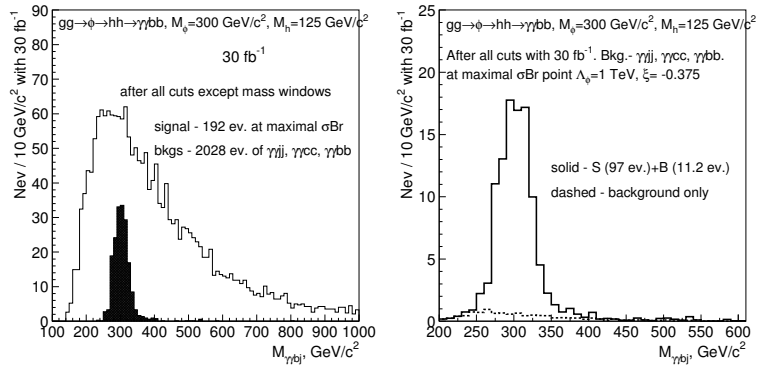

Figure 5.20: Left plot : $M_{\gamma\gamma jj}$ for the background after selections 1-3 in Tab. 5.10 and b-tagging and for the signal after selections 1-8 in Tab. 5.9 with 30 fb^{-1}. Right plot : $M_{\gamma\gamma bj}$ for the background and the signal plus background after all selections with 30 fb^{-1}. In both plots signal was evaluated for the maximal cross section times branching ratios point in the (ξ, Λ_ϕ) plane.

Further selections require di-jet mass M_{bj} to be in the window $m_h \pm 30$ GeV/c^2 (efficiency 65 %) and di-photon mass $M_{\gamma\gamma}$ in the window $m_h \pm 2$ GeV/c^2 (efficiency 78 %). Finally, the $M_{\gamma\gamma bj}$ invariant mass should be in the window of

selection criteria	relative efficiency	absolute efficiency
Level-1	0.738	0.738
Level-2	0.927	0.685
Level-2.5 photon stream	0.996	0.683
$p_{rmT}^{\gamma_1,\ rm2} > 40$, 25 GeV/$c$	0.871	0.595
tracker isolation of photons	0.682	0.406
ECAL isolation of photons	0.909	0.369
two jets of $E_{rmT} > 30$ GeV, $\|\eta\| < 2.4$	0.341	0.126
at least one b jet	0.610	0.077
$95 < M_{bj} < 155$ GeV/c^2	0.648	0.050
$M_{\gamma\gamma}$ mass window of 4 GeV/c^2	0.780	0.039
$250 < M_{\gamma\gamma bj} < 350$ GeV/c^2	0.950	0.037

Table 5.9: Trigger end off-line selection efficiencies for the signal.

	$\gamma\gamma$jj	$\gamma\gamma c\bar{c}$	$\gamma\gamma b\bar{b}$
selections	efficiency		
$E_T^{\gamma_{1,2}} > 40$, 25 GeV, $\|\eta\| < 2.5$	0.446	0.466	0.487
tracker isolation in cone 0.3	0.328	0.345	0.379
two jets $E_T > 30$ GeV, $\|\eta\|$ <2.4	0.127	0.125	0.133
$M_{\gamma\gamma}$ window 4 GeV/c^2	0.00278	0.00263	0.00410
M_{jj} window 60 GeV/c^2	0.00086	0.00096	0.00144
$M_{\gamma\gamma jj}$ window 100 GeV/c^2	0.00045	0.00061	0.00123
N events after all selections including b-tagging	4.2 ± 0.8	2.0 ± 0.6	2.0 ± 0.6

Table 5.10: Background efficiency and number of events with 30 fb$^-$1 after all selections including b-tagging.

$m_\phi \pm$ 50 GeV/c^2 (efficiency 95 %). The signal efficiency of the whole selection chain is 3.7 %.

For $\Lambda_\phi = 1$ TeV and $\xi = 0$ the expected number of signal events with 30 fb^{-1} is 41. Efficiency of selections and expected number of events with 30 fb^{-1} , including b-tagging, are shown in Tab. 5.9 for the signal sample and in Tab. 5.10 for the background samples. Statistical errors on the expected number of events are also shown. The number of background events was then multiplied by 0.92 and by 0.90 to take into account Level-1 e/γ trigger efficiency and calorimeter isolation efficiency not taken into account in the fast simulation. These efficiencies were obtained from full simulation of the signal events. With a total number of background events of 6.9 for 30 fb^{-1} the CMS discovery reach in the (ξ, Λ_ϕ) plane has been evaluated. Reducible backgrounds from γ + three jets

and four jet backgrounds have still to be evaluated. We expect (from inclusive $h \rightarrow \gamma\gamma$ studies) that the total reducible background will be at the same level or even less than the total irreducible one.

In this study we used the ratio of the reducible to the total background of 0.4 [139]. Figure 5.21 (left plot) shows the 5 σ discovery contour in the (ξ, Λ_ϕ) plane when the reducible background has been taken into account. Dashed line contours present the discovery reach when the irreducible background cross sections are calculated with the renormalization and factorization scales set to $0.5\times\mu_0$ and to $2\times\mu_0$. The background can be determined directly from the $\gamma\gamma$ plus two jets data obtained after all selections (including b-tagging, and except those on the final masses) have been applied. The final cuts on $M_{\gamma\gamma}$, M_{bj} and $M_{\gamma\gamma bj}$ introduce systematic uncertainties on the expected number of background events.

The error due to the systematics is determined by the following factors : the energy scale uncertainty for photons and jets and the theoretical uncertainty due to the possible different shape of the mass distributions for the different renormalization and factorization scales and the different structure functions. The assumption of 0.1 % uncertaincy on the photon scale [55, 137] and 1 % uncertainty of the jet scale [62] leads to 1.4 % incertainty on the $M_{\gamma\gamma}$ cut efficiency and 1 % uncertainty on the M_{bj} cut efficiency. The variation of the renormalization and factorization scale leads to $\simeq$ 3 % uncertainty on the efficiency of the mass cuts. This value is expected to be smaller with the next-to-leading order calculations which are still missing in the literature. The total uncertainty is thus 4.7 % (the energy scale uncertainties were added in quadrature and then the renormalization and factorization scale uncertainties were added linearly). The right plot in Fig. 5.21 shows two contours without and with the systematic uncertainty discussed above. The contours are evaluated with the total background and for the irreducible background cross section. One can see that the systematic uncertainties hardly affect the discovery reach. This is due to the fact that the signal to background ratio for the points of significance 5 and above, is more than one, so that uncertainties on the background have small effects.

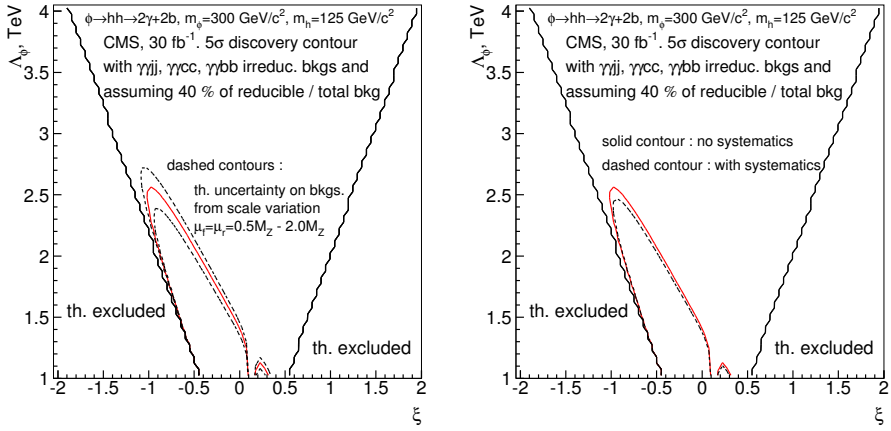

Figure 5.21: Left plot : 5 σ discovery contour for $\phi \to$ hh $\to \gamma\gamma$+b$\bar{\text{b}}$ channel (m_ϕ=300 GeV/c^2, m_h=125 GeV/c^2) with 30 fb^{-1}. Statistical significance was calculated with the Poisson probability; the ratio of the reducible to the total background of 0.4 was used. Dashed line contours present the discovery reaches when the irreducible background cross sections were calculated for the renormalization and factorization scales set to $0.5\times\mu_0$ and to $2\times\mu_0$. Right plot : 5 σ discovery contour for $\phi \to$ hh $\to \gamma\gamma$+b$\bar{\text{b}}$ channel (m_ϕ=300 GeV/c^2, m_h=125 GeV/c^2) with 30 fb^{-1}. Statistical significance was calculated with the Poisson probability; the ratio of the reducible to the total background of 0.4 was used. Irreducible background cross sections were calculated for the renormalization and factorization scales set to μ_0. Solid (dashed) line contour presents the discovery reach without (with) systematical error taken into account.

Comparison between $\tau\tau$ bb and $\gamma\gamma$ bb final state.

The two final states described in the sections above are to some extent complementary. The $\gamma\gamma$ final state can cover a bigger region of the (ξ,Λ_ϕ) plane, but it has fewer number of signal events than the $\tau\tau$ one. Moreover photons are much more sophisticated objects than τ jets and a very good working condition of the calorimeter is required to achieve the shown results. The narrowness itself of the invariant mass distribution of the two photons is strongly dependent on the detector performance. On the other hand the τ jets invariant mass suffer from the presence of neutrinos; the recovery of the missing energy is not yet optimized and further work is needed in order to improve the invariant mass resolution.

The best situation is achieved when the Higgs mass is known. The use of a kinematical fit improves the radion mass resolution and the signal can be easily

	Cross Section	Events in 30 fb^{-1}
Signal	10.3 pb	3.1×10^5
QCD $\hat{p}_T$ (30-50) GeV/c	0.1957 mb	5.9×10^{12}
QCD $\hat{p}_T$ (50-80) GeV/c	0.0258 mb	7.7×10^{11}
QCD $\hat{p}_T$ (80-120) GeV/c	0.0036 mb	1.0×10^{11}
QCD $\hat{p}_T$ (120-170) GeV/c	0.0006 mb	1.8×10^{10}
$t\bar{t}$	615 pb	1.8×10^7
$Zb\bar{b}$	349 pb	1.0×10^7

Table 5.11: Signal and background events in 30fb^{-1}.

extracted in both final states fitting the invariant mass distribution.

5.4 bbbb **final state**

In this section the analysis of the final state with four b jets is presented. The analysis is more difficult than the previous described ones due to the huge QCD background. Even if it selects the greatest number of signal events, the number of background events is so big that it makes this channel unusable.
The signal cross section times branching ratios for $gg \rightarrow \phi \rightarrow hh \rightarrow b\bar{b}b\bar{b}$ process is 10.3 pb for $\Lambda_\phi = 1$ TeV and $\xi = -0.35$. The main QCD multi jet background was generated by PYTHIA in a different $\hat{p}_T$ bins. Other backgrounds considered are $t\bar{t}$ and $Zb\bar{b}$. In Tab. 5.11 cross sections and expected numbers of events with 30 fb^{-1} are summarized, (all the background cross sections are at Leading Order). Fast detector simulation with CMSJET package was used for both signal and background samples. A dedicated trigger selection has been developed to keep QCD multi jet background rate at the acceptable level while maintaining a high efficiency for the signal.
The optimized trigger strategy for the four b jets final state is the following:

- Level-1 selection (standard Level-1 95% efficiency thresholds are applyed [62])
  - 1 jet $E_T > 164$ GeV (in $|\eta| < 0.8$) OR
  - 2 jets $E_T > 129$ GeV (in $|\eta| < 0.8$) OR
  - 3 jets $E_T > 76$ GeV (in $|\eta| < 0.8$) OR
  - 4 jets $E_T >62$ GeV (in $|\eta| < 0.8$).

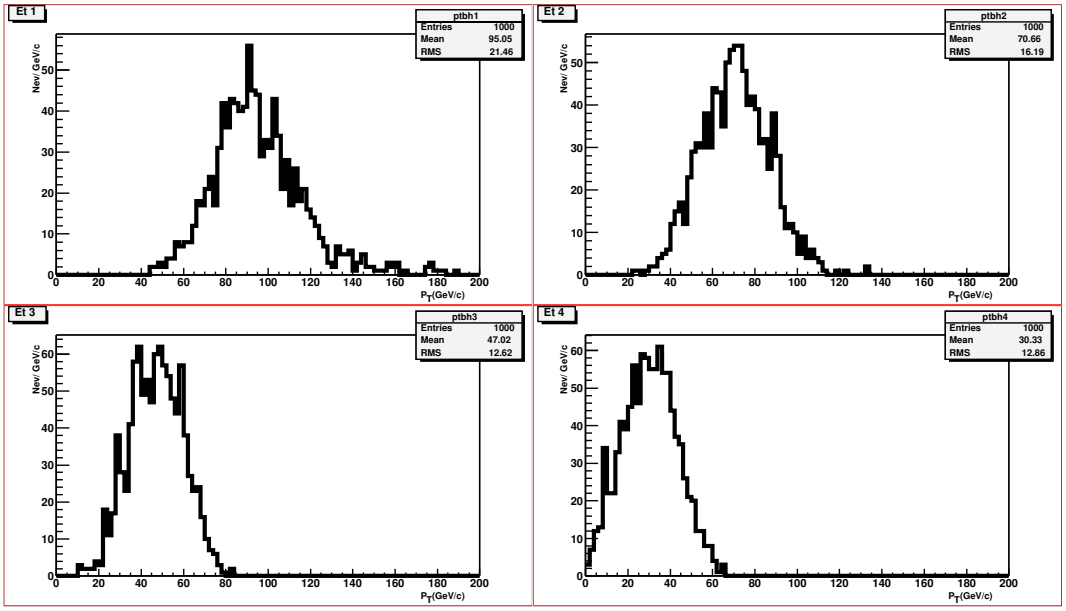

Figure 5.22: The signal kinematics: the transverse energy distributions for the four highest E_T jets ordered in decreasing E_T. Jets were reconstructed at the generator (PYTHIA) level with the cone algorithm using a cone size of 0.4.

- HLT selection:
  - at least 4 jets with $E_T > 30$ GeV and $|\eta| < 0.8$ in the final state AND
  - at least 2 b-tagged jets (b-tag is done with 2 tracks associated with the jet with $\sigma_{\rm IP}$ >2.)

The jets transverse energy for the signal events is presented in Fig. 5.22 that shows the E_T of the four most energetic jets reconstructed at the generator (PYTHIA) level with the cone algorithm with a cone size of 0.4.

Table 5.12 shows the trigger efficiency for signal and all background sources considered. Where the statistics is low, upper limits are given in terms of 95% confidence level. The overall QCD rate is, after the described selection, ∼5 Hz. The off-line selection is strictly signal dependant. The idea is to reconstruct Higgs bosons and the radion with a certain accuracy to define a mass window. The request to have at least four jets gives the possibility to reconstruct 2 objects from jet invariant mass. The best combination, that reconstructs 2 objects as similar as possible (the Higgs boson), is taken. After that the 4 selected jets are used to reconstruct the radion mass. The Higgs bosons and radion reconstruction can hence be summarized by the following

	$\sigma \times BR$	$\epsilon_{trigger}$	ϵ_{tot}	Evenets in 30 fb^{-1}
Signal	10.3 pb	0.038	0.031	$9.57{\cdot}10^{3}$
QCD $\hat{P}_T(30-50)$	0.1957 mb	$< 1.1{\cdot}10^{-7}$	$< 1{\cdot}10^{-7}$	$< 5.7{\cdot}10^{5}$
QCD $\hat{P}_T(50-80)$	0.0258 mb	$< 5{\cdot}10^{-7}$	$< 5{\cdot}10^{-7}$	$< 3.8{\cdot}10^{5}$
QCD $\hat{P}_T(80-120)$	0.0036 mb	$1{\cdot}10^{-5}$	$7{\cdot}10^{-6}$	$7.5{\cdot}10^{5}$
QCD $\hat{P}_T(120-170)$	0.0006 mb	$1{\cdot}10^{-4}$	$6.6{\cdot}10^{-5}$	$1.1{\cdot}10^{6}$
$t\bar{t}$	614 pb	0.015	0.010	$1.84{\cdot}10^{5}$
$Zb\bar{b} \to 4b$	52 pb	0.0022	$8{\cdot}10^{-4}$	$1.2{\cdot}10^{3}$

Table 5.12: Trigger selection efficiency, trigger+offline selection efficiency and expected number of events in 30 fb^{-1} for signal and considered background sources

step: invariant mass reconstruction:

- i,j,k and l are indeces over all jets
- 2 identical objects are searched for, minimizing $(\mathrm{m_{i,j}} - \mathrm{m_{k,l}})$, where $\mathrm{m_{i,j}}$ is the i-th and j-th jet invariant mass. The Higgs mass is taken as the mean value of the two selected invariant mass (m_h)
- once the two combinations are found, the four selected jets are used to reconstruct the 4 jets mass (m_ϕ)

The mean values (and σ_{fit}) of di-jet and four jet effective masses reconstructed in this way are: 120 (39) GeV/c^2 and 313 (76) GeV/c^2. A 1.5 σ windows in mass around m_h and m_ϕ were used to select signal and background events. Efficiency for the signal, background and the expected number of events with 30 fb^{-1} are summarized in Tab. 5.12. The number of signal events was evaluated for $\Lambda_\phi = 1$ TeV and $\xi = -0.35$. Plots in Fig. 5.23 shows the 2 jets (Higgs) and 4 jets (radion) invariant mass distribution for signal and background events after 30 fb^{-1}: the light distribution is for all background sources and the dark distribution is for the signal. The maximal number of expected signal events is about 10^4, while the total number of expected background events is about $2{\times}10^6$. Condidering systematical uncertainties on the estimated background, to have a significance equal to 5 the background should be known with a precision better than 10^{-3}. This means that this channel cannot increase the overall radion significance.

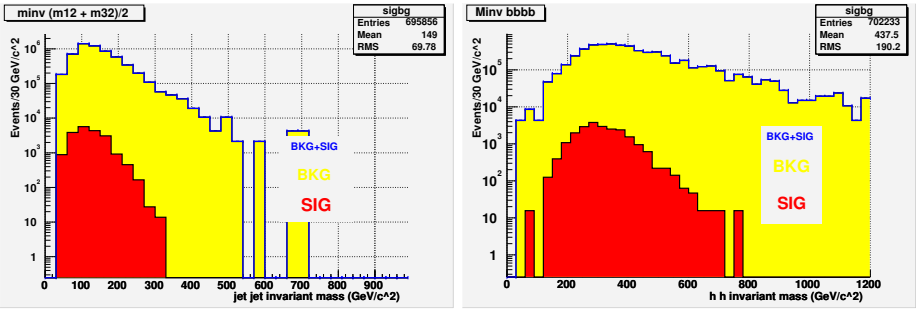

Figure 5.23: Signal and Background distribution for Higgs invariant mass reconstruction (left plot) and Radion mass (right plot) based on expected events in 30fb^{-1} in the (ξ, Λ_ϕ) phase space.

5.5 Results

The $\tau\tau$ bb and $\gamma\gamma$ bb final states have been investigated and studied in detail. They are to some extent complementary and offer clear possibilities to discover a radion if it exists with the assumed properties and to measure the signal significance. The bbbb final state has also been considered but, due to the huge QCD background, cannot be used to increase the significance of the previous two channels.

Conclusions

In this thesis the candidate has studied the observability of a scalar particle (the radion) forseen in theoretical models with extra dimensions. The presence of this particle would be a definitive proof of the existence of extra spatial dimensions. The Randall-Sundrum model with one extra dimension has been taken as an example; it allows to evaluate the rate of events in which the scalar particle called "radion" (ϕ) decays into two Higgs bosons. The main parameters of the model (besides the Higgs mass) are the radion mass, a mixing parameter (ξ) and the energy scale of the new physics (Λ).
The production and decay process $gg \rightarrow \phi \rightarrow hh$, which would allow the study of the two scalars at the same time, has been considered with three different final states:

- gg $\rightarrow \phi \rightarrow$ hh $\rightarrow \tau\tau$ bb
- gg $\rightarrow \phi \rightarrow$ hh $\rightarrow \gamma\gamma$ bb
- gg $\rightarrow \phi \rightarrow$ hh $\rightarrow$ bb bb

The candidate has analysed the $\tau\tau$ bb final state, Nikitenko and Dewhirst have analised the final state with two photons and Livio Fanò the one with four b-jets in the final state. The $\tau\tau$ and $\gamma\gamma$ final states are to some extent complementary and offer clear possibilities to extract the signal significance while no signal information can be extracted for the four b-jets final state, due to the huge QCD background.
In the $\tau\tau$ bb analysis it has been shown that the High Level τ trigger selection must be used in order to suppress bacground with fake τ-jets. This algorithm can reduce the background rate, providing good efficiency on the signal events by means of a tracker isolation criterium. The candidate has contributed to the development of this algorithm which is used in almost all the other CMS

studies with τ-jets in the final state.
The τ Trigger relies on the optimal performance of the CMS tracker, which permits a fast and regional track reconstruction. The candidate has also partecipated to the measurement of the dead time of the chip, used in the tracker modules, caused by a large release of energy in the silicon bulk. To measure this dead time a dedicated test beam, and several laboratory studies have been done. The candidate has simulated the dead time induced by a high energy deposit injected by means of laser pulses. The effect of this dead time on the track reconstruction and b-tagging efficiency has been studied during the past year. A modification of the track reconstruction software and of the front-end electronics software will ensure full efficiency recovery of the b-tagging performance even in the worst case of a dead time of 750 ns.

Acknowledgements

I would like to thank all the people who made this study possible.
Special thanks are needed to Dr. Roberto Tenchini, Dr. Fabrizio Palla and Dr. Giuseppe Bagliesi who gave important ideas and comments on the work. I would also thank all the Pisa Collaboration for all the usefull adivices and Sasha, Guy and Livio with whom I made the analysis.

Bibliography

[1] J. L. Rosner, "Resource letter: The standard model and beyond," arXiv:hep-ph/0206176;
J. R. Ellis, "Beyond the standard model for hillwalkers," arXiv:hep-ph/9812235;
C. Quigg, "The state of the standard model", arXiv:hep-ph/0001145;
J. Womersley, "Physics beyond the standard model," J. Phys. G **26** (2000) 505 arXiv:hep-ex/0001039.

[2] The Lep ElectroWeak Working Group, results presented at 2002 summer conferences, http://www.cern.ch/LEPEWWG/

[3] G. Altarelli, R. Barbieri and F. Caravaglios, "Electroweak precision tests: A concise review," Int. J. Mod. Phys. A **13** (1998) 1031 arXiv:hep-ph/9712368.

[4] Y. Fukuda *et al.* Super-Kamiokande Collaboration, "Evidence for oscillation of atmospheric neutrinos," Phys. Rev. Lett. **81** (1998) 1562 arXiv:hep-ex/9807003.

[5] One can also see the following reviews:
N. Schmitz, "The discovery of neutrino masses," arXiv:hep-ex/0211041
H. Pas, "Neutrino masses and particle physics beyond the standard model," Annalen Phys. **11** (2002) 551 arXiv:hep-ph/0209018

[6] F. Wilczek, "Beyond the standard model: This time for real," Nucl. Phys. Proc. Suppl. **77** (1999) 511 arXiv:hep-ph/9809509

[7] T. Hambye and K. Riesselmann, "Matching conditions and Higgs mass upper bounds revisited," Phys. Rev. D **55** (1997) 7255 arXiv:hep-

ph/9610272;
Lep Higgs Working Group, http://lephiggs.web.cern.ch/LEPHIGGS/www/Welcome.html

[8] R. Barbieri and A. Strumia, "The LEP paradox" arXiv:hep-ph/0007265

[9] M. Schmaltz, "Physics beyond the standard model (Theory): Introducing the little Higgs," arXiv:hep-ph/0210415

[10] Lep SuSy Working Group, http://www.cern.ch/lepsusy/

[11] G. Nordstrom, Z. Phys. **15**, 504 (1914)

[12] T. Kaluza, Preuss.Akad.Wiss, Berlin, Math. Phys. **K 1**, 966 (1921);
O. Klein Z. Phys. bf 37 895;
Nature **118**, 516 (1926)

[13] V. A. Rubakov, "Large and infinite extra dimensions: An introduction," Phys. Usp. **44** (2001) 871 Usp. Fiz. Nauk **171** (2001) 913 arXiv:hep-ph/0104152;
M. Besancon, "Experimental introduction to extra dimensions," arXiv:hep-ph/0106165;
A. Perez-Lorenzana, "Theories in more than four dimensions," AIP Conf. Proc. **562** (2001) 53 arXiv:hep-ph/0008333;
R. Tabbash, "Physics of extra dimensions: Higher-dimensional virtual environments," arXiv:hep-ph/0111334

[14] K. R. Dienes, "Beautified with goodly shape: Rethinking the properties of large extra dimensions," arXiv:hep-ph/0211211

[15] N. Arkani-Hamed, S. Dimopoulos and G. R. Dvali, "The hierarchy problem and new dimensions at a millimeter," Phys. Lett. B **429** (1998) 263 arXiv:hep-ph/9803315
I. Antoniadis, "A Possible New Dimension At A Few Tev," Phys. Lett. B **246** (1990) 377;
J. D. Lykken, "Weak Scale Superstrings," Phys. Rev. D **54** (1996) 3693 arXiv:hep-th/9603133

[16] J. C. Long, H. W. Chan, A. B. Churnside, E. A. Gulbis, M. C. Varney and J. C. Price, "New experimental limits on macroscopic forces below 100-microns," arXiv:hep-ph/0210004

[17] N. Arkani-Hamed, S. Dimopoulos and G. R. Dvali, "Phenomenology, astrophysics and cosmology of theories with sub-millimeter dimensions and TeV scale quantum gravity," Phys. Rev. D **59** (1999) 086004 arXiv:hep-ph/9807344

[18] G. F. Giudice, R. Rattazzi and J. D. Wells, "Quantum gravity and extra dimensions at high-energy colliders," Nucl. Phys. B **544** (1999) 3 arXiv:hep-ph/9811291;
G. F. Giudice, R. Rattazzi and J. D. Wells, "Graviscalars from higher-dimensional metrics and curvature-Higgs mixing," Nucl. Phys. B **595** (2001) 250 arXiv:hep-ph/0002178

[19] G. F. Giudice, R. Rattazzi and J. D. Wells, "Transplanckian collisions at the LHC and beyond," Nucl. Phys. B **630** (2002) 293 arXiv:hep-ph/0112161

[20] T. Han, J. D. Lykken and R. J. Zhang, "On Kaluza-Klein states from large extra dimensions," Phys. Rev. D **59** (1999) 105006 arXiv:hep-ph/9811350;
S. Cullen and M. Perelstein, "SN1987A constraints on large compact dimensions," Phys. Rev. Lett. **83** (1999) 268 arXiv:hep-ph/9903422;
C. Hanhart, D. R. Phillips, S. Reddy and M. J. Savage, "Extra dimensions, SN1987a, and nucleon nucleon scattering data," Nucl. Phys. B **595** (2001) 335 arXiv:nucl-th/0007016

[21] L. J. Hall and D. R. Smith, "Cosmological constraints on theories with large extra dimensions," Phys. Rev. D **60** (1999) 085008 arXiv:hep-ph/9904267;
S. Hannestad, "Strong constraint on large extra dimensions from cosmology," Phys. Rev. D **64** (2001) 023515 arXiv:hep-ph/0102290

[22] L. Anchordoqui, T. Paul, S. Reucroft and J. Swain, "Ultrahigh energy cosmic rays: The state of the art before the Auger observatory," arXiv:hep-ph/0206072, sections VII and IX;
R. Emparan, M. Masip and R. Rattazzi, "Cosmic rays as probes of large extra dimensions and TeV gravity," Phys. Rev. D **65** (2002) 064023 arXiv:hep-ph/0109287

[23] S. Alexander, R. H. Brandenberger and D. Easson, "Brane gases in the early universe," Phys. Rev. D **62** (2000) 103509 arXiv:hep-th/0005212

[24] A. Pomarol and M. Quiros, "The standard model from extra dimensions," Phys. Lett. B **438** (1998) 255 arXiv:hep-ph/9806263;
A. Delgado, A. Pomarol and M. Quiros, "Supersymmetry and electroweak breaking from extra dimensions at the TeV-scale," Phys. Rev. D **60** (1999) 095008 arXiv:hep-ph/9812489;
A. Delgado, A. Pomarol and M. Quiros, "Electroweak and flavor physics in extensions of the standard model with large extra dimensions," JHEP **0001** (2000) 030 arXiv:hep-ph/9911252

[25] T. Appelquist, H. C. Cheng and B. A. Dobrescu, "Bounds on universal extra dimensions," Phys. Rev. D **64** (2001) 035002 arXiv:hep-ph/0012100

[26] Y. Kawamura, "Triplet-doublet splitting, proton stability and extra dimension," Prog. Theor. Phys. **105** (2001) 999 arXiv:hep-ph/0012125

[27] G. Altarelli and F. Feruglio, "SU(5) grand unification in extra dimensions and proton decay," Phys. Lett. B **511** (2001) 257 arXiv:hep-ph/0102301

[28] Lectures at Corfu Summer Institute, September 2001; based on A. Muck, A. Pilaftsis and R. Ruckl, "An introduction to 5-dimensional extensions of the standard model," arXiv:hep-ph/0209371

[29] J. Lykken and S. Nandi, "Asymmetrical large extra dimensions," Phys. Lett. B **485** (2000) 224 arXiv:hep-ph/9908505

[30] R. Barbieri, L.J. Hall, Y. Nomura, " A constrained Standard Model from a Compact Extra Dimension", hep-ph/0011311

[31] I. Antoniadis, N. Arkani-Hamed, S. Dimopoulos and G. R. Dvali, "New dimensions at a millimeter to a Fermi and superstrings at a TeV," Phys. Lett. B **436** (1998) 257 arXiv:hep-ph/9804398

[32] L. Randall and R. Sundrum, "A large mass hierarchy from a small extra dimension," Phys. Rev. Lett. **83** (1999) 3370 arXiv:hep-ph/9905221

[33] W. D. Goldberger and M. B. Wise, "Modulus stabilization with bulk fields," Phys. Rev. Lett. **83** (1999) 4922 arXiv:hep-ph/9907447

[34] W. D. Goldberger and M. B. Wise, Phys. Rev. Lett. **83**, 4922 (1999)

[35] L. Randall and R. Sundrum, "An alternative to compactification," Phys. Rev. Lett. **83** (1999) 4690 arXiv:hep-th/9906064.

[36] L. Randall, R. Sundrum, Phys. Rev. Lett. 83 (1999) 3370, arXiv:hep-ph/9905221

[37] R. Sundrum, Phys. Rev. D59, 085010 (1999) hep-ph/9807348;
N. Arkani-Hamed, S. Dimopoulos and J. March-Russell, hep-th/9809124;
W. D. Goldberger and M. B. Wise, Phys. Rev. Lett. 83, 4922 (1999) hep-ph/9907447

[38] J.J. van der Bij, Acta Physica Polonica, B 25 (1994) 827
R. Raczka, M. Pawlowski, Found. Phys. 24 (1994) 1305, arXiv:hep-th/9407137

[39] D. Dominici, B. Grzadkowski, J. F. Gunion and M. Toharia, arXiv:hep-ph/0206192

[40] H. Davoudiasl, J. L. Hewett and T. G. Rizzo, Phys. Rev. D 63 (2001) 075004 arXiv:hep- ph/0006041

[41] G. Abbiendi et al. OPAL Collaboration, Eur. Phys. J. C 7, 407 (1999), hep-ex/9811025

[42] OPAL Collaboration, preliminary physics note: OPAL Physics Note 495, Feb. 2002

[43] D. Buskulic et al. ALEPH Collaboration, Phys. Lett. B 313, 312 (1993)

[44] LEP seminar, July 10, 2001, P Teixeira-Dias, on behalf of the LEPHIGGS working group

[45] LEP Higgs Working Group for Higgs boson searches Collaboration, arXiv:hep-ex/0107029

[46] M. Spira, hep-ph/9704448.
D. Dominici, private communication.

[47] The LHC Study Group, CERN/AC/95-05

[48] the ATLAS Collaboration, ATLAS Technical Proposal, CERN/LHCC 94-43

[49] CMS Technical Proposal CERN/LHCC 94-038

[50] the ALICE Collaboration, ALICE Technical Proposal, CERN/LHCC 95-71

[51] the LHCb Collaboration, LHCb Technical Proposal, CERN/LHCC 98-4

[52] the CMS Collaboration, CMS TDR - Technical Design Report: CMS - MAGNET

[53] the CMS Collaboration, CMS TDR - Technical Design Report: CMS - TRACKER, CERN/LHCC 98-6

[54] the CMS Collaboration, Addendum to the CMS Tracker TDR, CERN/LHCC 2000-016

[55] the CMS Collaboration, CMS TDR - Technical Design Report: CMS - ECAL, CERN/LHCC 97-33

[56] D.Green, K.Maeshima, R.Vidal, W.Wu and S.Kunori, CMS NOTE 2002/004

[57] the CMS Collaboration, CMS TDR - Technical Design Report: CMS - HCAL, CERN/LHCC 97-31

[58] Alexandre Nikitenko private communication.

[59] CMS Technical note 1998, $http://uscms.fnal.gov/uscms/Subsystems/HCAL/hcal_docs/hcal_d$

[60] the CMS Collaboration, CMS TDR - Technical Design Report: CMS - MUON, CERN/LHCC 97-32

[61] the CMS Collaboration, CMS TDR - Technical Design Report: CMS - TRIGGER, Vol.1 CERN/LHCC

[62] the CMS Collaboration, CMS TDR - Technical Design Report: CMS - TRIGGER, Vol.2 in preparation

[63] D. Kotlinski, CMS IN 2000/022

[64] D. Lucchetti *et al.*, in '*Proceeding of the Fifth International Symposium on High Purity Silicon*', Electrotechnical Society Proceedings, Vol.98-13

[65] G. Segneri *et al.*, Nucl. Instr. Meth. **A476** (2002), 729

[66] L. Borrello *et al.*, to appear on IEEE Trans. Nucl. Sci.

[67] S. Braibant *et al.*, CMS NOTE 2000/011

[68] N. Demaria *et al.*, Nucl. Instr. Meth. **A447** (2000), 142
N. Albergo *et al.*, Nucl. Instr. Meth. **A466** (2001), 300

[69] G. Lutz, '*Semiconductor Radiation Detector*', Springer Verlag

[70] GEANT-3, '*Detector Description and Simulation Tool*', CERN Program Library entry W5013, CERN, Geneva, Ed. March 1995

[71] M.Moll, Ph.D Thesis (Hamburg University), DESY-THESIS-1999-040

[72] A. Chilingarov *et al.*, Nucl. Instr. Meth. **A360** (1995), 432

[73] Bates *at al.*, IEEE Trans. Nucl. Sci. **43** (1996), 199
Bates *at al.*, CERN/ECP 95-19

[74] E. Fretwurst *at al.*, Nucl. Instr. Meth. **A342** (1994), 19

[75] F. Lemeilleur *et al.*, Nucl. Instr. Meth. **A360** (1995), 438

[76] http://cms.web.psi.ch/cms.html

[77] R. Baur, Nucl. Instr. Meth. **A465** (2000), 159
D. Kotlinski, R. Baur, K. Gabathuler, R. Schnyder and W. Erdmann, in *Proceedings of the 6th Workshop on Electronic for LHC Experiments* (Cracow, Poland, Sept. 11-15 2000)

[78] M. French, '*APV User Manual*', available at:
http://te.rl.ac.uk/med

[79] A. MArchioro, '*CMS Microstrip Tracker Electronics*', available at:
http://www.cmstrackercontrol.web.cern.ch/CMSTrackerControl/documents/GeneralDoc.htm

[80] S. Gadomski *et al.*, Nucl. Instr. Meth. **A320** (1992), 217

[81] V. Radeka and R.A. Boie, Nucl. Instr. Meth. **A178** (1980), 543

[82] L. Borrello *et al.*, Nucl. Instr. Meth. **A461** (2000), 178

[83] S. Dutta *et al.*, IEEE Trans. Nucl. Sci. **48** (2001), 2303

[84] O. Adriani *et al.*, Nucl. Instr. Meth. **A396** (1997), 76

[85] A. Heikkinen and V. Karimaki, CMS NOTE 1999/029

[86] S. Dutta *et al.*, Nucl. Instr. Meth. **A476** (2002), 739

[87] M. Lenzi *et al.*, IEEE Trans. Nucl. Sci. **48** (2001), 1016

[88] ORCA reference guide, available at:
http://www.cmsdoc.cern.ch/orca

[89] T. Todorov, in '*Proceeding of the International Conference on Computing in High Energy and Nuclear Physics*', (Padova, Italy, February 7-11 2000)

[90] R. Fruhwirth, M. Regler, R.K. Bock, H. Grote and D. Motz, '*Data Analysis Techniques for High Energy Physics*', Cambridge University Press, 2000

[91] R. Fruhwirth Nucl. Instr. Meth. **A262** (1997), 444

[92] T. Sjostrand *PYTHIA 6.2 Physics and Manual*, hep-ph/0108264.

[93] "Information on Oct. 2001 X5 Test-Beam",http://hepwww.rl.ac.uk/CMSTracker/b
tau/TestBeam/X5oct2001.html,

[94] L.Jones,"The APV25-S1 User manual",
http://www.te.rl.ac.uk/med/projects/High_Energy_Physics/CMS/APV25-S1/pdf/User_Guide_2.2.pdf

[95] M. Huhtinen, "Highly Ionising Events in Silicon Detectors", CMS-NOTE-2002/011.

[96] R. Bainbridge et al., "The Effect of Highly Ionising Events on the APV Readout Chip", CMS NOTE 2002/038

[97] I. Tomalin et al. "Test-Beam Analysis of the Effect of Highly Ionising Particles on the Silicon Strip Tracker", CMS-NOTE 2003/025

[98] "The Tracker project Technical Design Report", CERN/LHCC 98-6

[99] M.Ageron at al.,"The Trigger Sequencer Card user's manual",http://lyoinfo.in2p3.fr/cms/tsc/tsc03.pdf

[100] L.Mirabito, "The standalone Tracker data acquisition program", CMS internal note to be published.

[101] L.Mirabito et al., "Tracker Data Acquisition for Beamtest and Integration " , CMS IN-2003/021

[102] D. Bouvet et al., "Results on the radiation hardness of Small Gap Chambers", Nucl.Instrum.Meth.A454:359-363,2000.

[103] M. Raymond, "Laboratory studies of the HIP and pin-hole effects on the APV", http://cmsdoc.cern.ch/Tracker/managment/Agenda GTM/GM 01 12/Mark CMShipstalk.ppt (Dec. 2001), http://cmsdoc.cern.ch/ghall/TKEL 0102/Raymond 0102.pdf (Jan. 2002).

[104] Andrea Rizzi's Degree thesis.

[105] Tommaso Boccali's private communication.

[106] CMS Coll., "*The Trigger and Data Acquisition project, Volume I, The Level-1 Trigger, Technical Design Report*", CERN/LHCC 2000-038, CMS TDR 6.1, 15 December 2000.

[107] M. Aguilar-Benitez at al., "*Construction and Test of the final CMS Barrel Drift Tube Muon Chamber Prototype*", Nucl. Instr. and Meth. A480 (2002) 658

[108] S. Eno *et al.*, CMS Note 2000/055

[109] G. Bagliesi, S. Gennai, G. Sguazzoni: CMS Note 2002/018

[110] R. Kinnunen, A. Nikitenko, CMS Note 1997/106
R. Kinnunen, D. Denegri, CMS Note 1999/037

[111] P. Chumney, S. Dasu, W.H. Smith, CMS Note 2000/074

[112] http://home.fnal.gov/sceno/jpg/Default.html; Description of the HCAL calibration scheme

[113] J. E. Huth et al., Proceeding of Research Directions for the decade, Snowmass 1990

[114] G. Bagliesi, S. Dutta, S. Gennai, G. Sguazzoni, CMS IN2001/045

[115] R. Kinnunen talk at SUSY02, DESY Hamburg

[116] R. Kinnunen private communication

[117] D. Kotliński, A. Nikitenko and R. Kinnunen, CMS Note 2000/045

[118] R. Kinnunen et al.: CMS Note 2001/032

[119] D. Kotlinski, A. Nikitenko, R. Kinnunen: CMS Note 2001/017

[120] R. Kinnunen, CMS Note 2001/047

[121] E. Meschi *et al.*, CMS Note 2001/034.

[122] CMS Coll., The Electromagnetic Calorimeter Project, Technical Design Report, CERN/LHCC 97-33, CMS TDR 4, 15 December 1997.

[123] V. Innocente, M. Maire, E. Nagy, CERN program library long writeup W5013-E, GEANE.

[124] G. Bruno *et al.*, CMS Note 2002/043.

[125] . N. Amapane, M. Fierro, M. Konecki, CMS Note 2002/040.

[126] M. Battaglia *et al.*, hep-ph/0304245.

[127] ATLAS Collaboration, EPJ direct C, **4**, C16, 1-13 (2002), Study presented at the Les Houches workshop in 2001.

[128] G. Segneri, F. Palla, CMS Note 2002/046.

[129] A. Pukhov *et al.*, CompHEP manual, hep-ph/9908288.

[130] S. Abdullin *et al.*, CMS TN/94-180.

[131] J. Campbell, *at al.*, hep-ph/0308195, D. Chakraborty, *at al.*, hep-ph/0303092.

[132] S. Abdullin *et al.*, CMS IN 2001/001.

[133] G. Batignani, *et al.* ALEPH 93-95, PHYSIC 93-78.

[134] The Lep Collaboration, Ph. Lett. **B 565**, p. 71, 2003.

[135] John Conway, FERMILAB-Conf-00/048-E CDF May 2000.

[136] A. De Roeck, private communication.

[137] C. Seez, private communication

[138] F. Maltoni and T. Stelzer, JHEP 0302 (2003) hep-ph/0208156; T. Stelzer and W. F. Long, Comput. Phys. Commun., 81 (1994) p.357, hep-ph/9401258. CMS note in preparation.

[139] S. Shevchenko, private communication